GROWTH AND MORPHOLOGICAL CHARACTERIZATION OF INTRINSIC HYDROGENATED
AMORPHOUS SILICON THIN FILM FOR a-Si:H/c-Si HETEROJUNCTION SOLAR CELLS

A THESIS SUBMITTED TO
THE GRADUATE SCHOOL OF NATURAL AND APPLIED SCIENCES
OF
MIDDLE EAST TECHNICAL UNIVERSITY

BY

ÖZLEM PEHLİVAN

IN PRACTICAL FULFILLMENT OF THE REQUIREMENTS
FOR
THE DEGREE OF DOCTOR OF PHILOSOPHY
IN
PHYSICS

JANUARY 2013

Approval of the thesis:

GROWTH AND MORPHOLOGICAL CHARACTERIZATION OF INTRINSIC HYDROGENATED AMORPHOUS SILICON THIN FILM FOR a-Si:H/c-Si HETEROJUNCTION SOLAR CELLS

submitted by **ÖZLEM PEHLİVAN** in partial fulfillment of the requirements for the degree of **Doctor of Philosophy in Physics Department, Middle East Technical University** by,

Prof. Dr. Canan Özgen   _____
Dean, Graduate School of **Natural and Applied Sciences**

Prof. Dr. Mehmet Zeyrek   _____
Head of Department, **Physics**

Prof. Dr. Mehmet Tomak   _____
Supervisor, **Physics Dept., METU**

Assoc. Prof. Dr. Alp Osman Kodolbaş   _____
Co-Supervisor, **UME, TUBITAK**

Examining Committee Members:

Assoc. Prof. Dr. Orhan Özdemir   _____
Physics Dept., Yıldız Technical University

Prof. Dr. Mehmet Tomak   _____
Physics Dept., METU

Assist. Prof. Dr. Akın Bacıoğlu   _____
Physics Engineering Dept., Hacettepe University

Prof. Dr. Çiğdem Erçelebi   _____
Physics Dept., METU

Assoc. Prof. Dr. Akif Esendemir   _____
Physics Dept., METU

                                                      Date: 25.01.2013

I hereby declare that all information in this document has been obtained and presented in accordance with academic rules and ethical conduct. I also declare that, as required by these rules and conduct, I have fully cited and referenced all material and results that are not original to this work.

Name, Last name: ÖZLEM PEHLİVAN

Signature :

ABSTRACT

GROWTH AND MORPHOLOGICAL CHARACTERIZATION OF INTRINSIC HYDROGENATED AMORPHOUS SILICON THIN FILM FOR a-Si:H/c-Si HETEROJUNCTION SOLAR CELLS

Pehlivan, Özlem
Ph.D., Department of Physics
Supervisor: Prof. Dr. Mehmet Tomak
Co-Supervisor: Assoc. Prof. Dr. Alp Osman Kodolbaş

January 2013, 102 pages

Passivation of the crystalline silicon (c-Si) wafer surface and decreasing the number of interface defects are basic requirements for development of high efficiency a-Si:H/c-Si heterojunction solar cells. Surface passivation is generally achieved by development of detailed silicon wafer cleaning processes and the optimization of PECVD parameters for the deposition of intrinsic hydrogenated amorphous silicon layer.

a-Si:H layers are grown in UHV-PECVD system. Solar cells were deposited on the p type Cz-silicon substrates in the structure of Al front contact/a-Si:H(n)/a-Si:H(i)/c-Si(p)/Al back contact. Solar cell parameters were determined under standard test conditions namely, using 1000 W/m^2, AM 1.5G illumination at 25 $^{\circ}$C.

Growth of (i) a-Si:H, films on the clean wafer surface was investigated as a function of substrate temperature, RF power density, gas flow rate, hydrogen dilution ratio and deposition time and was characterized using SEM, HRTEM, AFM, SE, ATR-FTIR and I/V measurements.

Structural properties of the films deposited on silicon wafer surface are directly effective on the solar cell efficiency. Morphological characterization of the grown films on the crystalline surface was found to be very complex depending on the deposition parameters and may even change during the deposition time.

At 225 $^{\circ}$C substrate temperature, at the beginning of the deposition, (i) a-Si:H films was found grown in epitaxial structure, followed by a simultaneous growth of crystalline and amorphous structure, and finally transforming to complete amorphous structure. Despite this complex structure, an efficiency of 9.2% for solar cells with total area of 72 cm^2 was achieved. In this cell structure, TCO and back surface passivation do not exist.

In the ≤200 $^{\circ}$C temperature region, we realized an existence of process window for the deposition temperature of intrinsic and n-doped layers in our PECVD system.

From the post annealing studies, we have observed that solar cell parameters improve when the barrier energy reaches 1.2eV, which is in close agreement with the minimum photon energy for the observation of light induced defects (SWE) in a-Si:H. A model based on breaking of weak Si-Si bonds, bond switching and hydrogen passivation from interface is suggested to explain our results.

Keywords: a-Si:H, solar cell, PECVD, heterojunction, spectroscopic ellipsometer, annealing, epitaxial, FTIR.

ÖZ

a-Si:H/c-Si HETEROEKLEM GÜNEŞ PİLLERİ İÇİN KATKISIZ HİDROJENLENDİRİLMİŞ AMORF SİLİSYUM İNCE FİLMLERİN BÜYÜTÜLMESİ VE MORFOLOJİK KARAKTERİZASYONU

Pehlivan, Özlem
Doktora, Fizik Bölümü
Tez Yöneticisi: Prof. Dr. Mehmet Tomak
Ortak Tez Yöneticisi: Doç. Dr. Alp Osman Kodolbaş

Ocak 2013, 102 sayfa

Kristal silisyum (c-Si) alttaban yüzeyinin pasivasyonu ve ara yüzey kusurlarının azaltılması, yüksek verimli a-Si:H/c-Si heteroeklem güneş pillerinin gelişiminde temel gereksinimlerdir. Yüzey pasivasyonu, genel olarak silisyum alttaban temizlik süreçlerinin detaylı bir şekilde geliştirilmesi ve katkısız hidrojenlendirilmiş amorf silisyum tabakanın büyütülmesi için gerekli olan PECVD parametrelerinin belirlenmesi ile sağlanır.

a-Si:H filmler yüksek vakumlu plazma destekli kimyasal buhar kaplama (UHV-PECVD) sistemi ile kaplanmıştır. Güneş pilleri, p tipi Cz-silisyum alttabanlar üzerine Al ön kontak/a-Si:H(n)/a-Si:H(i)/c-Si(p)/Al arka kontak yapısında oluşturulmuştur. Güneş pili parametreleri 1000 W/m^2 AM 1.5G güneş simülatörü altında standart test şartlarında, 25 ^{o}C sıcaklık değerinde belirlenmiştir.

Katkısız, hidrojenlendirilmiş amorf silisyum filmlerin temizlenmiş wafer yüzeyine büyümesinin alt taban sıcaklığı, RF güç değeri, gaz akış hızı, hidrojen seyreltme oranı ve film büyütme süresine bağımlılığı SEM, HRTEM, AFM, SE, ATR-FTIR ve I/V ölçümleri ile incelenmiştir.

Silisyum wafer üzerinde büyüyen filmin morfolojisi güneş pili verimliliğini doğrudan etkilemektedir. c-Si üzerinde büyüyen filmin morfolojisinin film büyütme parametrelerine bağlı olarak komplex olabileceği ve film büyütme sürecinde değişebileceği gözlenmiş ve incelenmiştir.

225 ^{o}C alt taban sıcaklığında kaplanan katkısız hidrojenlendirilmiş filmlerin ilk etapta kristal yapıda büyüdüğü, daha sonra kristal ve amorf yapının bir arada büyüdüğü ve son olarak amorf yapıya dönüştüğü gözlenmiştir. Bu özelliklere sahip katkısız tabakaya karşın, tam alanı 72 cm^2 olan güneş pillerinde 9.2% verim elde edilmiştir. Bu pil yapısında TCO ve arka yüzey pasivasyonu bulunmamaktadır.

200°C ve daha düşük taban sıcaklıklarında, mevcut PECVD sistemi için belirtilen tabakaların her sıcaklık değerinde büyütülemeyeceği, yüksek verimli piller için bir sıcaklık penceresinin varlığı tespit edilmiştir.

Büyütme sonrası tavlama çalışmaları ile pil parametrelerinde 1.2 eV bariyer enerji seviyelerinde iyileşme gözlenmiştir. Bu değer, güneş pilinin aydınlatılması sonucunda oluşan ışıl kusurların oluşması için gerekli olan en düşük foton enerji değeri ile uyum göstermektedir (SWE). Yapıdaki iyileşmenin zayıf Si-Si bağlarının kırılarak ara yüzeyde bulunan hidrojene bağlanmasından kaynaklandığı önerilmiştir.

Anahtar kelimeler: a-Si:H, güneş pili, PECVD, heteroeklem, spektroskopik elipsometre, tavlama, epitaksiyel, FTIR.

In the memory of Oben Sezer.

ACKNOWLEDGMENTS

TABLE OF CONTENTS

LIST OF TABLES

TABLES

LIST OF FIGURES

FIGURES

CHAPTER 1

INTRODUCTION

In the modern world, finding new alternative energy sources is a vital issue for many reasons. One reason is that traditional energy sources like coal, gas, and oil are not renewable sources and they will eventually be depleted. Another important reason is that burning of fossil fuels cause air and water contamination. Additionally, one of the most important another reason is that the electricity generated from fossil fuels has led to high concentrations of harmful gases like carbon monoxide, carbon dioxide, etc. in the atmosphere, which increase the average temperature on the planet, which is known as the global warming.

Clean and renewable energy sources like solar energy, wind energy and hydrogen fuel energy can be considered as an alternative. This kind of energy resources cause fewer emissions, reduce pollution and stand out as a viable source of clean and limitless energy. In this study, we will focus on the solar energy as one of the most promising sources of alternative energy.

Photovoltaic is the converting solar radiation into electricical energy. It was first discovered by Henri Becquerel in 1839 [1]. Definition of the photovoltaic can be given as the occurrence of an electric voltage between two electrodes attached to a system when light is applied onto the system. These devices are known as solar cells. Photovoltaics are a semiconductor technology that converts solar radiation into direct-current electricity, without moving parts, burning fuel, and pollution. This can be used directly or converted into AC, and it can be stored for later use.
Some of the advantages of PV can be outlined as:

– They can directly convert solar radiation into electricity,
– They are mechanically stable,
– They can be produced at low deposition temperatures; so low production cost,
– They are not pollute the environment
– Lifetime of the modules are long,
– They use free and relatively perpetual energy source, the sun,
– With its power ranging from micro-watts to mega-watts; PV is a very large range energy source.

1.1 Motivation for a-Si:H/c-Si Heterojunction Solar Cells

Hydrogenated amorphous silicon (a-Si:H) solar cells belong to the "second generation" or thin film class of PV devices that have the potential for cost effective solar power. These Si:H PV devices have many advantages over "first generation" crystal silicon PV and other thin film PV devices that make them an attractive option for further research and development in increased efficiency and cost reduction. The materials used in the manufacture of these Si:H solar panels are not toxic and are readily available. For hydrogenated amorphous silicon (a-Si:H), a very high optical absorption coefficient ($>10^5$ cm^{-1}) allows the undoped absorber layers that compose the PV structure to be made thinner. Thus, less material is consumed during fabrication, and hence the production cost is lowered.

Additionally, other advantages can be highlighted as; applicability of low temperature during deposition. With a ~1.7eV it has a suitable bandgap energy value, at which high solar energy conversion efficiency values are optained. Its raw material is abundant and it can be easily doped both p-type and n-type using boron or phosphorous respectively.

Most of the layers in the a-Si:H solar cell are deposited using plasma enhanced chemical vapor deposition (PECVD) system. This method has been used as a method to deposit thin films in a controllable manner. In a typical enhanced CVD process, the precursor gas molecule from which the material is to be deposited is exposed to some form of energy rather than thermal. RF power breaks

precursor gases into smaller constituents, which can adsorb on the substrate. PECVD uses plasma as the energy source to convert precursors into radicals. Energetic ions from the plasma may also contribute to radical-substrate reactions. The focus of this thesis is on the deposition of thin films in solar cell structures of the p-i-n configuration. The primary gas used in the fabrication of these solar cells is silane (SiH_4). In oreder to deposition of n-type and p-type doped a-Si:H layers, additional gases like phosphene (PH_3) and diborane (B_2H_6) are introduced in the chamber respectively.

Amorphous silicon/crystalline silicon heterojunction (SHJ) solar cell is one structure that uses only low temperature processing. Instead of high temperature treatment in diffused junction, SHJ employs deposited a-Si:H to form hetero-junction with crystalline silicon wafer. In addition, with the inherent passivation of amorphous silicon layer, this structure can achieve high open circuit voltages (V_{oc}), resulting in high power conversion efficiency (η). SHJ has drawn great interests and has been studied extensively in recent years due to its advantages of low cost, low processing temperature and potential for thinner wafers, while still keeping high efficiency and high stability.

The Heterojunction solar cell with Intrinsic Thin layer (HIT), a promising new member of the PV device family is developed by the Sanyo company, in the 1990's [2]. The device bases on a phosphorous doped n-type mono-crystalline Si wafer equipped with sequentially doped and intrinsic a-Si:H together with front and back contacts. Presently, the conversion efficiency of the HIT solar cell has reached a level of 23.7% for a 100 cm^2 crystalline silicon substrate. The other solar cell parameters are V_{oc}: 745mV, short circuit current (J_{sc}): 39.4mA/cm^2, fill factor: 80.9%) [3]. Originally, the doped amorphous Si layers was deposited directly on the wafer. It is found that the doped layers cause a high defect density at the surface and a high surface recombination velocity too [2]. To reach very high efficiencies, Sanyo integrated a thin intrinsic interlayer to passivate the c-Si surface. Since 1997 Sanyo has been fabricating HIT solar cell modules in mass production with module efficiencies up to 18.6 % that range among the highest in the world. Several research groups have tried to adapt Sanyo's concept of a-Si:H/c-Si heterojunction from phosphorous to boron doped wafers.

Surface passivation is still a challenge for n-type a-Si/p-type c-Si heterojunctions. New investigations are still possible for the passivation of the c-Si wafers surface. Among them, the most efficient surface passivation is obtained by either wet [4] or dry cleaning by HF solutions dry [5-6] cleaning of the crstalline silicon wafer surface ,followed by placing an intrinsic buffer layer [7-9] in between the a-Si:H thin film layer and c-Si substrate surface to improve the interface between a-Si:H and c-Si substrate. Additionally, it is known that film growth conditions are also strongly effective on the properties of a-Si/c-Si heterojunctions solar cells. Efficiency and carrier transport properties of the solar cells can be improved significantly by the optimization of plasma deposition parameters [10].

1.2 Objectives

Intrinsic layer in a-Si:H/c-Si heterojunction solar cells serves the reduction of interface states in c-Si surface while the photogenerated carriers are strongly swept in the electric field due to doped layers with much less recombination.

For the reduction of a-Si:H/c-Si heterojunction solar cell manufacturing cost, deposition of intrinsic layer at low temperature is crucial step, typically below 250 °C. Therefore, the primary objective of the present thesis is to deposit (i) a-Si:H films with and without H_2 dilution below 250 °C and investigate the influence of structural variations of intrinsic layers on the solar cell parameters of a-Si:H/c-Si based heterojunction.

Both wet chemical and dry etching methods are used for cleaning to obtain high quality c-Si surface prior to the deposition of a-Si:H film. So that, secondary objective of the present thesis is to the examine of both chemical and dry etching methods prior to the deposition of intrinsic a-Si:H film and study the interface properties of a-Si:H/c-Si heterojunctions.

The efficiency of the solar cells were characterized by the current-voltage (I-V) measurements under solar simulator illumination. In order to work on the structural analysis of the deposited layers HRTEM, SE anf FTIR analysis measurements were performed.

1.3 Contents of the Thesis

Chapter 2 introduces the fundamental background of solar cells in terms of device physics, band diagram analysis and gives an overview of the present understanding of the structural, electronic, and optical properties of amorphous silicon (a-Si).

Chapter 3 explains the experimental techniques performed during this thesis studies. Additionally, some experimental details including sample preparation, experimental set up, and device analysis methods for solar cells are given.

Chapter 4 focuses on the experimental data analysis and argues the results in detail. The performance of c-Si/a-Si:H HJ solar cells, fabricated by the processes discussed in the Chapter 2 are analyzed in this chapter. The performance of these solar cells with regards to the parameters like efficiency, V_{oc}, J_{sc} and fill factor and the structural analysis of intrinsic layer are studied and discussed extensively.

CHAPTER 2

HYDROGENATED AMORPHOUS SILICON SOLAR CELLS

2.1 Hydrogenated Amorphous Silicon

In this part, the basic concepts and general aspects of structural and electronic properties of hydrogenated amorphous silicon are going to be described.

2.1.1 Atomic Structure

One of the main parameter distinguishing the amorphous materials from crystalline materials is the disorder in its atomic structure. In crystalline structure, each silicon atom is covalently bonded to four neighboring atoms with an equal bond lengths and equal bond angles. Periodicity of the atomic structure is central to the theory of crystalline semiconductors.

While there is preservation of short range order in the a-Si:H structure, there is a lack of long range order as illustrated in Figure 2.1. Because of the short range order the conduction and valence bands can still be used in a-Si:H. The broad variations in bonding angles and bonding lengths between the adjacent atoms in a-Si:H result in weak or strained bonds. These bonds lead to exponentially decaying band tails in the band gap. Additionally, these weak bonds can easily be broken when a small amount of energy is applied to the material and defects in the atomic network such as dangling bonds in the band gap are created within the structure.
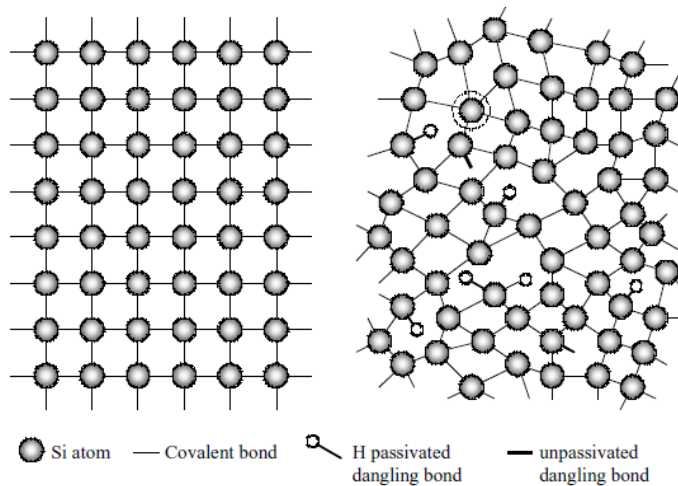
Figure 2.1 Schematic representation of the atomic structures for crystal silicon (a),and for hydrogenated amorphous silicon (b) [5].

In a crystal structure defects can be cathegorized as vacancies, interstitials and dislocations. Whereas, in the case of an amorphous semiconductor, basic defect is coordination defect, in which an atom has too many or too few bonds. The ability of the disordered network to adapt to any atomic coordination

5

allows an isolated coordination defect.This is not a possible case in a crystalline structure. The corresponding defects for the crystalline and amorphous structures are given in Figure 2.2.
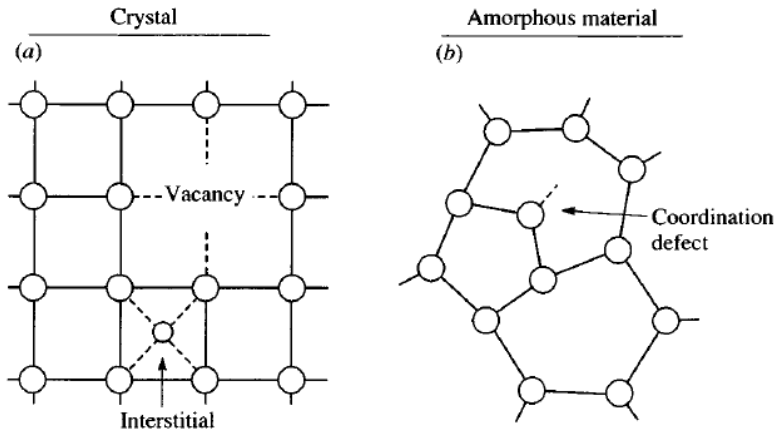
Figure 2.2 An illustration contrasting the different types of simple defects in (a) crystalline and (b) amorphous networks [6].

2.1.2 Electronic Structure

Because of the conservation of the short-range order, the amorphous material has a similar overall electronic structure with the crystal. The only deviation from the crystal is that the abrupt band edges of a crystalline material are replaced by a broadened tail of states extending into the forbidden gap in the case of the amorphous material. This deviation is caused by the variations of the bond lengths and bond angles arising from the long-range structural disorder. Additionally, there are allowed energy states located in between the valence band and conduction band states, originated from the coordination defects. These deviations create a continuous distribution of energy states in a-Si:H and that there is no well defined. Thus, the bandgap between the valence band and the conduction band is not well defined anymore. The electronic structure of an amorphous semiconductor is shown in the Figure 2.3.

Dangling bonds, present as positive (D^+), neutral (D^0) and negative (D^-) states, are considered as the dominant defect in a-Si:H structure. Two transition energy levels for dangling bonds $E^{+/0}$ (singly occupied dangling bond) and $E^{0/-}$ (doubly occupied dangling bond) characterize the charge occupation of the imperfection. The two Gaussian distributions, $D^{+/0}$ and $D^{0/-}$, represent the energy distributions of states corresponding to +/0 and 0/− charge transitions of dangling bonds, "transitions from neutral to positive charge states" and "transitions from neutral to negative charge states" respectively.

In the amorphous material, since due to the absence of long range order there is lack of periodicity of the atomic structure and the lattice symmetry. Thus, the Bloch's theorem and the theory of lattice vibrations are not feasible anymore [6-7]. Therefore, a new theoretical approach for this new configuration is applied to the system, which is called as Anderson Localization [11].
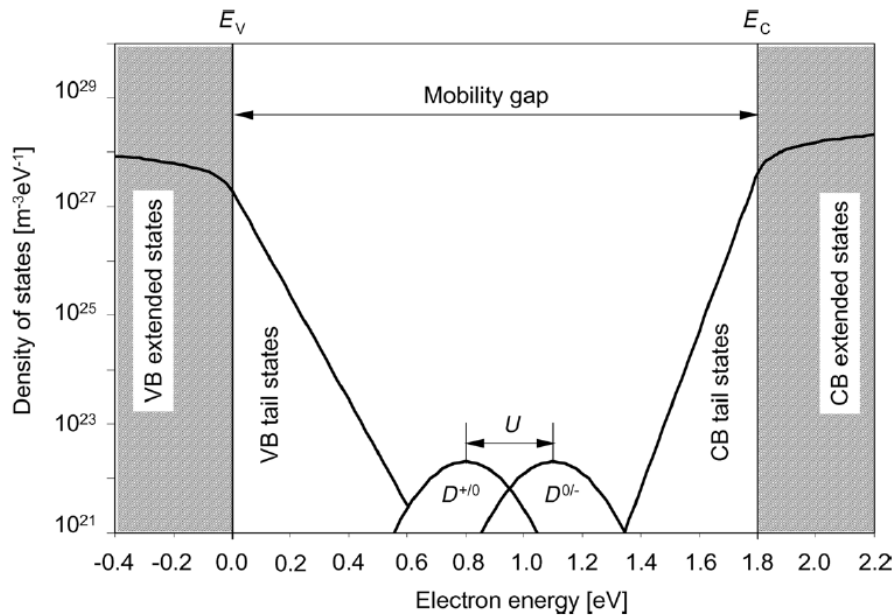
Figure 2.3 Density of states distribution for both c-Si and a-Si:H [5]

Anderson [12] has attempted to describe the disorder quantitatively by using a model of random varying local potentials. In his model, disorder creates a variable potential wells, leaving the spacing unchanged. Schematic of the meodel for both the crystalline and amorphous structures is given in Figure 2.4. In the model, Anderson defined a V_o potential as the additional random potential which has the same spatial periodicity as the original crystal potential. The corresponding band of electronic states are widened by a width B due to the interaction of the crystal atoms. According to Anderson, if the ratio of V_o and B is greater than three, there is no probability for an electron to diffuse any particular site. This is known as complete localization of the electron. When the disorder potential V_o is small, there is only a small perturbation from the original extended Bloch wavefunction and the the electron is scattered from one state to another within an extended band theory. On the other hand, if there is large disorder potential, frequent scattering results in the loss of the phase coherence in the electron wavefunction over two or three atomic spacings.

Schematic of the wavefunctions of extended and localized electron states both in crystalline and amorphous semiconductors are given in Figure 2.5 [8]. It can be easily seen that the phase coherence starts to deteriorate after a relatively short distance in the amorphous structure than the crystalline structure. When the disorder increases further more, the extended state in the amorphous structure transforms into a localized state and there is a rapid decay in the envelope.
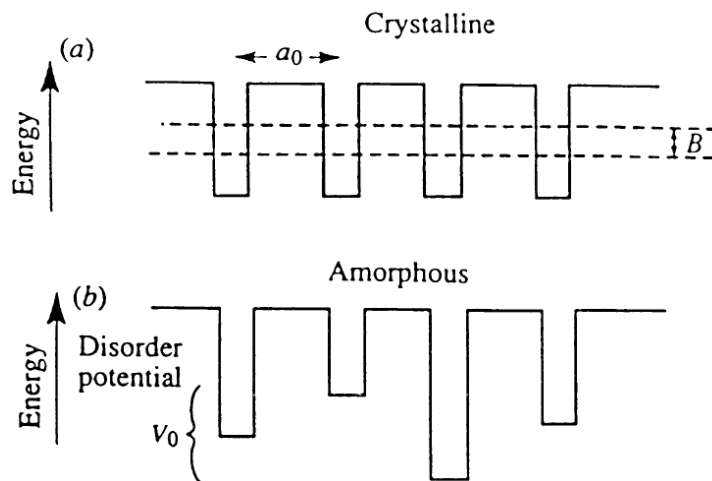
Figure 2.4 Anderson's model representations for both the crystalline and amorphous structures [6].
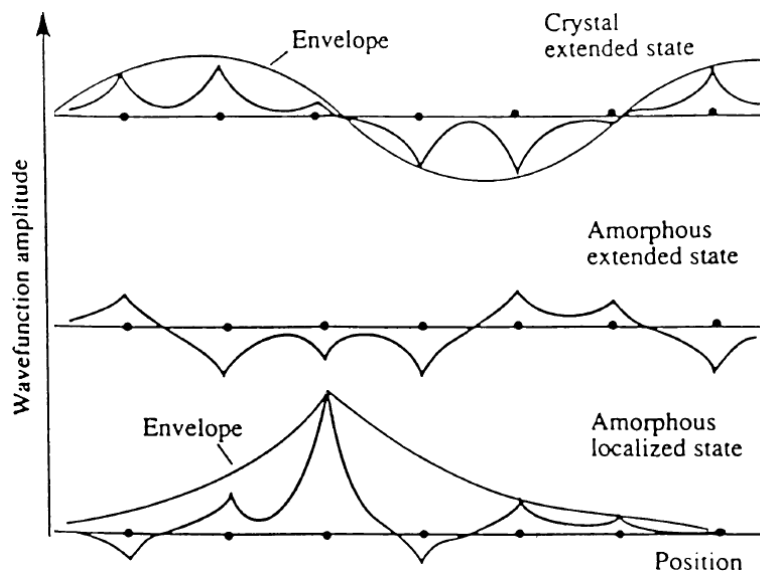
Figure 2.5 Extended and localized states representations for the crystalline and amorphous structures.

As a result, the strong scattering results in a large uncertainty in the value of electron momentum and momentum is not conserved in electronic transitions any more. As a result of lack of momentum conservation, the energy bands are described by an energy-dependent density of states distribution, instead of the energy-momentum dispersion relation. With this feature, a-Si:H has a direct band gap semiconductor and its absorption coefficient significantly higher than that of c-Si.

In this model, the density of states is determined by the bands, the band tails and the defect states deep in the band gap. Any disorder in the atomic lattice of a solid leads to an exponentially decaying density of localized states extending into the band gap, which is called as band tail [7].

8

The density of localized states and so the slope of the tail in the density of states are determined by the amount of disorder. The localized band tail states have a direct impact on both the electronic transport and optical behavior of a-Si:H in that due to trapping of charge carriers in the tail states, the effective mobility is reduced and becomes temperature-activated, so the thermal energy is needed to re-excite the trapped carriers.

2.1.3 The Role of Hydrogen Atoms in a-Si:H

In pure a-Si, defect concentration is about 10^{21} cm^{-3} [13]. Material with such a high defect density cannot be used for device applications since the Fermi level is pinned. When amorphous silicon is deposited from decomposition of silane by glow discharge, hydrogen atoms make a bond with most of the silicon dangling bonds and strong silicon–hydrogen bonds are formed [14-16]. Being a small atom, hydrogen can easily attach to dangling bonds and form an electron-pair bond, which results with the passivation of surfaces, grain boundaries, dislocations, shallow and deep impurity levels of the structure. Hydrogen passivation of dangling bond defects reduces the defect density from about 10^{21} cm^{-3} in pure a-Si to 10^{15}–10^{16} cm^{-3} in a-Si:H when the hydrogen concentration is about 9 % [13]. However, hydrogen also breaks and removes weak Si-Si bonds, causing reconstruction of the network. Therefore, optimization of hydrogen content and its bonding configurations are important parameters for the improvement of the performance and reliability of a-Si:H devices.

Figure 2.6 (b) shows a 3-d representation of amorphous silicon with dangling bonds passivated by hydrogen atoms. A crystalline structure is also shown for comparison in Figure 2.6(a) [15].
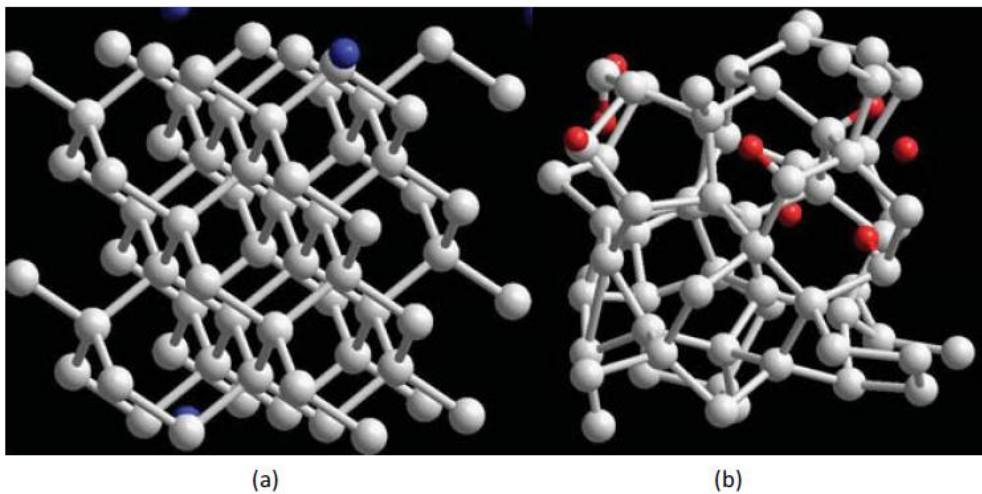
Figure 2.6 3-d computer model representation of c-Si (a), and a-Si (b) with dangling bonds passivated by hydrogen atoms [15].

Among all the gas radicals near the surface, atomic hydrogen can diffuse farthest into the material. The diffusion of hydrogen, its removal and adsorption at the surface, show that, at the deposition temperature, interstitial hydrogen can move quickly into the bulk where it attaches to silicon dangling bonds. Hydrogen therefore, is advantageous to be able to remove any subsurface defects within the structure. The diffusion of silicon in the bulk is much slower than that of hydrogen since the silicon has four covalent bonds but hydrogen only one.

2.2 Deposition of Hydrogenated Amorphous Silicon

During this thesis studies, the deposition of hydrogenated amorphous films is performed with plasma enhanced chemical vapour deposition (PECVD) system [6].

2.2.1 PECVD: An Introduction

Plasma is known as a fourth state of matter. When the temperature is increased and pressure is kept constant, in thermal equilibrium, a solid substance passes into a liquid state. As the temperature is further increased the liquid phases turn into a gas phases. When the temperature is high enough, the molecules in the gas decompose and form a gas of atoms. These atoms move freely in random directions and collide with each other. At even higher temperatures atoms become freely moving charged particles (electrons and positive ions), and the substance shifts into the plasma state. Plasma state of matter contains neutral radicals, ions and electrons.

There are two kinds of plasmas: If electrons, ions, and neutral species are in local thermodynamic equilibrium then it is called "thermal plasma". If the electrons and ions are more energetic than the neutral species, it is a nonequilibrium or "cold" plasma [17]. Nonequilibrium glow discharge plasmas are generally created by a radio-frequency (rf) electric field. At the beginning of the application of the electric field, since electrons are much lighter than ions, they are attracted faster by the negatively charged electrodes, while the heavier ions behave much slower. During the motion of electrons in the electric field, there will be inelastic collisions between high energy electrons and gas species, which generate new ions, electrons and highly reactive species, like excited neutrals or free radicals without increasing the gas temperature of the system. The central region of the plasma has slightly positive potential with respect to the electrodes because of the remaining positive ions. The maximum value with which ions can be accelerated from the edge of the sheath towards the substrate, located at the grounded electrode is the plasma potential. This potential causes ion bombardment that creates ion-surface interactions like: enhancement of adatom diffusion, displacement of surface atoms, trapping or sticking of incident ions, sputtering, and implantation.

Electrons are ejected from the sheaths; therefore, all ionization and dissociation processes occur in the plasma bulk. The positive ions and the neutral radicals reach the substrate by drift and diffusion respectively and go through surface and subsurface reactions during deposition. Film deposition is started by the diffusion of reactive neutral species. Positive ions are accelerated toward the substrate and they drift into the growing film. Movement of negative ions is restricted in the bulk of the plasma and they are transformed to particules.

2.2.2 Deposition Chamber Cleaning

During PECVD processes film deposition occurs on the chamber walls as well as on the substrate. This means that, the next deposition will start in a different reactor conditions and will have different properties. Therefore, it is necessary to clean the interior walls of the PECVD chamber periodically. This step is accomplished either manually (ex situ) or by dry cleaning (in situ).

Fluorine containing plasmas are commonly used for cleaning accumulated silicon dioxide (SiO_2) and silicon nitride (Si_3N_4) films from chamber walls after silicon based depositions [18,19]. Atomic or molecular fluorine reacts at the reactor walls with the deposited silicon, forms silicon tetrafluoride by converting solid silicon into volatile products which are to be extracted by using vacuum pumps [20].

Hrunski et al.[20] has suggest that the etching reaction products generally remain within the reactor and gas out continuously. This results in to their incorporation into the silicon films deposited in the system subsequently. This is proved by the fact that higher base pressure was observed in the deposition chamber after in situ cleaning (about 4×10^{-5} mbar) than before (about 10^{-7} mbar).

They have studied the influence of SF_6+O_2 and NF_3 gasses on the thin film solar cell performeance by chemical memory effect (CME) measurements. In order to measure the quality of i layer in the cell structure they have measure the fill factor that is very sensitive to the contaminations (Figure 2.7) [20]. According to the Figure 2.7, they have concluded that the replacement of the SF_6+O_2 gas mixture with NF_3 gas seriously reduced the CME. When they check the results of CME measurements, they get the following results: The "first" amorphous solar cells deposited after NF_3 cleaning had only a 5% lower FF unlike the SF_6+O_2, which had 18%. They have also point out the fact that NF_3 plasmas significantly decrease global warming emissions compared with SF_6.
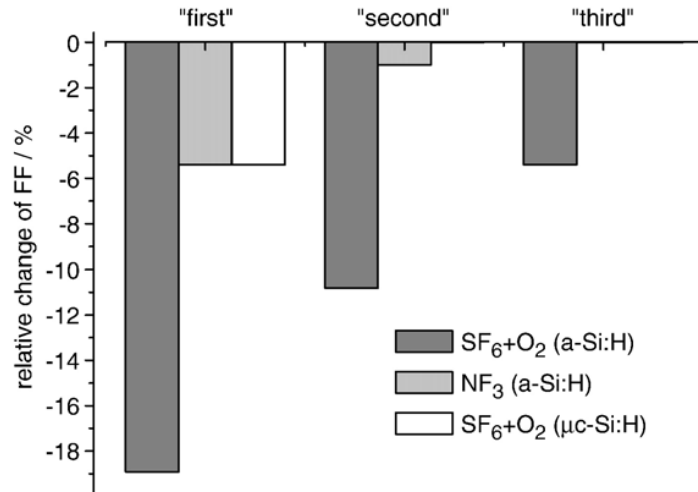
Figure 2.7 Change in the fill factor for a-Si:H and μc-Si:H solar cells relatevly, prepared after in situ cleaning procedure. "First", "second", and "third" cell denote the deposition sequence after in situ dry chamber cleaning [20].

2.3 a-Si:H Deposition Processes in PECVD System

During the deposition of the a-Si:H films by plasma techniques there are mainly three processes occur [21-25] :

- Gas phase/plasma processes,
- Surface processes and
- Subsurface processes.

Schematic representation of these processes is given in Figure 2.8. In the case of the gas phase–plasma reaction, the process starts with the dissociation of SiH_4 into both neutral radicals and ionic species as a result of collision with electrons. This is the primary reaction and controlled by the deposition parameters such as the gas flow rate, plasma power and gas pressure. There are sometimes following reactions in the gas phase. These reactions occur in between the reactive molecules and radicals generated in the plasma [14]. The importance of these secondary reactions are that by reacting the H atoms to the silane, they produce SiH_3 radical which is the most important radical and has the dominant effect for the a-Si:H deposition, since it is uncharged upon gas phase colllisions and reach the film surface. On the other hand, under high plasma power and/or pressure conditions, secondary processes lead to detrimental successive insertion reactions of reactive SiH_2 with SiH_4. As a result, higher silanes build up in the plasma and lead to the formation of polymeric particles [26].

11

In the surface reactions, there is an high interaction between the radicals and the surface of the growing film. Radicals diffuse the growth sites and they provide the contribution of the deposition by sticking the substrate [25]. Either sticking to or abstraction from the surface occurs on the surface, related with the substrate temperature.

In the subsurface reactions, hydrogen is released from this hydrogen rich layer which results in the improvement of the silicon network.
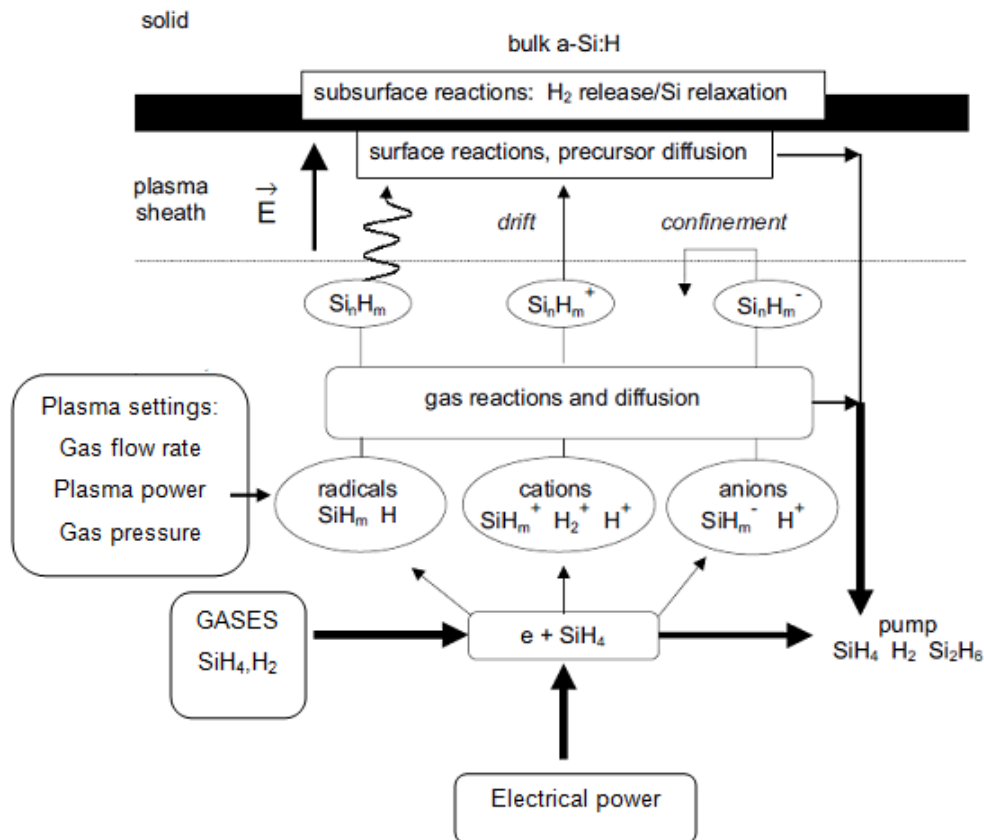
Figure 2.8 Schematic representation of the a-Si:H deposition from SiH_4/H_2 plasma [27].

2.3.1 Relation between Plasma Parameters and Material Properties

Generally, it is difficult to get the uniform homogeneous layers in thin film deposition. Some macroscopic inhomogeneities, such as voids, columnar growth structures and surface roughness can be created during the initial nucleation of the film on the substrate. Structure of the deposited films strongly depends on and sensitive the deposition conditions and operation parameters of the PECVD reactor [27].

1- Plasma power: The deposition rate is increased linearly with the plasma power density up to the point where the gas flow rate becomes the limiting factor. Increase in the deposition rate has a number of disadvantages like poor film quality and powder formation. At low power values, dissociation of

SiH$_4$ is low. Consequently, the films contain only silicon monohydrides. At high power levels on the other side, the SiH$_4$ is strongly dissociated and the films contain a large amount of SiH$_2$. Because of the increase of the hydrogen content in the deposited films, the optical band gap increases with increasing power. On the contrary, upon apptication of large power, microcrystalline silicon is formed in the film structure, leading to decrease in hydrogen content and band gap. Obviously, high quality films require optimum power levels.
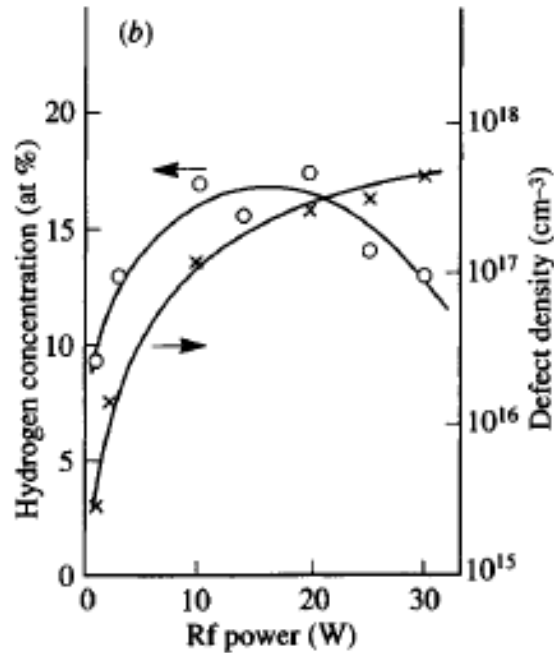
Figure 2.9 Dependence of material properties on RF power [6].

2- Gas flow rate: Residence time of heavy and short lifetime radicals in the plasma, which is a measure of the probability of a molecule to be incorporated into the film, increases when a gas flow rate is decreased [28]. With the increase in the residence time the contribution of molecules to the thin film growth increases, leading to a poor structural and electronic quality of film [29]. On the other hand, the gas utilization rate is low at higher flow rates [29], which means that the flow rate should also be optimized to obtain good quality films.

3- Substrate temperature: Since the substrate temperature is directly affects the kinetics of adsorption and desorption, surface diffusion and incorporation of growth precursors, it has a great effect on the structure of the deposited film. High substrate temperature gives high energy to SiH$_x$ adatoms and increases their mobility. By this way, adatoms can easily diffuse across the substrate surface and find an energetically favorable position [29]. On the other hand, further increase in substrate temperature results loss of hydrogen from the surface, creating large numbers of dangling bonds [29]. Thus, there is an optimum substrate temperature for thin film growth, which is in the range of 200°C to 300°C [9, 29-30].
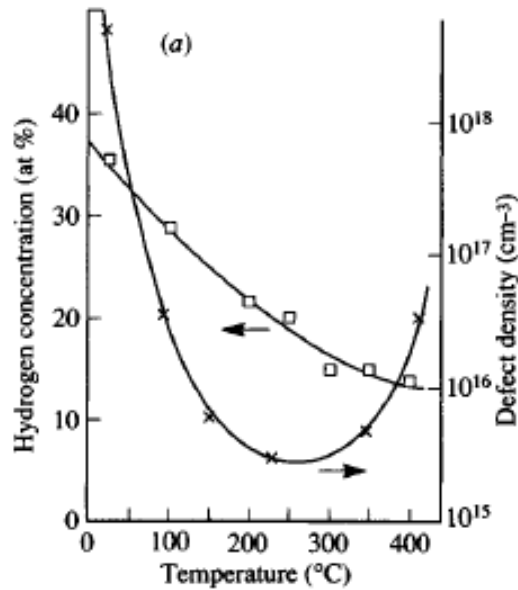
Figure 2.10 Dependence of material properties on substrate temperature [6].

4- Total pressure: During the deposition, there are two pressure regions as the Paschen's Law. At low-pressure region, the deposition is restricted by surface reaction, whereas at the high-pressure region the deposition is restricted by chemical processes in the gaseous phase [31].

In the high pressure regime (> 1 Torr), because of the secondary reactions, formation of higher levels of Si-H bonding like (Si_mH_x), SiH_3, etc. are more expected within the plasma bulk than in the low pressure regime [29]. Moreover, deposition rate of the thin films significantly increases and the powder formation within the plasma begins in the high-pressure regime [29].

5- Hydrogen dilution ratio: Hydrogen dilution is one of the main parameter that we have used to induce crystallinity in the films. The advantages of hydrogen dilution is ascribed to 3 mechanisms as [32]:

- In the presence of H_2 atoms, there is better surface passivation and more homogeneous film growth.
- Since the hydrogen species react with SiH_4 to form SiH_3, increase in H_2 dilution results the increase in [SiH_3].
- The hydrogen radicals break weak Si-Si bonds in the subsurface region and create dense, high-quality material.

Further increase in hydrogen dilution, on the other hand, reduces the deposition rate. This is because the depletion of SiH_4 in the chamber results in less species decomposed for film growth. Additionally, more H_2 in the chamber will increase the etching rate on the growing surface.

14

2.4 a-Si:H Growth Mechanism

Structure of the deposited a-Si:H network is defined by the growth parameters and therefore depends on the details of the deposition process. Thus, it is anticipated that the electronic properties vary with the growth conditions and hence a detailed understanding of the growth mechanisms is essential for the optimization of the electronic properties.

There are numbers of growth models for the a-Si:H deposition sequence [33]. One of the most populer model among them states that when SiH_3 radicals reach a film-growing surface, they start to diffuse across it. Various surface reactions occur during this diffusion process such that: some of the incoming SiH_3 is reflected back to the plasma and/or some of them are adsorbed onto the surface. After the adsorption of SiH_3, three different mechanisms on the surface are take place as in Figure 2.11, Figure 2.12 and Figure 2.13: (i) It can recombine with another SiH_3 radical on the surface and produce Si_2H_6 molecule or (ii) SiH_3 radicals can make a bond with H atom from the surface, forms SiH_4 and leaves a dangling bond on the surface or (iii) SiH_3 make a chemical bond with the dangling bond and forms strong Si−Si bond.
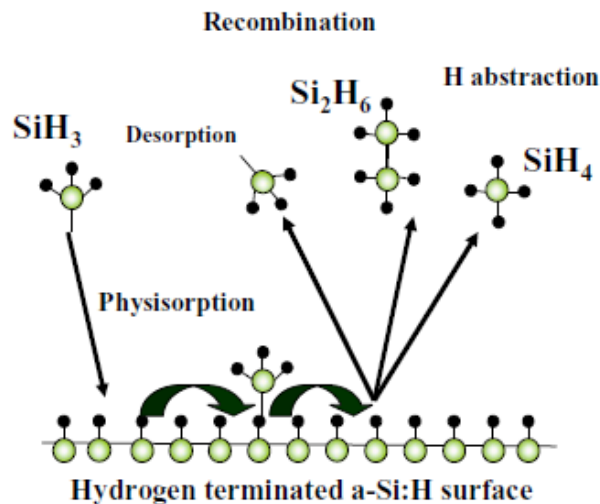
Figure 2.11 Schematic representation of the surface reactions during the growth of a-Si:H where the SiH_3 radicals are the only growth precursors [33-34].
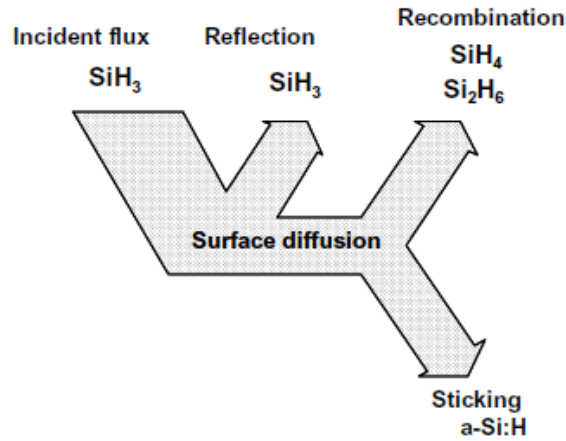
Figure 2.12 Surface reaction processes for on-coming SiH$_3$ radicals [35].
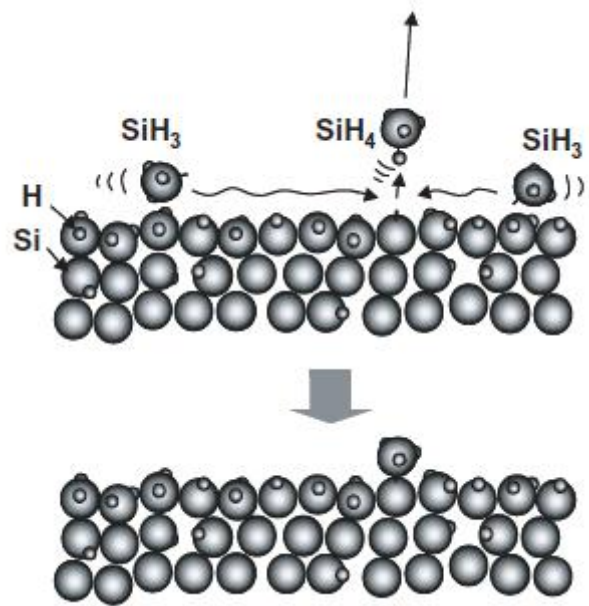
Figure 2.13 Schematic sketch of surface growth process for a-Si:H [35].

2.5 Hydrogenated Amorphous Silicon Doping Process

Doping is addition of the controlled amount of specific impurity atoms to the structure in order to manage the electrical conductivity of the material. The formation of defect compensated donors and acceptors by using phosphorus atoms and boron atoms relatively is the major doping mechanism in a-Si:H [5]. Doping of a-Si:H unavoidably create dangling bonds. This results in doped a-Si:H has a larger defect density than intrinsic a-Si:H in two or three orders of magnitude. The diffusion length of charge carriers in doped a-Si:H is smaller than in single crystal silicon, resulting from the higher

defect density. Accordingly, a-Si:H solar cells are not usable for p-n junction, instead an layer, which has less defect, is inserted between the p type and n type layers.

2.6 Development of a-Si:H/c-Si Heterojunction Solar Cells

The idea of a-Si:H/c-Si heterojunction solar cells was first proposed by Walther Fuhs et al. from the University of Marburg in 1974. Then the first cell was fabricated by Hamakawa et al. in 1985 [36, 33, 37]. Later, many research groups have started to study the amorphous silicon emitter on a silicon wafer and finally the best efficient structure is industrially developed for photovoltaic applications by Sanyo in 1991[36].

In the early studies of Sanyo, p-type a-Si:H layer was deposited directly onto an n-type c-Si wafer in order to form the structure of the heterojunction solar cell as shown in Figure 2. **14**. In this cell structure they have obtained 12.3% efficiency [33].

| TCO |
| (p) a-Si:H |
| (n) c-Si |
| metal |
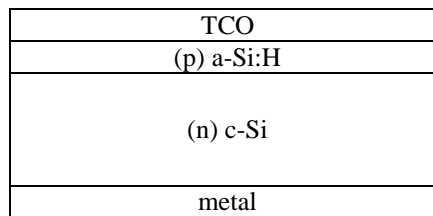
Figure 2. 14 a-Si:H/c-Si solar cell structure in Sanyo [33].

Doping process results in an increase in the defect density in the a-Si:H. With this property, it also results in an icrease in the interface defect density at the s-Si:H/c-Si junction and hence deteriorates cell parameters. In order to get rid of the interface defect-state density, Sanyo start to use very thin intrinsic a-Si:H buffer layers between the wafer and the doped a-Si:H layers as shown in Figure 2. **15**. and named this structure as the "artificially constructed junction-heterojunction with intrinsic thin film (ACJ-HIT) solar cell".

| TCO |
| (p) a-Si:H |
| (i) a-Si:H |
| (n) c-Si |
| metal |
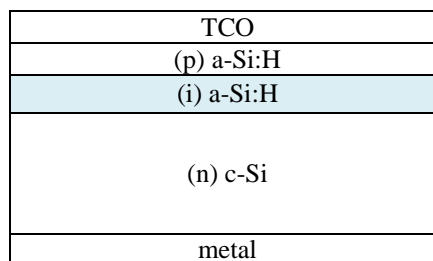
Figure 2. 15 Schematic representation of a single junction a-Si:H/c-Si heterojunction solar cell at Sanyo [25].

With the addition of intrinsic a-Si:H layer into the structure, the maximum efficiency of the cell increased from 12.3% to 14.8% for the 4 nm thick intrinsic a-Si:H layer. With an increase of about 30 mV, it was the opencircuit voltage that especially benefitted from the use of such a buffer layer [38]. It can also be concluded that there is a limitation for the thickness of the intrinsic layer since it decreases both FF and J_{sc} either by acting as a transport barrier with its high resistivity or by the absorption looses.

For further improvement of a-Si:H/c-Si heterojunction solar cell efficiency in time, different studies such as texturizing the wafer surface and introduction of back surface field (BSF) have been performed by different groups. Texturized surfaces cause to increase the average optical path length of the incoming photon and increases the absorption probability of the photon, so the I_{sc}. On the other side, texturizing the wafer surface leads to increase in the total surface area. Since the wafer surface defect density is one of the important parameter, which causes to decrease in efficiency, it is necessary to make the optimization study for the texturing. The inclusion of surface texturing and the BSF enabled a-Si:H/c-Si heterojunction solar cell efficiencies upto 18.1% [25]. Finally, Sanyo introduced a double-sided a-Si:H/c-Si heterojunction solar cell structure and with this new structure they have achieved in an V_{oc} of 0.717 V and efficiency of 21.3%.

Up to now, Sanyo has reached the highest efficiency (23.7%) in the silicon heterojuction solar cells on the 98 μm thick n type c-Si wafer [38]. Although the first solar cell structure is deposited on n-type c-Si wafer, in time p type c-Si wafer is also used as substrate. Device results on n-type substrates and p-type substrates are published by De wolf et al. 2012 in rewiev paper [38] and given in Table 2.1 and Table 2.2.

Table 2.1 Device results on p-type substrates [38].

Affillation	η (%)	V_{oc} (mV)	J_{sc} (mA.cm^{-2})	FF (%)	A (cm^2)	Year
EPFL,Switzerland	19.7	717	37.9	72.7	4, FZ	2011
NREL, USA	19.3	678	36.2	78.6	0.9, FZ	2010
Titech, Japan	19.1	680	36.6	76.9	0.8, FZ	2011
HZB, Germany	18.5	633	36.8	79.1	1	2009
Univ. Stuttgart, Germany	18.1	670	35.7	75.6	2	2010
LPICM, France	17	662	33.0	77.6	25, CZ	2009
ENEA, Italy	17	601	37.1	76.3	2.25	2004
Univ. Hagen, Germany	16.6	655	31.0	81.6	FZ	2009
NCHU, Taiwan	16.4	645	34.8	73.0	1	2008
IMEC, Belgium	16.4	644			1, FZ	2005
Univ. of Valencia, Spain	15.2	591	33.8	77.6	1, CZ	2010
CAS, China	15.1	585	34.6	74.7	<1, CZ	2009
Ultrecht Univ., the Netherlands	14.9	571	33.3	78	1, FZ	2005
UPC, Spain	14.5	613	30.3	77.9	FZ	2008
SUNY, USA	10.6	550	30	64	0.03	1997

Table 2.2 Device results on n-type substrates [38].

Affiliation	η (%)	V_{oc} (mV)	J_{sc} (mA.cm^{-2})	FF (%)	A (cm^2)	Year
Sanyo, Japan	23.7	745	39.4	80.9	100, CZ	2011
Kaneka, Japan	22.1	729	38.5	79.1	~220, CZ	2011
RRS,Switzerland	21.9	735	38.5	77.5	4, CZ	2011
EPFL,Switzerland	21.8	726	37.8	79.7	4, FZ	2011
HHI, Korea	21.1	721	36.6	79.9	~220	2011
CEA-INES, France	21	732	36.9	78.3	105, FZ	2011
CIC, Japan	20	685	36.9	79.2	243, CZ	2011
HZB, Germany	19.8	639	39.3	78.9	1, FZ	2006
NTUST, Taiwan	19.6	690	39.1	72.7	1, FZ	2011
Univ. Hagen, Germany	19.3	675	37	77.3	FZ	2009
FhG-ISE, Germany	18.7	~705	~35	~75	4, FZ	2010
IEC, USA	18.3	694	35.7	74.2	0.55, CZ	2008
LG, Korea	18.2	687	33.3	78.9	1, FZ	2010
NREL, USA	18.2	694			0.9	2009
Titech, Japan	17.9	671	35.2	76	<1, CZ	2008
Sungkyunkwan Uni.,Korea	17.5	656	35.6	75	0.2	2009
LPICM, France	17.4	631	36.3	76.1	CZ	2011
Ultrecht Univ., the Netherlands	17.2	701	30.8	79.6	4	2011
CNR-IMM, Italy	16.2	573	36.6	77	1, CZ	2005
Delf Univ., the Netherlands	15.8	646	32.9	74.3	FZ	2011
Univ. Toronto, Canada	15.5	679	31.7	72.4	4.2, FZ	2011
Kyung Hee Univ. Korea	14	575	34.4	71	CZ	2011
ECN, the Netherlands	13.2	635	29.1	72	21, FZ	2010
KIER, Korea	12.8	<600				2009
ENEA, Italy	12.4	526	31.9	74	mc	2010
UPC, Spain	10.9	525	28.6	72.8	FZ	2006

During this thesis studies, we have used 72 cm^2 (large area) (100) oriented, one side polished, CZ, (p) c-Si wafers as a substrate. When looking the active area value of the working groups given in Table 2.1, for the device results on p-type substrates, the major importance of this thesis studies can be easily understood having the highest active area studied so far on the p- type substrates.

The main motivation for the study of a-Si:H/c-Si heterojunction solar cell structure is that there is still on going studies for the further imrovement of the efficiency by focusing on [33]:
   i)   Limitations in the J_{sc}, created by the optical losses
   ii)   Limitations in the V_{oc}, created by the recombination losses
   iii) Limitations in the FF, created by the resistance losses.

These losses and their possible solutions are schematically introduced in Figure 2. **16** and outlined as follows:

In order to decrease the optical losses, one of the possible solutions could be the texturizing the surface of the wafers to obtain efficient light trapping. Another solution is optimization of each layer, including TCO and a-Si:H, in order to decrease the absorption and the aspect ratio of the grid electrodes could be increased by reducing the shaded area.

For the minimization of recombination losses one of the main parameter is the cleaning of the wafer surface before the a-Si:H deposition. With a suitable wafer surface cleaning, it is possible to decrease the number of recombination centers and interface defect-state density in an important amount.

The resistance losses can be prevented by reducing the device series resistance of both highly conductive TCO and good ohmic contacts.
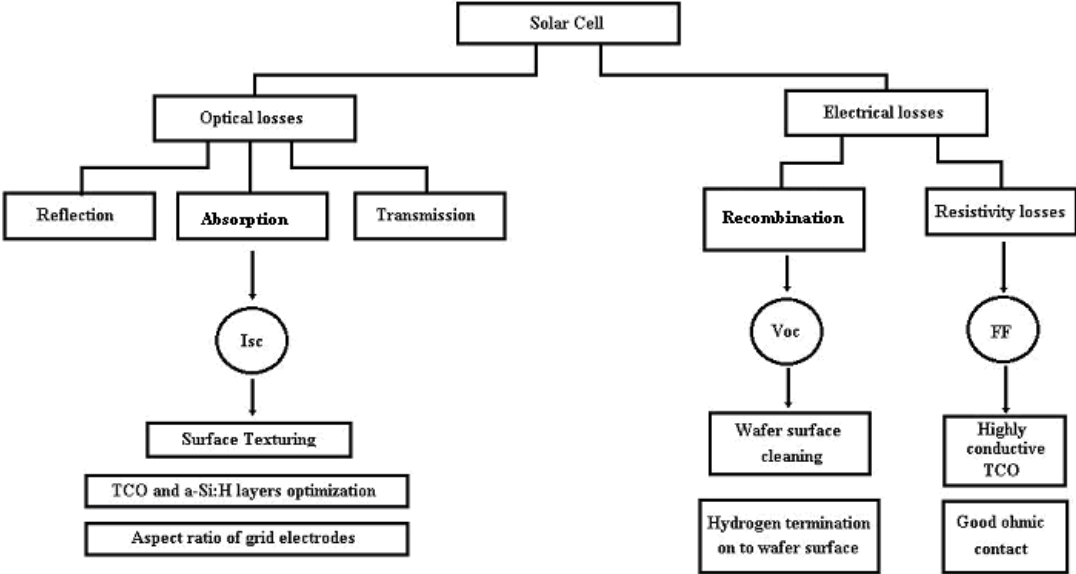
Figure 2. 16 Losses sources in heterojunction silicon solar cells.

Additionally, one can also see the impact of each layers and interfaces (defined in Figure 2. **17**) to the solar cell parameters in Table 2.3.

20
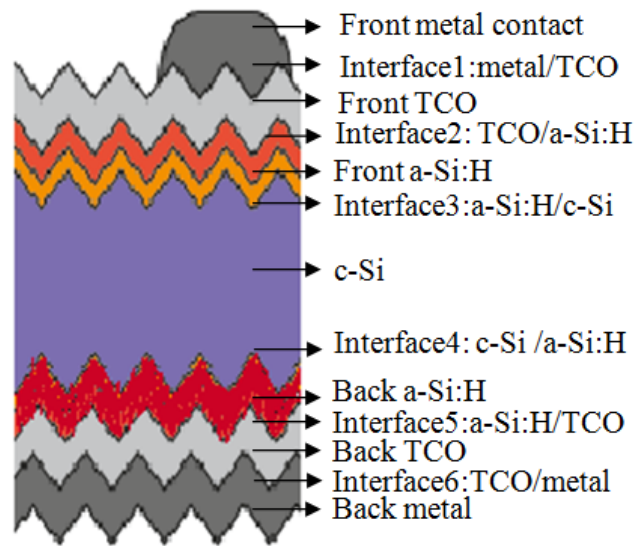
Figure 2. 17 Structure of a double side heterojunction solar cell.

Table 2.3 Qualitative impact of each layers and interfaces in the heterojunction solar cell on the cell parameters [33].

Layer	Voc	Isc	FF
Front metal grid	-	●●●	●●●
1st Interface: metal/TCO	-	●	●●
Front TCO	●	●●●	●●●
2nd Interface: TCO/a-Si:H	●	●	●●
Front a-Si:H	●●	●●●	●●
3rd Interface: a-Si:H/c-Si	●●●	-	●●
c-Si	●●	●●●	●
4th Interface:c-Si/a-Si:H	●●●	-	●
Back a-Si:H	●●	-	●
5th Interface: a-Si:H/TCO	●	●	●
Back TCO	●	●	●
6th Interface: TCO/metal	-	●	●●
Back metal	-	●	●●

●●●: most effective
●●: more effective
●: moderate effective.

2.7 Epitaxial Growth Discussions and Annealing Dynamics

It is well known that the crystallinity of the deposited Si layer is highly sensitive to the deposition temperature and crystal orientation of the substrate [39]. For instance, while there is an epitaxial growth on (100) substrate at around 200°C, the film is essentially a-Si:H on a (111) substrate at the same temperature [39-41], (see Figure 2.18). When the substrate temperature inreased further, epitaxial growth starts on (111) substrates also. Keep in mind that thin undoped epitaxial underlayer does not passivate well the surface and lifetime improvement cannot accomplished upon annealing when the film was not purely amorphous [34, 42-43].
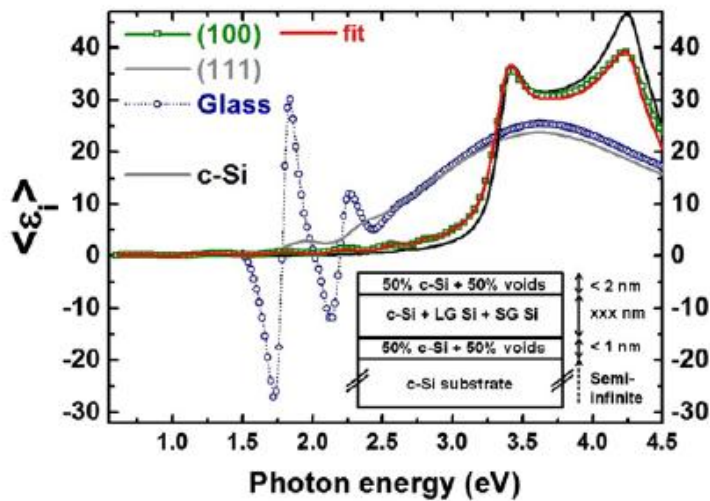
Figure 2.18 ε_i variation of silicon thin films with photon energy, deposited on Corning glass, (100) c-Si and (111) c-Si substrates [41].

Caborracas et al. [41] have studied the reason for the deposition of amorphous structure on c-Si (111) and epitaxial on c-Si (100). They have observed a certain link between the hydrogen content and the structure of the deposited films like that there is more than order of magnitude difference between the hydrogen content of the deposited amorphous film and that of the epitaxial film (Figure 2.19). They have suggested that the growth process enables to get rid of hydrogen or succeeds in avoiding the incorporation of hydrogen in or at the surface of the film.
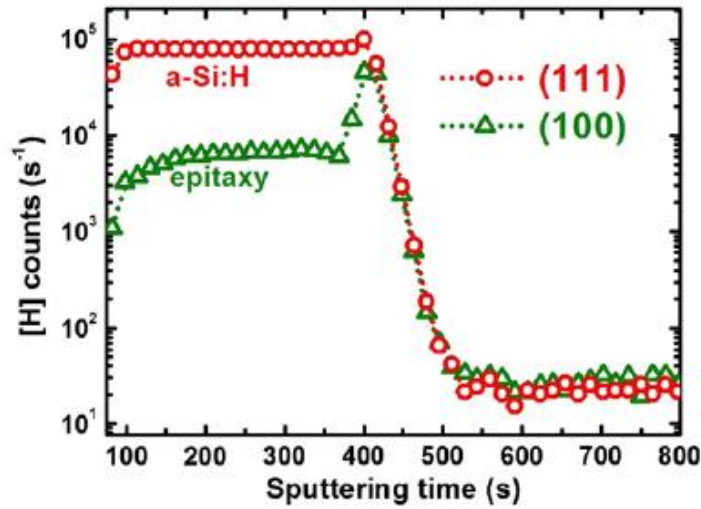
Figure 2.19 SIMS results of hydrogen in silicon thin films co-deposited at 175 °C on (111) and (100) c-Si substrates [41].

In order to overcome the epitaxial growth and hence getting a better surface passivation of c-Si wafers numerous studies has been performed. Some of the indications of these good surfaces are hydrogen rich and atomically abrupt a-Si:H/c-Si interface.

Fujiwara et al. [42] have observed that intrinsic layer was partially epitaxial for the substrate temperature (T_{subs}) in between 140 and 180 °C. For $T_{subs} \geq 180$ °C, the i layer became completely epitaxial. They have also found that the phase structure of the i layer was strongly dependent on the resistivity of c-Si substrates. In particular, a-Si:H growth occured when the resistivity of c-Si is high (1000 Ω cm), whereas for c-Si layers having smaller resistivity values like 0.5 Ωcm, epi-Si growth occurs at high substrate temperatures. Main difference caused by the effect of ion bombardment in PECVD. For the case of the highly resistive substrates, the substrate surface was charged negatively, which enhanced ion bombardment that displaced atoms in crystal sites. To verify the effect of ion bombardment on the deposited samples, they have fabricated the solar cell devices at different rf power values and growth temperatures of at 130 °C and 180 °C. From Figure 2.20, they have observed that when P_{rf} was low, the epitaxial growth of the i layer formed at both temperatures due to the decrease in the ion bombardment and this epitaxial growth caused to the large decrease in V_{oc}. At high P_{rf}, the solar cell efficiency also reduced, although the film layer structures were amorphous. They offered two possible reason in reduction of V_{oc} at high P_{rf} either (i) enhanced plasma damage to the c-Si substrate or (ii) increase in defect density in the a-Si:H layers by the ion bombardment. Thus, they have concluded that the optimum P_{rf} locates near the phase boundary of the epi-Si/a-Si:H growth.
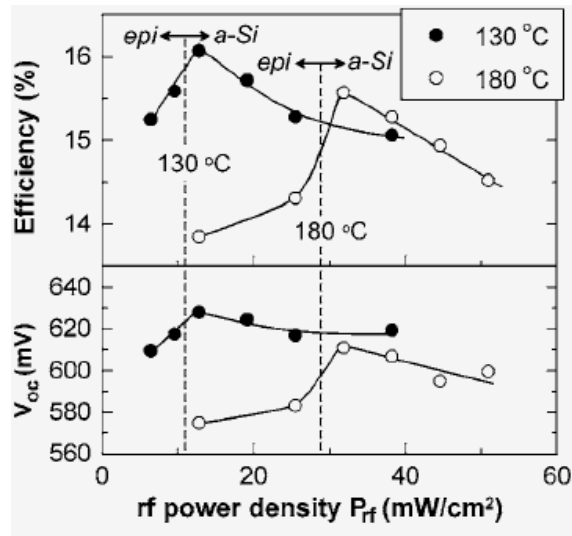
Figure 2.20 Efficiency and V_{oc} variations of the a-Si:H/c-Si solar cell, plotted as a function of rf power density P_{rf}.

Additionally, the solar cell efficiency at various growth temperatures, T_G and P_{rf} were summarized by Fujiwara et al. [44] as shown in Figure 2.21. They found that the epi-Si/a-Si:H phases are separated by a straight line and epi-Si growth occured at high T_G and low P_{rf}. Moreover, they have obtained the higher efficiencies when a-Si:H layers were grown near the phase boundary. Furthermore, yielding higher growth rates, the epi-Si growth was avoided at high deposition pressures, since ion bombardment becomes weaker at high pressure. This suggests that at high pressures there occurs a higher growth rates and this prevent the epitaxial growth within the structure of the deposited film.
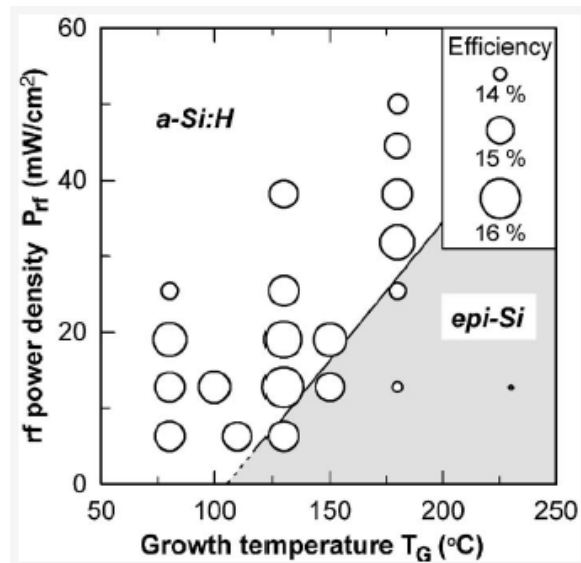
Figure 2.21 Solar cell efficiency distributions obtained at different growth temperatures and rf power densities [44].

24

Epitaxial free films can also be produced below the optimum temperature with an additional annealing step for recovering [39, 45-48], contrary to Fujiwara [44] methods. These studies have been performed by different groups. For example Pysch et al. [45] have studied the influence of annealing on V_{oc}. Results of their studies are given in the Figure 2.22. The HJ cells reach the saturation region for a V_{oc} in a shorter time interval as the annealing temperature becomes higher. Moreover, for T_{anneal}: 100°C insignificant change of the V_{oc} was observed. This means that the hydrogen diffusion starts at around 150°C, which was in good agreement with the R. A. Street et al. [6]; stating that a hydrogen diffusion is initiated at temperature values in between 130 and 150°C, depending on phosphorous doping concentration.

Remarkably, a decrease in the V_{oc} was observed for an additional annealing step of 60 min at 350 °C. This was attributed to the fact that hydrogen is depleted from the interface. This results in an increase in the interface defect density at the interface and leads to a lower the passivation quality.
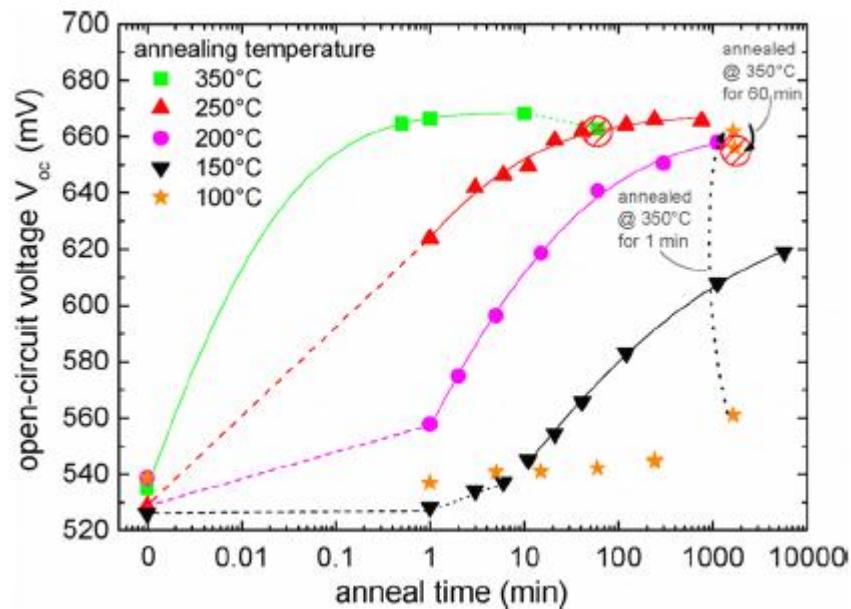
Figure 2.22 The open-circuit voltage variation with respect to annealing time at different annealing temperatures [45].

Several techniques were offered to explain the reasons of positive contribution of annealing to the properties of thin intrinsic a-Si:H films. Most of the groups have studied on effective lifetime as a function of annealing [43, 49-51]. They have confirmed that a minimum thickness was required for obtaining an improvement owing to annealing. In addition, they have suggested that a minimum amount of hydrogen was necessary to passivate the interface, and/or a certain density of film was needed to prevent effusion of hydrogen from the film. The first explanation states that if the film is thinner than enough, insufficient amount of hydrogen is present within the structure to accomplish to improvement. In the second and third cases, hydrogen occupying in certain states within the thin film will be used to passivate dangling bonds at the interface.

The diffusion of hydrogen from the a-Si:H layer to the c-Si surface is important for obtaining a better surface passivation and increasing solar cell performance. In the early studies, as an explanation of the surface passivation it was assumed that the hydrogen diffused from the thin film bulk layer to the c-Si surface. Neverthless; since 2.49 eV energy is the minimum energy necessary to release the bonded hydrogen, it must already be in either a free or a quasi-free state [52]. Since there are high density of dangling bonds, it is not possible to be free of hydrogen in the structure. Additionally low temperature thermal annealing and a relatively high defect density $10^{15}-10^{17}$ cm^{-3} would considerably prevent a bulk diffusion of hydrogen to the interface for surface passivation [52].

Mitchell et al. [52] have calculated 0.7±0.1 eV activation energy for the surface passivation, independent of the bulk layer thickness and they have concluded that the lower activation energy value indicating surface passivation is controlled by surfaces states, instead of bulk diffusion processes. Annealing process leads rearrangement of the hydrogen, which is already present at the interface either prior to deposition (HF-dip step) or else from the hydrogen deposited during the initial stages of deposition.

De Wolf and Kondo [53] have observed no lifetime improvement upon annealing when the growth was not purely amorphous. Similar results have also observed by Labrune [34], as shown in Figure 2.23.
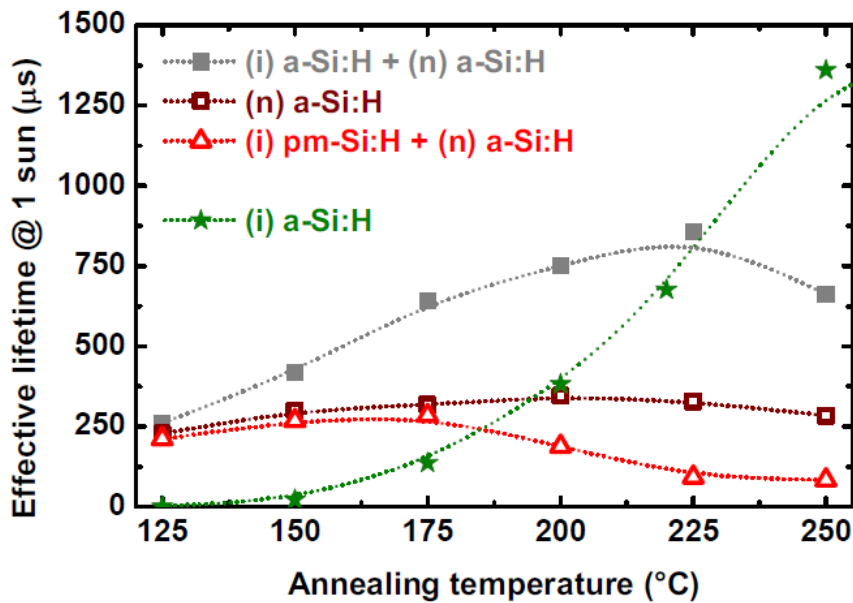
Figure 2.23 Effective lifetime at 1 sun on (n) c–Si with different structures.

2.8 Band Diagram and the role of the (i)a-Si:H layer on (n)a-Si:H/ (p)c-Si Heterojunction Interface

Figure 2.24 shows the band diagram of (n) a-Si:H/ (p) c-Si heterojunction structure. Due to the large band offset in the valance band, the emitter behaves as a barrier for holes. On the other hand, electrons can pass through the small conduction band offset, creating electron hole pair seperation. Thus an electric field is created at the heterojunction.

26

The field forces positively charged holes away from the interface and accelerates the electrons towards the front contact. Even though the band offsets at the junction form barriers for both electrons and holes; the conduction band offset is small enough to allow transport of electrons across the interface.

In the Figure 2.24 ΔE_c and ΔE_v terms are band offsets for conduction and valance bands respectively. Band offset is created by the band gap differences of the materials forming the heterostructure [7]. It has critical importance on the electronic transport of the carriers across the junction.

It is well known that in amorphous material the defect density increases with dopant concentration. Moreover, due to the nucleation and mechanical stress that take place at beginning of the growth; the defect density of the amorphous silicon close to the interface can be larger than that of the bulk amorphous material. In order to improve the interface; intrinsic a-Si:H thin layer is deposited between crystalline and amorphous doped materials since there is lower defect density distribution within the intrinsic a-Si:H bandgap.
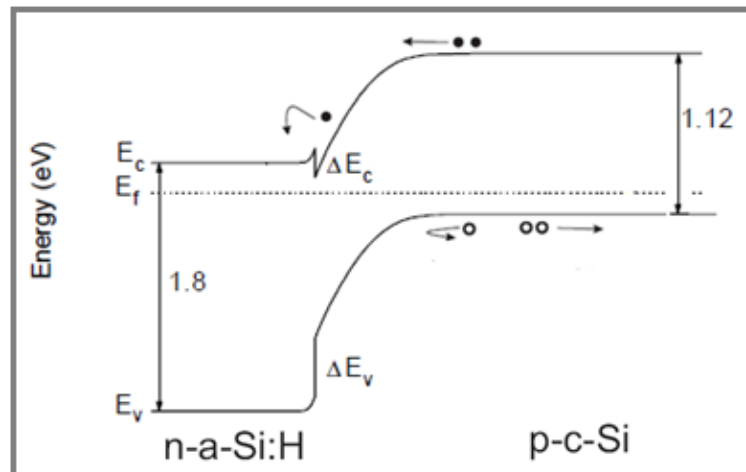
Figure 2.24 Energy bandgap diagram for (n) a-Si:H/(p) c-Si heterojunction interface [2].

As the conductivity of the intrinsic layer is low, the intrinsic layer has to be as thin as possible to ensure a low series resistance. On the other hand, for obtaining the interface passivation and achieving high performance a-Si:H/c-Si solar cells, it has to be inserted to the cell structure. When the thickness of (i) a-si:H layer increases, the number of recombinations will increase as well. Therefore, increase in the thickness does not mean the increase in the photon generated pair collection, even though it necessarily increase the photon-generation process rate [5, 36, 54-55].
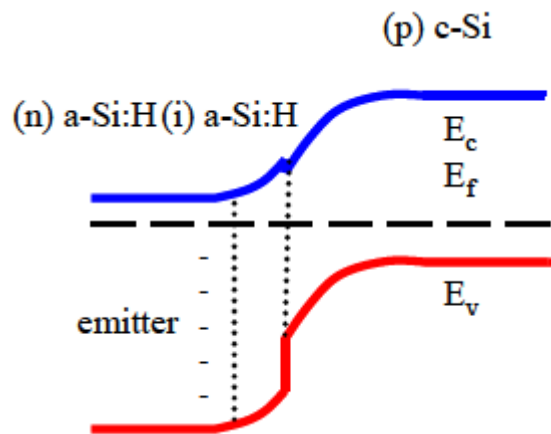
Figure 2.25 Band diagram sketch of a (n) a-Si:H/ (i) a-Si:H/ (p) c-Si heterojunction interface [36].

In the case of (n) a-Si:H/(i) a-Si:H/(p) c-Si structure (Figure 2.25), the collection of electrons generated in (p) c-Si side is only blocked by the small band offset in the conduction band edges. With this small barrier, minority carrier collection is easier than before.

Beside the front surface passivation, for improving the back surface passivation, intrinsic buffer layer is deposited between the c-si wafer and the doped a-Si:H layer in the SHJ solar cell structures as shown in Figure 2.26 below.

At the back surface, while the holes are accelerated by the electric field that enhanced the hole transport to the back, they have to overcome the barrier ΔE_v in the valance band at the interface to get into the intrinsic a-Si:H (Figure 2.27).
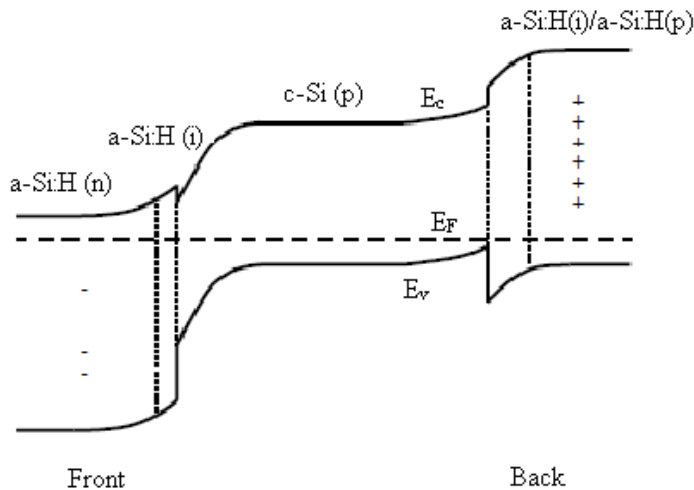
Figure 2.26 Band diagram sketch of a double side SHJ solar cell on (p) c-Si wafer [40].

28

The high valence band offset might be expected to prevent holes from moving freely to the a-Si:H p-layer. However, holes can pass through the barrier at the a-Si:H p-layer by tunneling, hopping, or thermally assisted tunneling [56].
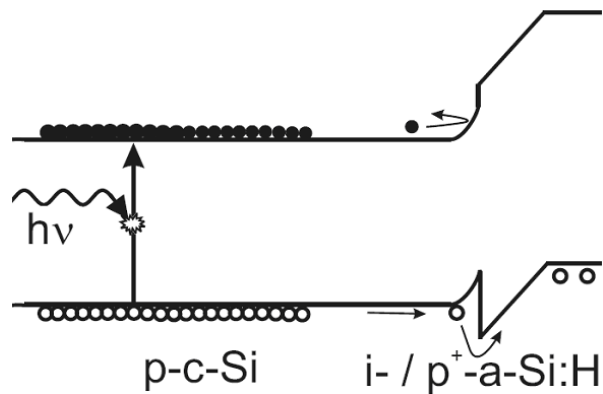
Figure 2.27 Band diagram sketch of a (p) c-Si wafer/ (i) a-Si:H/(p$^+$) a-Si:H heterostructure [2].

The alignment of the Fermi levels between a-Si:H (~1.7 eV) and c-Si (1.12 eV) both inverts the surface and creates an energy barrier at the interface. The quality of interface is once more important in that, otherwise the energy barrier might impede the transport of photogenerated carriers across the interface, lowering the fill factor, and resulting an S-shaped J-V curve for the solar cell device [57]. For a-Si:H / c-Si solar cell, band alignment and values of band offsets strongly depend on the deposition method, process conditions, and the c-Si wafer pre-cleaning. Hence, optimization should be applied to avoid the S-shaped in J-V curves.

"S"-shape characteristic can be observed for Si heterojunction cells fabricated on both p- and n-type c-Si wafers, with or without intrinsic buffer layers, and it has been reported by many other groups [58-59]. The researchers have ascribed the S-shape curve to various explanations like that including carrier recombination at the interface defects [34,60], recombination in the c-Si depletion region [45], offset in valence and conduction bands [45], and non-Ohmic electrode contacts, including both front contacts and the rear contacts could result in low FF and S-shape J-V curve.

CHAPTER 3

EXPERIMENTAL TECHNIQUES

In this chapter, experimental techniques used in the study of this dissertation will be presented, those includes a-Si:H/c-Si heterojunction solar cell fabrication process using the ultra high vacuum Plasma Enhanced Chemical Vapour Deposition (UHV-PECVD) technique; the material characterization techniques used to characterize related structural, electrical and optical properties; and finally the device analysis tools to investigate solar cell performance.

3.1 Plasma Enhanced Chemical Vapor Deposition System

In the plasma enhanced chemical vapor deposition technique, silane gas (SiH_4) is excited by a radio-frequent (RF, 13.56 MHz) plasma, which causes silane molecules to dissociate. Later on, dissociation products are deposited on heated substrates and generate a layer.

An important advantage of PECVD deposition is that the deposition temperature of device is usually in between 200 ^{o}C – 300 ^{o}C. The low temperature process allows the use of a variety of low cost materials as a substrate, such as glass, stainless steel and flexible plastic foils.

Another main advantage of the PECVD system is that one can deposit a-Si:H layers in the same system without exposing samples to air contamination.

3.1.1 UHV-PECVD System for a-Si:H Deposition

The schematic representation of a PECVD deposition system is given Figure 3.1. Main part of a deposition system contains a stainless steel vacuum chamber evacuated by a pumping unit to 10^{-9} Torr with the aid of turbo molecular pumps and mechanical pumps. With the help of a multichamber system exchange of residual gases between successive depositions will significantly be decreased and very sharp interfaces can be made [18]. Additionally, the use of a load-lock system guarantees the quality of the background vacuum, and thus lowers the contamination in the bulk layers. All chambers seal with valves, windows, gas-supply lines, and Conflat connections, ensuring the vacuum to be of ultra high vacuum quality.

The process gas mixture is introduced by Mass Flow Controllers and the pressure inside the chamber is kept constant by a throttle gate valves and precise mass flow controllers.

Plasma is ignited by by means of a RF power supply connected to the reactor via appropriate RF circuitry (matchboxes); process gas is decomposed in ions and radicals, which are then deposited as thin films.

Most of the gases used are hazardous, i.e., they can be corrosive, flammable, explosive, and/or highly toxic. Therefore, extreme care has to be taken in dealing with these gases. An exhaust system is designed to safely handle the exhaust process gases.

Finally, there is a control panel, which monitors and controls all the chamber pressure, chamber temperature, gas flow rate and RF power.
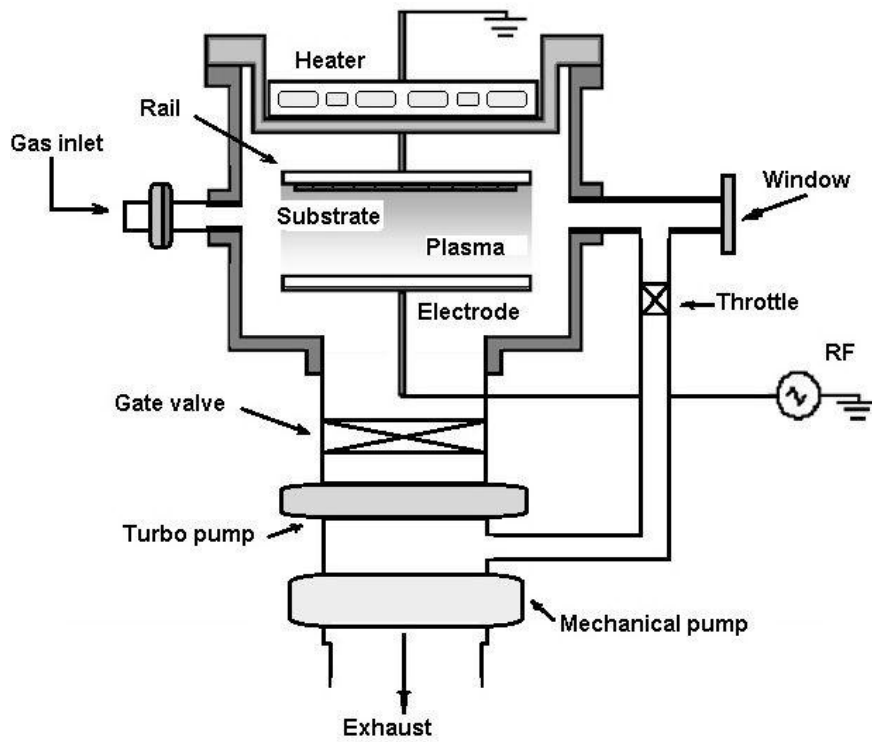
Figure 3.1 The schematic representation of a PECVD deposition system

Ultra high vacuum Plasma Enhanced Chemical Vapor Deposition system at TUBITAK UME is shown in Figure 3.2. The system consists of two capacitively coupled plasma chambers for the deposition of intrinsic and doped a-Si:H films and a load lock unit. The separation of the chambers is essential to fabricate high quality intrinsic films and cross-doping of n and p-type [2].

Figure 3.2: TUBITAK UME UHV-PECVD System

3.2 Deposition Chamber Cleaning

For the deposition chamber cleaning, we have used NF_3 gas as a dry etching. The most important advantage of NF_3 with respect to CF_4 and SF_6 is that it does not release undesirable species, such as C or S contaminants for the subsequent a-Si:H deposition.

A 15 minute pre-deposition of SiH_4 plasma before inserting wafers in the chamber for the deposition has been performed after each NF_3 cleaning process.

3.3 Heterojunction Fabrication

Figure 3.3 shows a sketch of the c-Si/a-Si:H solar cell preparation sequence. The p/n junction of the p type substrate heterojunction with intrinsic thin layer solar cell is formed by the n type amorphous silicon layer and the p-type crystalline silicon substrate. To passivate the interface of the heterojunction, an intrinsic amorphous silicon thin layer is inserted between the highly doped layer and the substrate, which greatly improves the performance of the solar cells and forms the so-called HIT structure.

All solar cells prepared in this work are deposited on p type, CZ, <100> c-Si wafer substrates. Once the wet chemical Radio Corporation of America (RCA) cleaning had been completed, the samples were immersed in a piranha solution (H_2SO_4:H_2O_2) (1:1) for 10 minutes to grow a chemical oxide. After rinsing the wafers in de-ionized water, for the etching of the native silicon oxide on the surface, wafers were dipped into 1% dilute HF solution for a 60 seconds. Following the rinsing in de-ionized water, wafers were immediately inserted into the chamber in order to prevent the oxidation of the surface. In the chamber, after desired deposition conditions were achieved, intrinsic and n doped a-Si:H layers were deposited respectively. The deposition parameters used were: 12 mW/cm^2 RF power density; 225 °C temperature; 0.6 Torr pressure; 40 sccm SiH_4 flow for intrinsic layer and for the n-doped layer 20 sccm PH_3 has been added in the mixture.

Thereafter a transparent conductive oxide (TCO) layer was deposited on the top of the n doped a-Si:H layer by sputtering method. Back and grid shape front contacts are supplied by thermal evaporation of aluminum. Before back contact deposition, back surface of the wafer was etched in the 2% HF once more upto obtaining the hydrophobic surface (2.5 min)
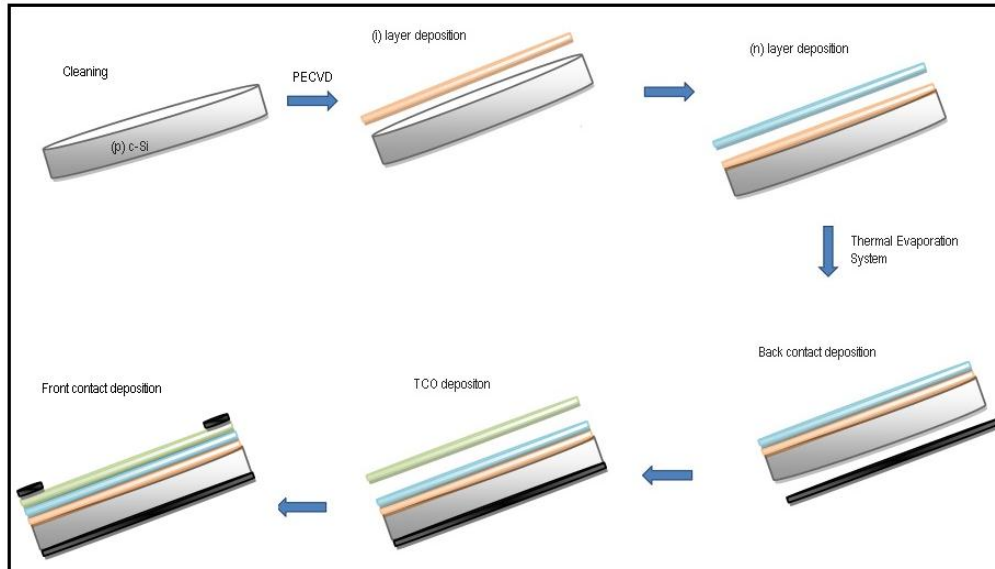
Figure 3.3: Sketch of the preparation sequence of c-Si/a-Si:H cell devices equipped with heterojunction emitters.

3.3.1 Substrate Surface Cleaning Studies

Since the substrate surface is directly a part of the electronic interface; it is very important to substrate surface cleaning process for the preparation of defect free surfaces before the a-Si:H layer deposition for the a-Si:H/c-Si heterojunction solar cell structure. Especially for this heterojunction solar cells, final aim of the cleaning pre-treatment has to be the removal of damaged regions of the silicon surface and the saturation of dangling bonds at the surface and near-surface region by H-termination [61].

Substrate surface cleaning processes can be cathegorized basically as wet chemical etching in hydrofluoric acid solutions [61-65] and dry cleaning procedures [66-67].

3.3.1.1 Wet-chemical method:

For the chamber parameters determination studies instead of using the expensive RCA cleaning process, we have used the modifying cleaning process that prevents the chemical and time consumption. For this purposes, we have used the following cleaning procedure, taken from [63]:

- Immersing into acetone for 10 min
- Rinsing with DI water for 1 min
- Immersing into IPA for 10 min
- Rinsing with DI water for 1min
- Immersing into %5 HF for 10 sec
- Rinsing with DI water for 1min

Later on, in order to study the pre-cleaning effect on to the solar cell structure we have changed the wafer cleaning procedure according to Angermann's paper [61]. According to the Angermann wet-chemical cleaning and smoothing procedures generally include two essential steps:

i- the formation of a silicon/silicon-oxide interface by oxidising agents,
ii- the subsequent removal of the so-prepared oxide layers by HF- or NH_4F-containing solutions.

In this cleaning procedure, wafers were cleaned by the conventional cleaning method of the RCA details of which is given in Table 3.1. Angermann has studied the density of interface states, D_{it}, after different cleaning treatments. He concluded that two steps of standard RCA I and RCA II processes had been confirmed to remove particles such as organic and metallic surface contaminations, but there still high densities of interface states after RCA treatments, as demonstrated in Figure 3.4. He concluded that the minimum interface state density can be achieved by two final chemical processes: the wet-chemical oxidation of the surface and the silicon oxide removal.

Table 3.1 The standard cleaning process of the Radio Corporation of America (RCA process) [61]

Solution	Composition	Contamination
RCA I	$H_2O:NH_4OH:H_2O_2$	Particles, organic materials and metals
HF dip	$HF:H_2O$	Native oxide
RCA II	$H_2O:HCl:H_2O_2$	Atoms and ions

Referring to their studies, we have decided our cleaning procedure for flat Si (100) wafer surfaces as the following steps:

- Standard RCA cleaning
- Rinsing with DI water for 1min
- Immersing into $H_2SO_4:H_2O_2$ (1:1) 10 min (wet chemical oxidation, for smooting)
- Rinsing with DI water for 1min
- Immersing into %1 HF 60 s (for oxide removal)
- Rinsing with DI water for 1min
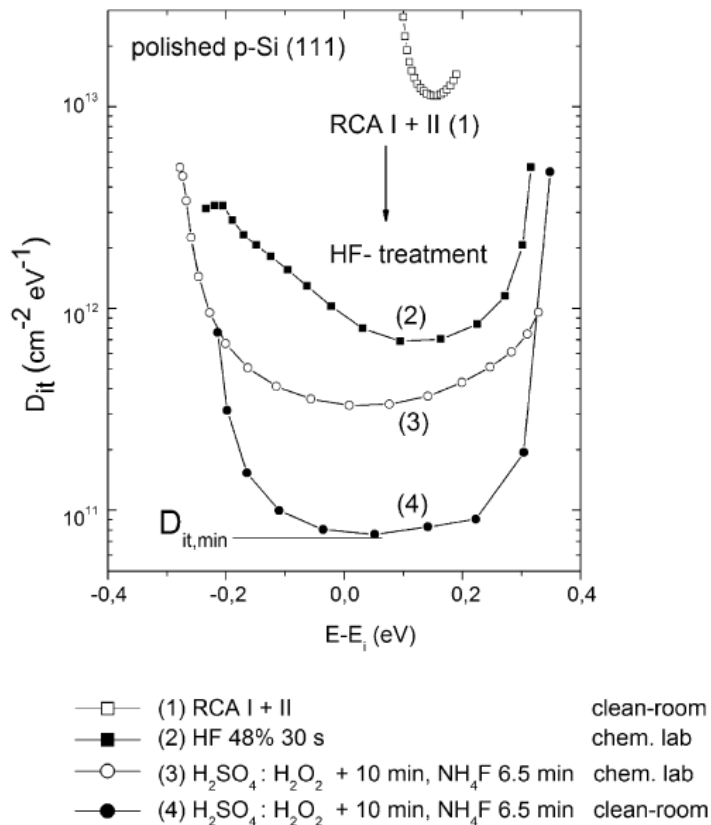
Figure 3.4 Interface state density curves for p-type Si(111) surfaces obtained after different cleaning procedures [61].

3.3.1.2 Dry Cleaning Procedure:

H_2, CF_4/O_2 and NF_3 are commonly used gasses for the plasma treatments on to the substrate surface [67]. Although it is considered that dry cleaning procedures are more favorable than that of the wet chemical treatments, in which there is large amount of chemical consumption, there is the fact that the plasma treatment can damage the crystalline surface [67].

3.3.2 Zinc Oxide Layer Deposition

Since it will collect the photo-created charge carriers towards the metallic contact, the selected transparent conductive oxide (TCO) layers require high electrical conductivity. Besides, it must be highly transparent to let most light enter the solar cell. In order to improve the efficiency of TCO layers, they must be optimized in terms of transparency, conductivity and uniformity.

In this work for the deposition of TCO films, RF magnetron sputtering system has been used. We have focused on optimizing the main deposition parameters such as; plasma power, target to substrate distance, process pressure, process temperature and gas flow rate.

Firstly, ZnO target was used as a target material for TCO deposition. Deposition conditions can be summarized as: plasma power between 150 to 180 W; target to substrate distance between 35 to 70 mm; process pressure 10^{-2} Torr; Ar flow rate 5 sccm and deposition was performed at room temperature. Moreover, similar studies will be carried on for the ZnO:Al substrates.

3.3.3 Front and Back Contact Deposition

In order to get the high device performance from the fabricated solar cell, it is necessary for front electrode to fulfill some requirements. First, electrical conductivity of the front electrode must be high enough to reduce the series resistance of the solar cell. Additionally, it must have a high transparency and it is necessary that the deposition technique of the front electrode must be not to damage the underlying heterojunction emitter surface [36].

Front electrode used during these studies contains 1.9 mm, 2 busbar and a number of 150 μm wide fingers.

Aluminum is widely used as a contact metal in microelectronic as well as in macroelectronic industries such as the photovoltaic industry [68]. During this thesis studies we have used full area Al metallization for the back and front contacts.

3.4 Material and Device Characterization

Various techniques have been used to characterize material properties in this dissertation. Scanning Electron Microscope (SEM) is used to investigate the surface uniformity and thickness properties of the samples; composition analysis was done by energy dispersive spectrum (EDS) integrated in SEM system. Optical properties, structural properties and the thickness of the films are determined from Spectroscopic Ellipsometry measurements. TEM measurements revealed the crystallinity, crystal structure, thickness and orientation of films. AFM measurements have been performed for the surface roughness determination. For the defect detection in solar cells, mainly cracks, broken fingers in the front metallization electroluminescence measurement is used. FTIR analyses is used to determine the hydrogen concentration of the deposited films and finally I-V measuremens have been performed for the determination of efficiency, V_{oc}, I_{sc} and FF values of the deposited solar cells under 1000 mW/cm^2 AM 1.5G illumination under standart test conditions (STC), mainly at 25 ^{o}C. Each characterization technique will be briefly discussed in the following.

3.4.1 Spectroscopic Ellipsometry Measurements

Spectroscopic ellipsometry is an optical technique used for the determination of optical properties and thickness of thin films. It measures the change in polarization state of light after being reflected on the material surface or transmitted through the material. Two main advantages of this measurement system are that it is fast and non-destructive [36]. In Figure 3.5 you can see a picture of Jovin Yvon UVISEL Spectroscopic Ellipsometer measurement system used in this thesis.

System contains Xenon arc lamp as light source (75 Watt), polarization generator, modulator, polarization analyzer and a detector. Light enters the polarizer by fiber optic cables Figure 3.6. The polarizer defines the state of polarization of the incoming light before it strikes on the sample surface. The polarization modulator changes the polarization state by varying the ellipticity of the polarization as a function of time [36,69]. Then, the polarization of the reflected beam is analyzed by another polarizer, analyzer. After analyzer, light passes through the monochromator and then detected by the detectors depending on the spectral range such as photomultipliers for the UV and visible range and InGaAs detector for the IR spectral range. The detector transforms light into the electronic signal for detecting the reflected polarization. Obtained polarization is compared to the known input polarization to determine the variation in polarization, caused by the sample reflection. This is the ellipsometry measurement of the Psi (Ψ) and Delta (Δ).
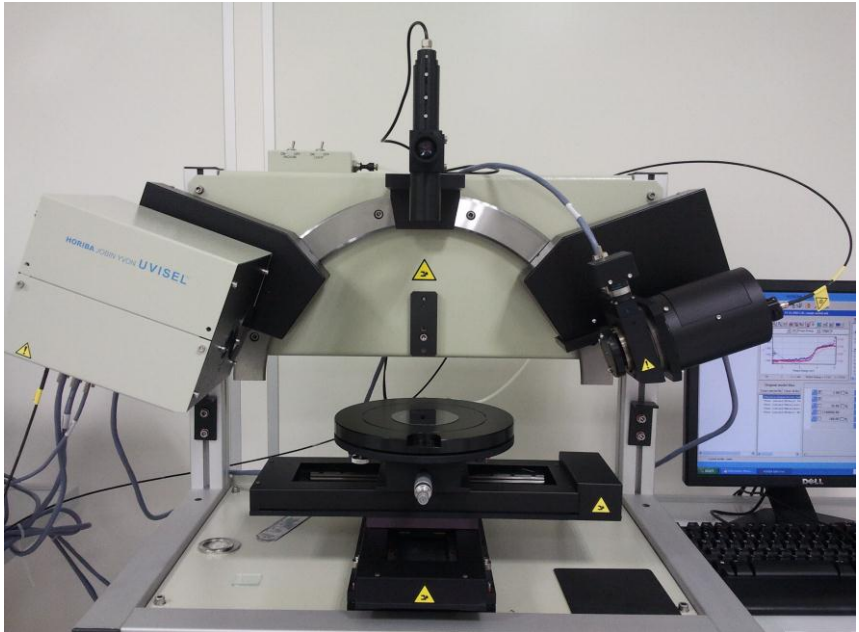
Figure 3.5 TUBITAK UME Jovin Yvon UVISEL Spectroscopic Ellipsometer measurement system
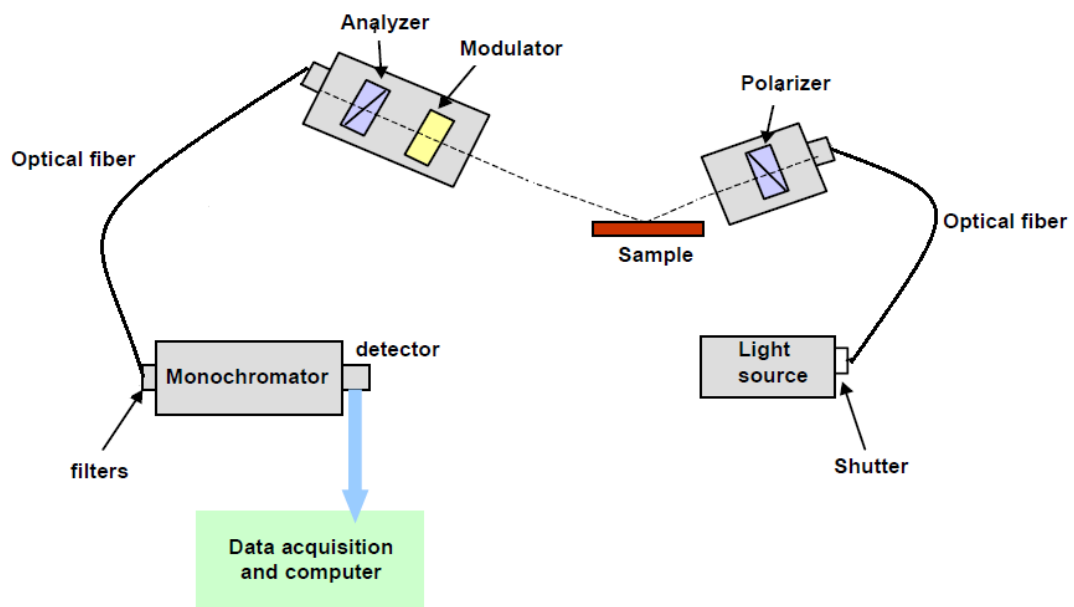
Figure 3.6 Schematic of the Spectroscopic Ellipsometer measurement system [69]

Ellipsometry measurements are based on the measurement of the pseudo-dielectric function <ε> of the material [36]:

$$\langle\varepsilon(\omega)\rangle = \sin^2\theta_0\left(1+\left(\frac{1-\rho}{1+\rho}\right)^2\tan^2\theta_0\right) = \langle\varepsilon_1(\omega)\rangle + i\langle\varepsilon_2(\omega)\rangle \qquad (3.1)$$

where ρ is obtained by measuring the state of polarization of the reflected beam. The measured values are expressed in the following equation, known as the fundamental equation of ellipsometry [69]:

$$\rho = \frac{r_p}{r_s} = \tan(\psi)\exp(i\Delta) \qquad (3.2)$$

An ellipsometric experiment follows the procedure:

i- The measurement contains the ellipsometric angles Ψ and Δ data,
ii- A model is defined for the sample to determine the sample parameters,
iii- Once the model is defined, the experimental data is fitted to the well-known physical dispersion formulas and the best match between the two sets are obtained.

SE is particularly sensitive to changes in material properties like crystallinity and surface roughness. For a-Si:H, the dielectric function reflects the main absorption in the film due to band to band transitions, while the evolution of the surface roughness yields information about nucleation process and surface mechanisms [70].

For the structural variation analysis with spectroscopic ellipsometry, it is necessary to work on the imaginary part of the dielectric constant of the materials. Graph of dielectric constant versus photon energy gives the structural information about the sample like that if the graph of the sample gives two sharp peaks at 3.5 eV , which corresponds to the direct optical transitions from the Γ (valance band) to Λ (conduction band) in the first Brillouin zone and 4.2 eV, originating from a large range of transition in the Brillouin zone along the X and R directions [71-72]. A broad peak around 3.6 eV indicates amorphous structure. Narrower peak with a shoulder at smaller photon energies indicates that the sample contains mixture of crystallinity and amorphous phase like nanocrystalline or microcrystalline structure (Figure 3.7) [36, 57, 72]. In particular, while μc sample has an intermediate spectrum with a soft peak at 4.2 eV and a shoulder at low photon energies [36], nc sample has a soft peak at 3.6 eV and a shoulder at low photon energies.

For the surface rougness measurements, top layer of the model is defined as the composite structure including void and the bulk by using Bruggeman Effective Medium Approximation (EMA) method in which each component material is identified by its percentage of overall volume of the relevant layer [36,73].
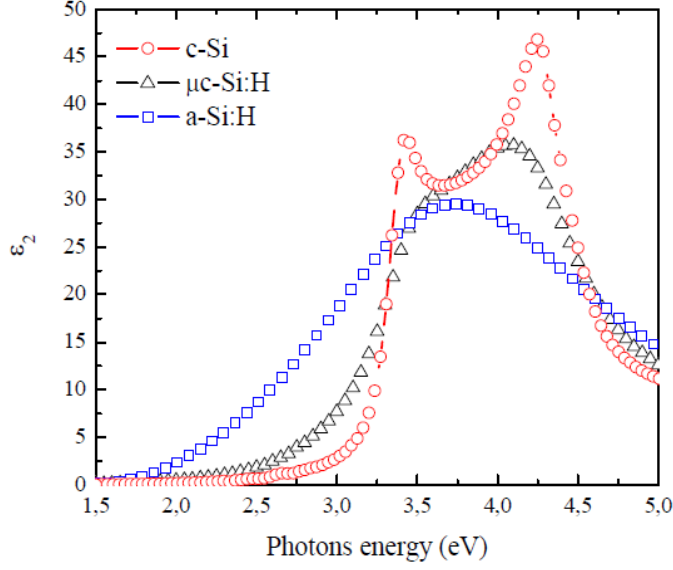
Figure 3.7 Photon energy versus ε_2 graph [36].

Effective medium approximation method based on the addition of the polarization effects and a general expression of it is given as:

$$\frac{\varepsilon_{eff} - \varepsilon_h}{\varepsilon_{eff} + 2\varepsilon_h} = \sum_i f_i \frac{\varepsilon_i - \varepsilon_h}{\varepsilon_i + 2\varepsilon_h} \tag{3.3}$$

where ε_{eff}, ε_h, ε_i and f_i are the effective medium dielectric function, the host dielectric function, and the dielectric function and volume fraction of the ith component, respectively. For the Bruggeman approximation (EMA) $\varepsilon_{eff} = \varepsilon_h$ and Eqn. 3.3 becomes [73-75]:

$$\sum_i f_i \frac{\varepsilon_i - \varepsilon_h}{\varepsilon_i + 2\varepsilon_h} = 0 \tag{3.4}$$

For the a-Si:H thin films, generally Tauc-Lorentz dispersion law is used to describes the material [7, 76]. According to this approach, imaginary part of the dielectric function is defined as:

$$\varepsilon_2(E) = \begin{cases} \dfrac{AE_oC(E-E_g)^2}{E\left[(E^2 - E_o^2)^2 + C^2E^2\right]} & \text{if } E > E_g \\ 0 & \text{if } E \le E_g \end{cases} \tag{3.5}$$

where, E_g is optical band gap energy, E_o is energy of maximum absorption (peak transition energy), A is the amplitude factor proportional to the density of the material , and proportional to the height of ε_2. C is the broadening parameter that is inversly proportional to the short range order of the material [34, 77-80]

40

3.4.2 Fourier-Transform Infrared Spectroscopy (FTIR) Measurements

FTIR is a powerful tool for identifying types of chemical bonds in a molecule by producing an infrared absorption spectrum [81]. Molecular bonds vibrate at well defined, specific frequencies depending on the elements and the type of bonds. For most common materials, the spectrum of an unknown material can be identified by comparison to a library of known compounds.

Since a-Si:H contains different hydrogen bonding configurations, each configuration has its absorption peaks. Possible peaks are summarized in Table 3.2 below for the a-Si:H.

Table 3.2 Silicon-hydrogen stretching modes for FTIR measurements

Surface Hydrogen			Bulk Hydrogen		
Peak position (cm^{-1})	Hydride Type	References	Peak position (cm^{-1})	Hydride Type	References
2070-2080	SiH	[70,82,83]	1980-2010 (LSM)	SiH in vacancies	[7, 84 85,82]
2095-2105	SiH	[70,82,83]	2070-2100 (HSM)	SiH clustered	[85,86]
2110-2120	SiH_2	[70,82,83]	2190-2210	$SiH_x(O_y)$	[82]
2135-2145	SiH_3	[70,82,83]	2240-2260	$SiH(O_3)$	[82,84]
2255-2265	$SiH(O_2)$	[70]			

The measurements are performed with a Platinum model of Bruker Optics Fourier Transform Infrared Spectrometer with an Attenuated Total Reflection apparatus (FTIR-ATR). The IR spectra are measured from $\omega=400$ cm^{-1} up to $\omega=4000$ cm^{-1} with resolution of 4 cm^{-1}. In order to obtain quantitive information about the hydrogen bonding structure, measured IR spectrum are deconvoluted several gaussian peaks. In Figure 3.8 all possible streching modes are indicated on μc-Si:H/c-Si structure [87].
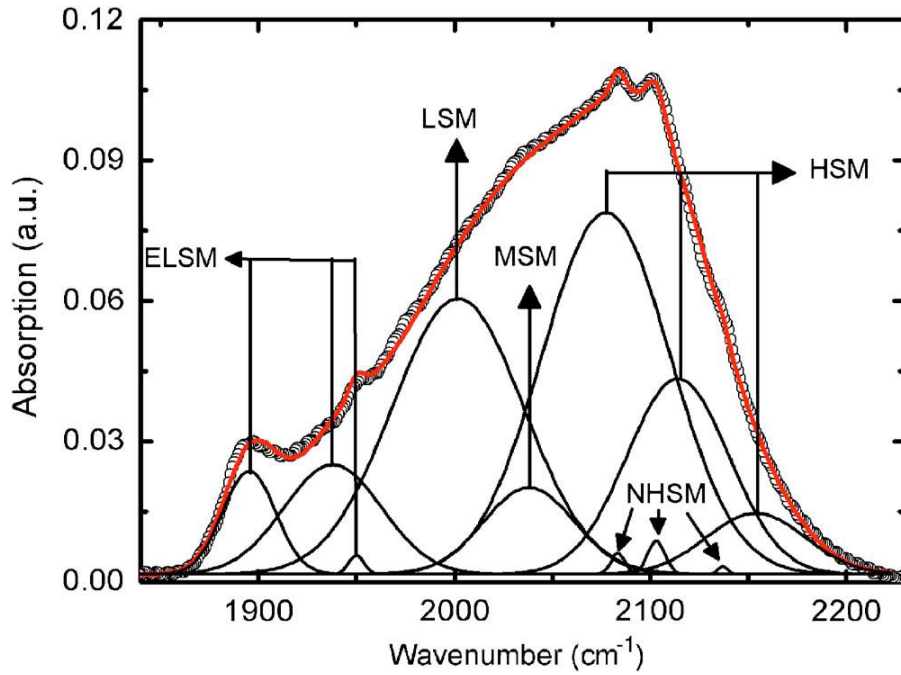
Figure 3.8 Deconvolution gaussian peaks for μc-Si:H films IR spectrum [87].

The low (LSM) and high (HSM) streching modes are originated from the bulk *a*-Si:H and associated bands lies at 1980–2010 cm^{-1} and 2070–2100 cm^{-1}, respectively [70,83,87]. The HSM ranges in μc-Si:H, broadens by two additional modes ~ 2120 and 2150 cm^{-1}, due to the contribution of Si-H$_2$ and Si-H$_3$ bonds in the bulk. Additionally, three narrow high streching modes (NHSM) (2083, 2103, and 2137 cm^{-1}) are observed, reflecting Si-H, Si-H$_2$, and Si-H$_3$ bonds on crystalline surfaces, assigned to crystalline grain boundaries in the bulk. The assignment of the extreme low strechinh modes (ELSM) (~1895, ~1929, and ~1950 cm^{-1}) are believed to be resulting from extreme high local hydride densities combined with mutual hydride dipole-dipole interactions, which either passivates the crystalline grain boundaries or fills the small pores [83].

It is known that the wavenumber at 2000 cm^{-1} means the stretching mode of the Si-H bond and the wavenumber at 2090 cm^{-1} peak is the stretching mode of the Si-H$_2$ bond, respectively. The Si-H$_2$ stretching mode is the indication of defects in the film and appearance of it can be concluded as the increase of a dangling bond in the film due to the microcrystallization of the film. The intensity of the Si-H stretching mode on the other hand, indicates that good quality a-Si:H thin films [49].

3.4.3 Conductivity Measurements

3.4.3.1 Dark Conductivity Mechanisms in Intrinsic Amorphous Silicon

In doped or intrinsic a-Si:H the dark conductivity σ$_{dark}$ is given by:

$$\sigma_{dark} = \sigma_o x \exp\left(-\frac{E_A}{k_B T}\right) \qquad (3.6)$$

The dark conductivity σ_d is determined by the mobility and the density of electrons in the conduction band [88]. Different conduction mechanism dominate the dark conductivity at different temperatures.

In the dark, at 0 Kelvin, the conductivity of the sample is zero. At very low temperatures, conductivity will occur in localized states near the Fermi level and in this case it is determined by variable-range hopping and nearest neighbour hopping mechanisms, in which electrons move from one localized states to another.

In the intermediate temperatures (including room temperature), Fermi level shifts slightly since gap states at higher energies are also occupied. In this case, hopping will occur in the whole width of the band gap, especially in the tail states.

At high temperatures, the tail of the distribution function enters the conduction band. In this case, electrons are present in the extended states of the conduction band, leaving empty places in the valance band. These are high mobility electrons significantly contributing to the conductivity. In the extended state conductivity there are various recombination and trapping mechanisms controlling the conductivity in amorphous silicon:

An electron can be either temporarily trapped in a localized state close to the conduction band edge, after which a thermal release follows, or final recombination to the valance band may occur. In the case of trapping in the shallow traps the electron contributes again to the conductivity after thermal release, as a result of the absorption of a phonon. Each electron may be trapped and reemitted in this way many times before final recombination, which is called multiple trapping mechanism.

3.4.3.2 Photoconductivity

The photoconductivity, represents the excess charge carrier concentration generated under illumination. The photoresponse of the material is defined as the ratio between the light and the dark conductivities [89].

A high photo-to-dark conductivity ratio (σ_{ph}/σ_d) and a low dark conductivity at room temperature are essential properties of device quality photovoltaic material since a low σ_d leads to a stronger field and a low diode current in the solar cell and a high σ_{ph}/σ_d indicates a low recombination rate of charge carriers through mid-gap states [88]. Device-quality intrinsic a-Si:H has typically a photoresponse of 10^5-10^7 under standard illumination conditions.

The two important parameters determining the conductivity are number of electrons (n) and drift mobility (μ). The number of electrons in the conduction band is determined by the density of localized states, which is affected by the concentration and nature of impurities and lattice disorder. Also the ratio of the lifetimes in the extended states and in the localized states influences the number of electrons. The value of the mobility is strongly dependent on the structure of the material.

In high quality amorphous silicon the dark conductivity at ambient temperature is low. If the density of localized gap states is increased by incorporation of impurities, since the dark conductivity is directly proportional with n, it is also increases. On the other hand, since the dark conductivity is not only determined by the number of free electrons, but also their mobility, the magnitude of dark conductivity alone is not a good measure for the material quality. It is necessary to determine the photo-conductivity as well. Illumination changes the number of free electrons, while the mobility stays relatively constant. In conclusion, it can be said that a low value of the density of states can be concluded from a low dark conductivity, while a high value of the mobility results in a high photo-conductivity.

For the measurement of the dark and photo conductivity of the samples, aluminum contacts with known seperation and length were evaporated onto the films deposited on the glass substrate. Two parallel wire contacts were prepared with silver paste on the deposited film. An electrical potential V is applied to the electrodes and the current passing through them, I, is measured. Then the conductivity can be determined from the Equation 3.7 [90]:

$$\sigma = \frac{I}{V}\frac{L}{Wt} \qquad\qquad (3.7)$$

where, t is the film thickness, W is the width of the electrodes and L is the seperation between the electrodes. The photoconductivity σ_{ph} was determined as excess conductivity under AM 1.5G light and the dark conductivity σ_d was determined by covering the sample with a black cover material. The photosensitivity is calculated from

$$\sigma_{ph}/\sigma_d \; . \qquad\qquad (3.8)$$

3.5 Solar Cell Characterizations

For the device characterization, we have used both the current-voltage measurements and the electroluminescense measurements, the detail of which are given below.

3.5.1 Current-Voltage measurements

Figure 3.9 shows a picture of a I-V measurement system. Solar cell is illuminated by the solar simulator and the current between the probes is recorded for each applied voltage. During the measurement, the solar cell is cooled with water circulation of the vacuum chuck. Wafer was put onto the chuck 10 minutes before the measurement in order to get the temperature stability. For preventing the heating of the wafers, shutter of the solar simulator lamp is opened just before the I-V measurements.
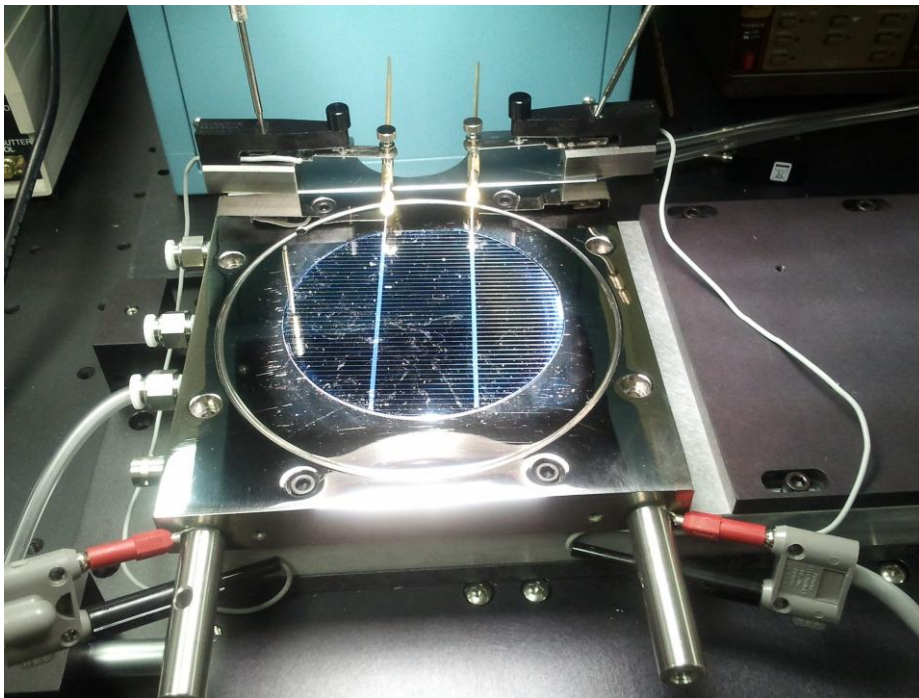
Figure 3.9 Picture of the J-V measurement system

From the I–V measurement, we can determine the solar cell performance by measuring open circuit voltage (V_{oc}), short circuit current density (J_{sc}), fill factor (FF) and efficiency (η). Figure 3.10 shows a typical J-V curve.

The open circuit voltage is the voltage that the solar cell delivers without connected to load. It brings information about the material quality and the surface passivation quality. The doping of the substrate and the emitter also play an important role for V_{oc}. The short circuit current density J_{sc} is the current that is extracted from the device. The fill factor is defined as the ratio of maximum power density P_{max} to the product of $V_{oc}xJ_{sc}$.

$$FF = \frac{P_{max}}{V_{oc} \times I_{sc}} \tag{3.9}$$

Efficiency of the solar cell η is defined as the ratio of P_{max} to the incident power density P_{light}.

$$\eta = \frac{P_{max}}{P_{light}} = \frac{FF \times V_{oc} \times I_{sc}}{P_{light}} \tag{3.10}$$
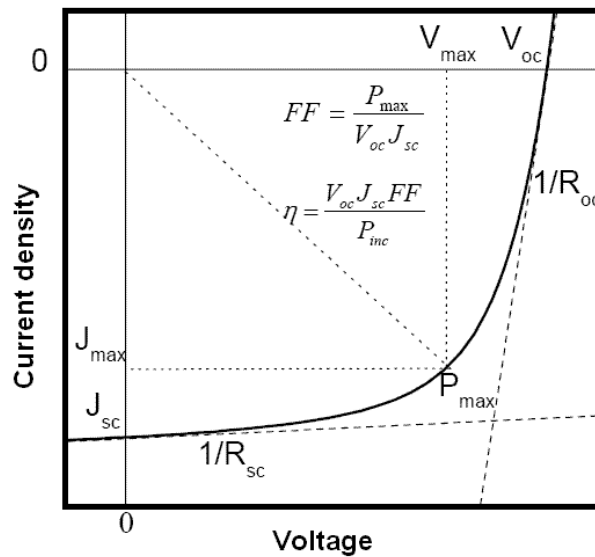
Figure 3.10 Typical J-V curve and the characterization parameters [91].

3.5.1.1 Uncertainty Calculations

Uncertainty evaluation of the measuremet is estimated by taking into account all contributing factors affecting the measurement. The considering uncertainty components and values for voltage and current measurements are given in Table 3.3 and Table 3.4 below.

Repeatability of the measurement component value is obtained from the standard deviation results of successive measurements. Accuracy of the device contribution value is obtained from the Keithley

2420C SourceMeter specifications. Temperature dependence uncertainty contribution is calculated by measuring the voltage and current values of the sample at different temperature set values and by obtaining the variation in their value with respect to the variation in temperature.

Uncertainty values for the FF and efficiency are calculated by considering the uncertainty values of current, voltage and the light source.

Table 3.3 Uncertainty Budget for Voltage Measurements

Symbol	Uncertainty Components	Standard Uncertainty (mV)
$U_{\delta repeatability}$	Repeatability of the measurement	3.95
$U_{\delta accuracy}$	Accuracy of the device	0.11
$U_{\delta temperature}$	Temperature dependency	1.80
Combined Uncertainty		4.08
Expanded Uncertainty		8.17

Table 3.4 Uncertainty Budget for Current Measurements

Symbol	Uncertainty Components	Standard Uncertainty (mA)
$U_{\delta repeatability}$	Repeatability of the measurement	40.41
$U_{\delta accuracy}$	Accuracy of the device	3.76
$U_{\delta temperature}$	Temperature dependency	0.50
Combined Uncertainty		40.47
Expanded Uncertainty		80.95

3.5.2 Electroluminescence (EL) Measurements

Electroluminescence is a contactless photographic surveying method for the analysis of silicon solar cells and photovoltaic modules [92,93], especially in the determination of the local effective diffusion length, the carrier collection length L_c, the local junction voltage and the series resistance. The widest use of electroluminescence is the defects detection in solar cells, mainly cracks, broken fingers, dark dots and inactive part of cells [94, 95].

In the EL measurement, the device is forward biased and a CCD is used to detect radiative recombination [96]. With the help of the forward bias potential, additional carriers are injected into the junction and they move in the material until they recombine. During their radiative recombination, the carriers emit electromagnetic radiation energy, electroluminescence, in a range of 1000 to 1200 nm. Intensity of this radiation gives information on the material properties, like the surface recombination velocity, minority carrier lifetime and diffusion length. Additionally extrinsic defects that have occurred in the cell or module manufacturing process can also be detected [93]. From the EL intensity signal, areas that have been discoloured correspond to regions of lower EL signal intensity,

which means that the material in these regions is damaged or that the discolouration of the coating blocks the EL signal from being detected. Either way this degradation results in poor photo-response and, ultimately, performance degradation in the affected areas.

During the Electroluminescence intensity measurements, emitted photons are captured by using a sensitive CCD camera in order to get an image of the distribution of radiative recombination in the cell. This distribution is determined by the local excitation level, which allows the determination of electrical losses and can be used to map the diffusion length of minority carriers [97]. The experimental setup for electroluminescence measurements is given in Figure 3.11. The cell is placed underneath the camera and electrically contacted from both sides.
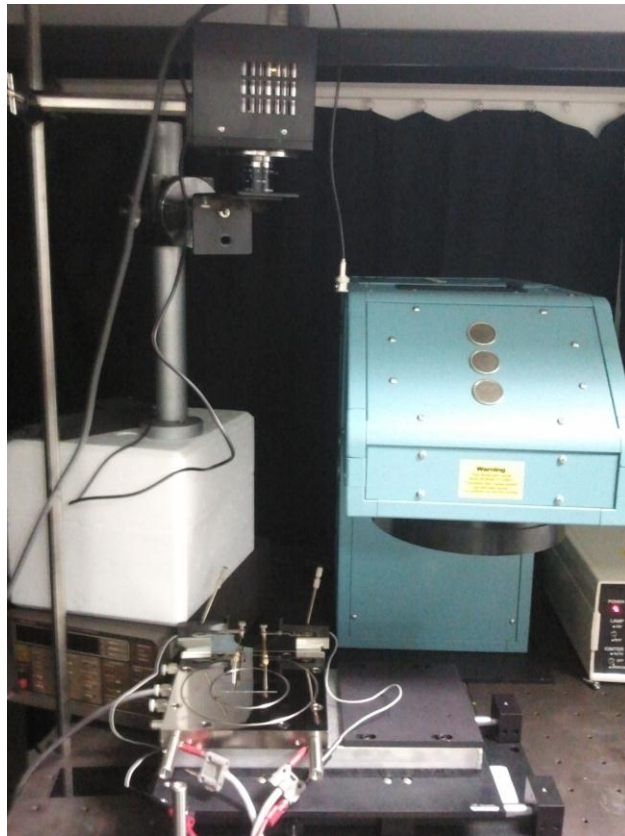
Figure 3.11 Typical electroluminescence setup [97].

CHAPTER 4

RESULTS and DISCUSSIONS

In this part of the thesis, we have concentrated on the experimental analysis, results and discussions. The performance of c-Si/a-Si:H HJ solar cells, fabricated by the process discussed in the Chapter 2 is analyzed in this chapter. The main aim of this work is to optimize the performance of these solar cells with regards to the parameters like efficiency, V_{oc}, J_{sc} and fill factor. Additionally, the structural analysis of intrinsic layer is studied and discussed extensively.

4.1 Determination of the Deposition Parameters for Device Quality Intrinsic a-Si:H Films for PV Applications

The optimal values for the device quality thin film solar cell are considered as: (i) Low dark conductivity, σ_d ($<10^{-10}$ $\Omega^{-1}cm^{-1}$) , which is an indication of the absence of electronically active impurities [36]; (ii) high photo to dark conductivity ratio ($\sigma_{ph}/\sigma_d \geq 10^5$) at room temperature, indicating a low recombination rate of the photogenerated carriers through the mid-gap states and (iii) high absorption coefficient with Tauc gap, E_g is in the range of 1.6 eV to 1.8 eV.

Since there is no unique PECVD reactor design, deposition parameters for device quality a-Si:H films need to be determined in each laboratory. This makes it difficult to compare properties of a film deposited in a laboratory with the others.

Physical properties of the deposited films were analysed using photoconductivity, (σ_{ph}), dark conductivity (σ_d), Spectroscopic Ellipsometry (SE), Scanning Electron Microscope (SEM) and Atomic Force Microscopy (AFM) measurements for different deposition parameters based on the literature given section 2.3.1 "Relation between Plasma Parameters and Material Properties". The substrate temperature, plasma power, gas flow rate and the gas pressure were optimized to meet the device quality a-Si:H requirements to be applicable for solar cells.

Intrinsic amorphous silicon thin films were deposited on Corning 7059 glass substrates for 30 minutes. Substrate temperature of the samples was changed from 100 ^{o}C to 300 ^{o}C, deposition pressure was changed from 0.4 Torr to 0.8 Torr, plasma power was changed from 3 Watt to 12 Watt and gas flow rate was changed from 3 sccm to 40 sccm.

4.1.1 Conductivity Measurements

Photoconductivity of the deposited films were measured under 1000 W/m^2 AM 1.5G illumination, at 25 ^{o}C under standart test conditions (STC). For conductivity measurements, coplanar Aluminum electrodes were deposited by thermal evaporation method within 5 mm×1.4 mm dimensions. Constant voltage was applied to the electrodes using Keithley 6517 Electrometer and resulting current was measured by the same device.

Photo to dark conductivity of intrinsic hydrogenated amorphous silicon films as a function of substrate temperature, deposition pressure, RF power and gas flow rate is presented in Figures 4.1-4.4, respectively. Observed extreme values in the figures were double checked for ensuring the film properties. In this way a-Si:H thin films with photo to dark conductivity ratio better than 10^5 is achieved at 225 ^{o}C (Figure 4.1), 0.6 Torr (Figure 4.2), 3 Watt (Figure 4.3) and 40 sccm (Figure 4.4). Observed changes of photo to dark conductivity is understandable based on the literature presented in section 2.3.1.
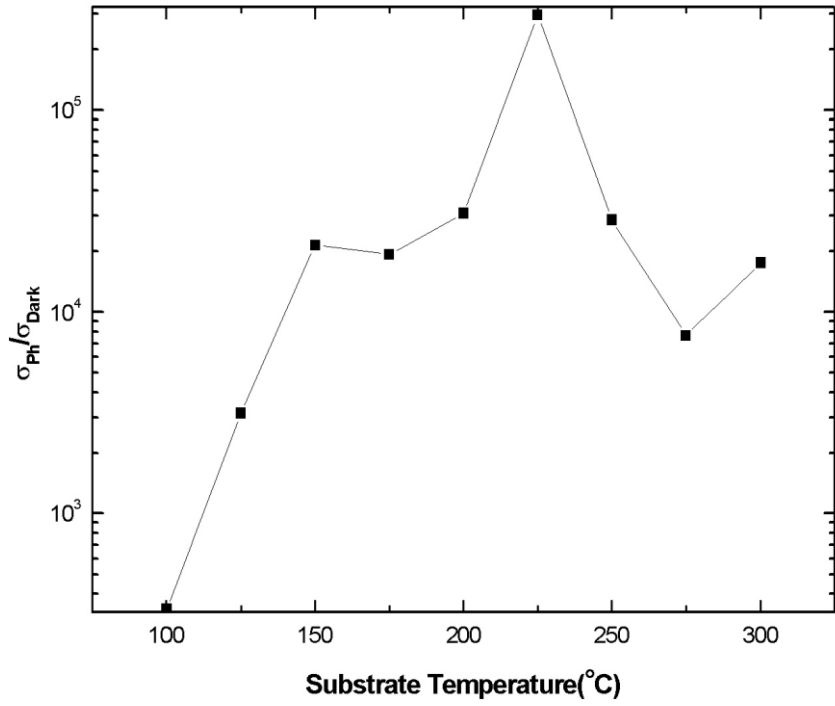
Figure 4.1 Variation of photo to dark conductivity ratio with substrate temperature.
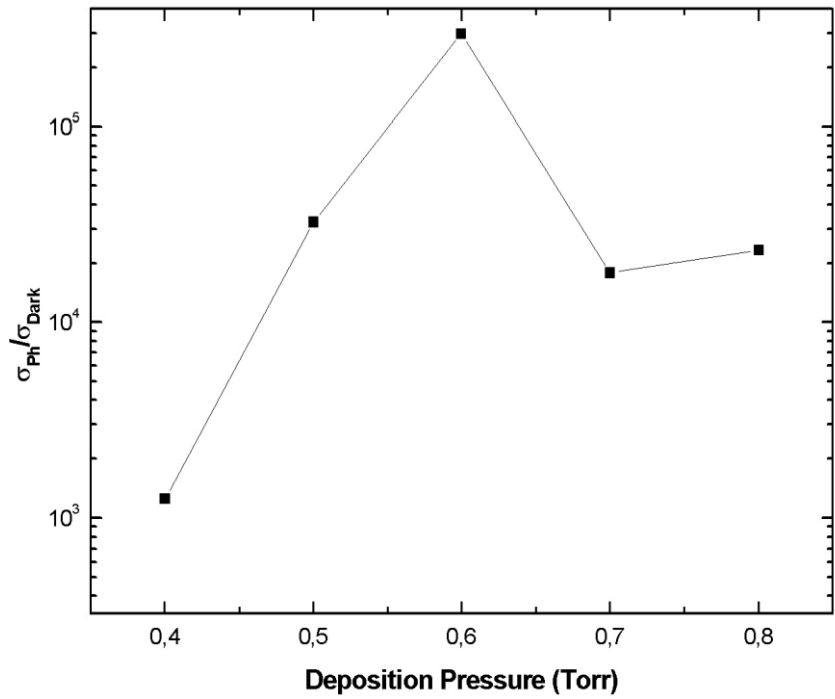
Figure 4.2 Variation of photo to dark conductivity ratio with deposition pressure.
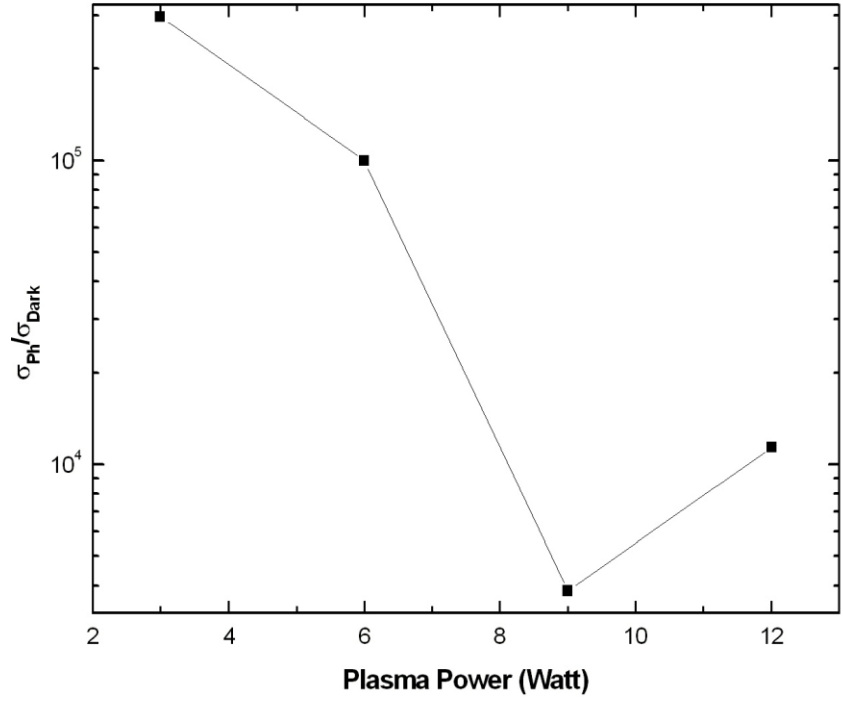
Figure 4.3 Variation of photo to dark conductivity ratio with plasma power.
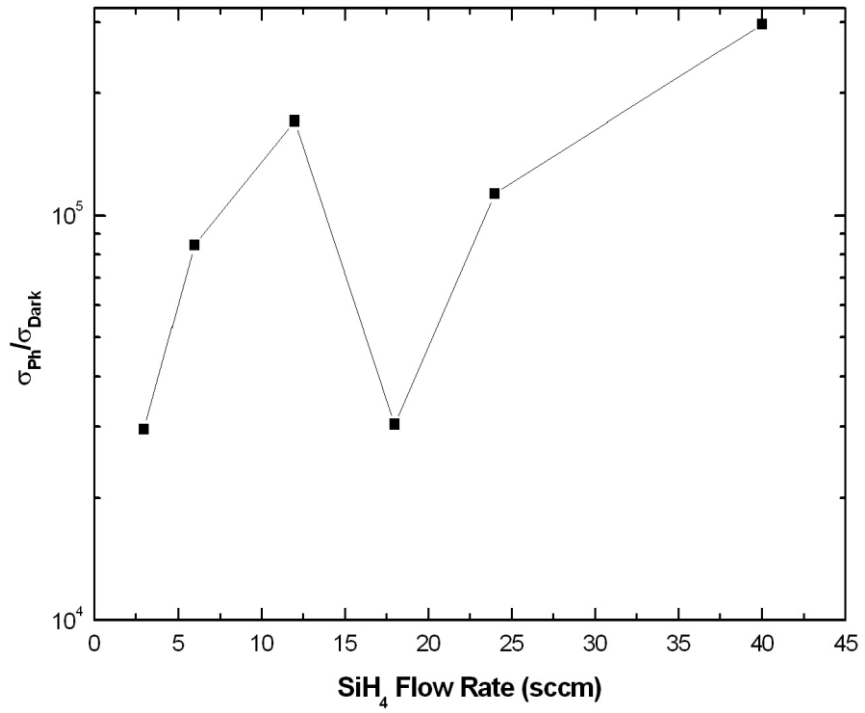
Figure 4.4 Variation of photo to dark conductivity ratio with gas flow rate.

4.1.2 Spectroscopic Ellipsometer Measurements

S.Y.Lee et al. [98] proposed that intrinsic layers with higher dielectric function value would lead to higher conversion efficiency, especially with higher FF. According to this proposal, we have tried to optimize intrinsic layer of samples with spectral ellipsometer measurements and we ploted the dielectric function constant of the intrinsic amorphous thin films at different substrate temperature values.

According to Figure 4.5 the amplitude of the broad ε_2 peak at 3.5 eV decrease as T_s reduces. Although the film deposited at 225 ^{o}C does not have the highest absorption spectra, there is a shift of ε_2 to higher energies at 225 ^{o}C, which is related to higher hydrogen content [71,78]. In addition, this film has also shown high photo/dark conductivity ratio. So that, we selected 225 ^{o}C as our deposition temperature for intrinsic a-Si:H films without H_2 dilution.
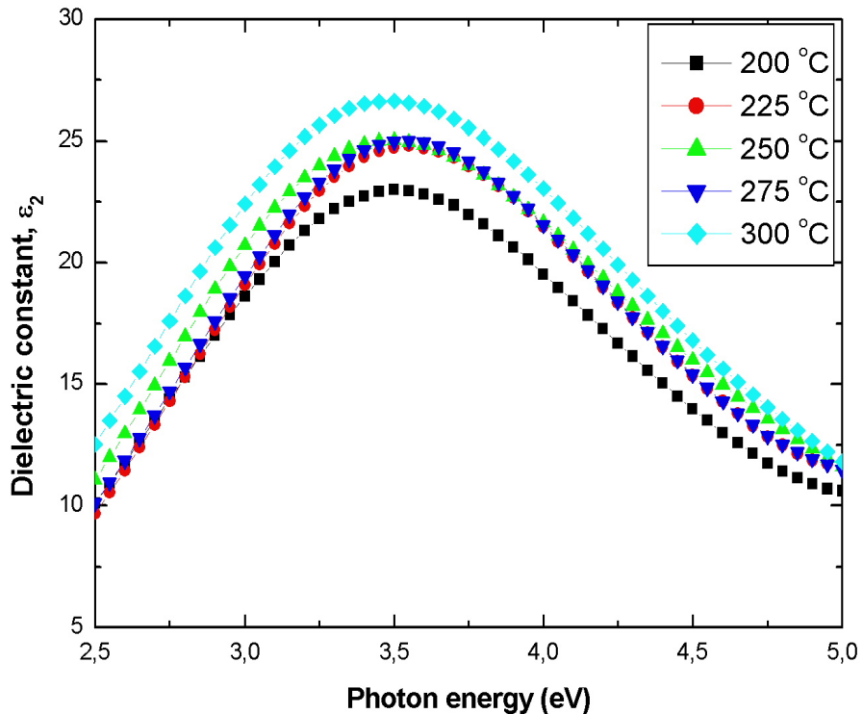
Figure 4.5 Dielectric function spectra for the a-Si:H films deposited on glass substrate at different substrate temperatures.

For the bandgap estimation of amorphous thin films we have used Cody gap, which is expressed as follows:

$$\varepsilon_2 = A(E_n - E_g)^2 \tag{4.1}$$

Thus, the Cody gap is determined from the energy position of $(\varepsilon_2)^{1/2} = 0$ in the plot of $(\varepsilon_2)^{1/2}$ versus E_n, given in Figure 4.6 [42].
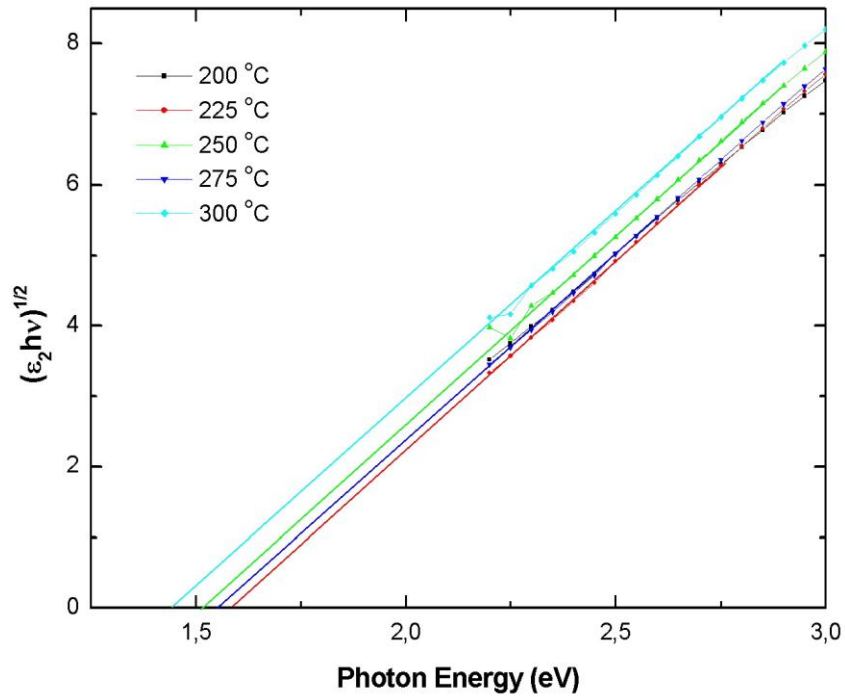
Figure 4.6 Analysis of optical bandgap (Cody gap) using the ε_2 spectra.

From the results of the ellipsometer analyses, for the films 30 min deposited on glass substrates at different substrate temperatures, the obtained thickness values of the samples, the corresponding deposition rates and calculated Cody bandgap values are given in Table 4.1:

Table 4.1 Parameters from spectroscopic ellipsometer analyses

$T_{substrate}$ (^{o}C)	Thickness (nm)	Deposition rate (Å /sec)	Cody gap (eV)
200	1515.7	2.1	1.56
225	999.1	2.4	1.59
250	938.0	2.6	1.52
275	988.6	2.7	1.56
300	1017.4	2.8	1.44

It is found that intrinsic a-Si:H films has the maximum effective band gap value at 225 ^{o}C substrate temperature. Above this value, especially at 300 ^{o}C, the optical band gap of intrinsic a-Si:H value decreases, which is probably created by the overflow of hydrogen in higher temperatures. As it is already stated before, the application of higher substrate temperatures results in the loss of hydrogen from the surface, resulting formation of large dangling bond densities.

Additionally, in order to have high-efficiency solar cells we need to reduce the optical absorption loss of the a-Si by using wide-gap a-Si, which will result relatively high I_{sc}. Thus, it seems suitable to choose the 225 ^{o}C as a substrate temperature.

4.1.3 SEM and AFM Measurements

As a final study, in order to ensure that the glass substrate is completely and uniformly covered with deposited films, SEM measurement are performed for the 30 minute deposited a-Si:H thin films on glass substrates and it is observed that the surface of the film is completely and uniformly coated with a-Si:H (Figure 4.7). The corresponding surface roughness of the film was measured as 4 nm along the 5 μm × 5 μm film area as in Figure 4.8.
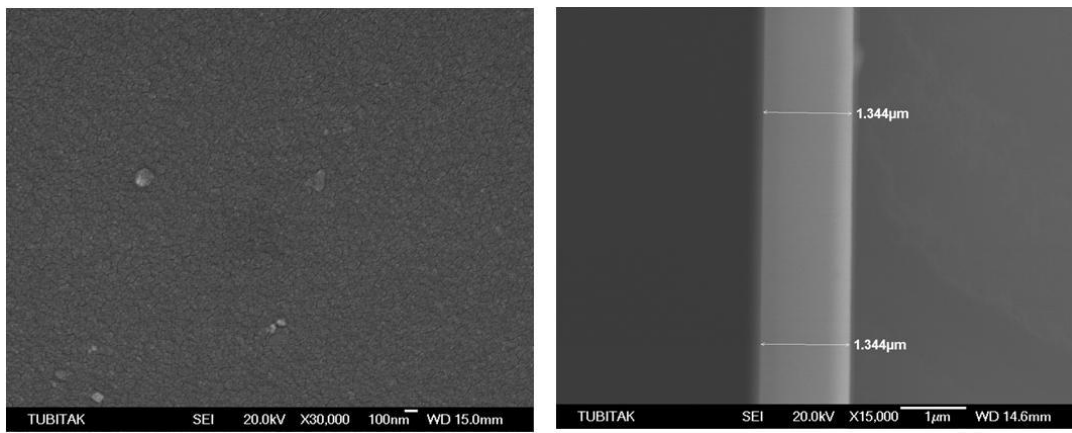
Figure 4.7 SEM surface and cross-section images of a T_{subs}: 225 ^{o}C sample.
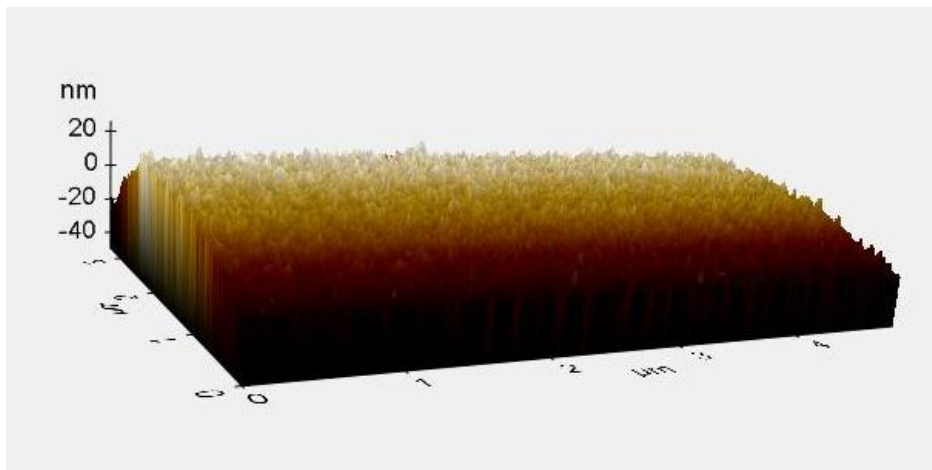
Figure 4.8 AFM surface measurement result for T_{subs}: 225 ^{o}C sample.

As a result of conductivity and SE measurements, it is concluded that the necessary deposition paramaters for device quality a-Si:H layer production with the present PECVD system are that: 225 ^{o}C substrate temperature, 0.6 Torr gas pressure, 3 Watt RF plasma power and 40 sccm gas flow rate.

4.2 c-Si Wafer Cleaning: Wet and Dry Etching Optimization Studies

For the wafer substrate surface cleaning, we have used three different cleaning procedures two of which are wet cleaning processes and the last one is dry cleaning method.

In the first wet cleaning method we used the following procedure:

- Immersing into acetone for 10 min
- Rinsing with DI water for 1 min
- Immersing into IPA for 10 min
- Rinsing with DI water for 1min
- Immersing into %5 HF for 10 sec
- Rinsing with DI water for 1min

Later on, in the second wet cleaning method we used the following cleaning procedure for flat Si (100) wafer surfaces:

- Standard RCA cleaning
- Rinsing with DI water for 1min
- Immersing into H_2SO_4:H_2O_2 (1:1) 10 min (wet chemical oxidation, for smooting)
- Rinsing with DI water for 1min
- Immersing into %1 HF 60 s (for oxide removal)
- Rinsing with DI water for 1min

In the case of dry cleaning method, we have used NF_3 plasma for the cleaning of the wafer surface. In order to determine the NF_3 plasma parameters, films of 1μm thickness were deposited on to glass substrates, and the decrease in the film thickness due to the NF_3/Ar plasma was investigated with profilometer measurements. Since the NF_3 plasma is non-stable, it has been diluted with Ar gas by 15:1. a-Si:H etching rate variation with respect to NF_3 flow rate and total gas pressure are given in Figure 4.9 and Figure 4.10. As a result of the studies, optimum plasma etching parameters were decided as: 0.5mbar for gas pressure, 40W for RF power, 14 sccm for gas flow rate. These parameter set values were used both for the cleaning of the chamber and the c-Si wafer. In this way, 1μm a-Si:H thin films deposited on the glass substrate can be completely etched in 15 minutes (Figure 4.11).
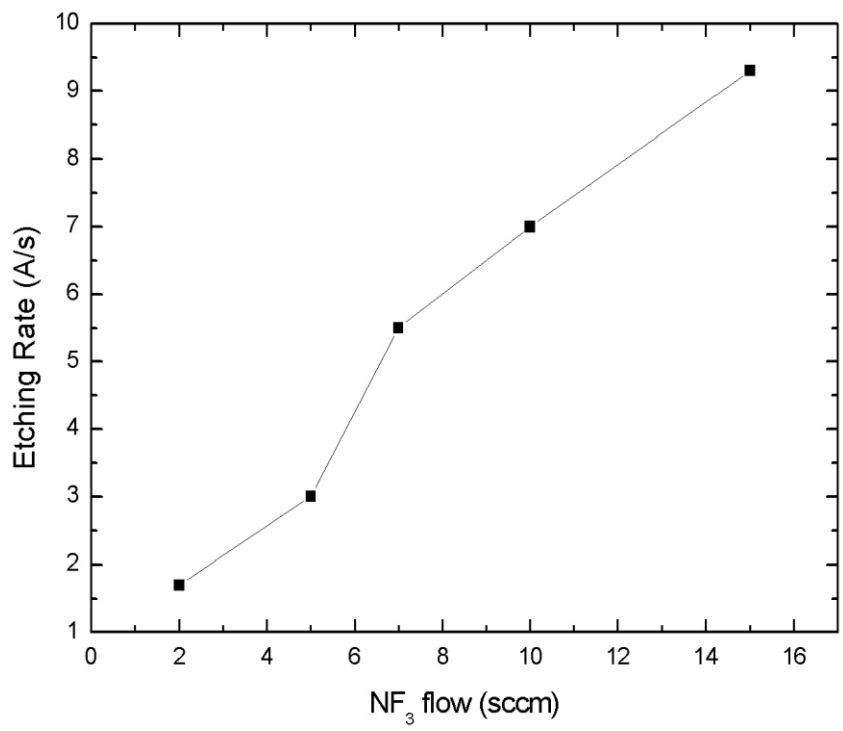
Figure 4.9 a-Si:H etching rate variation with respect to NF$_3$ flow rate.
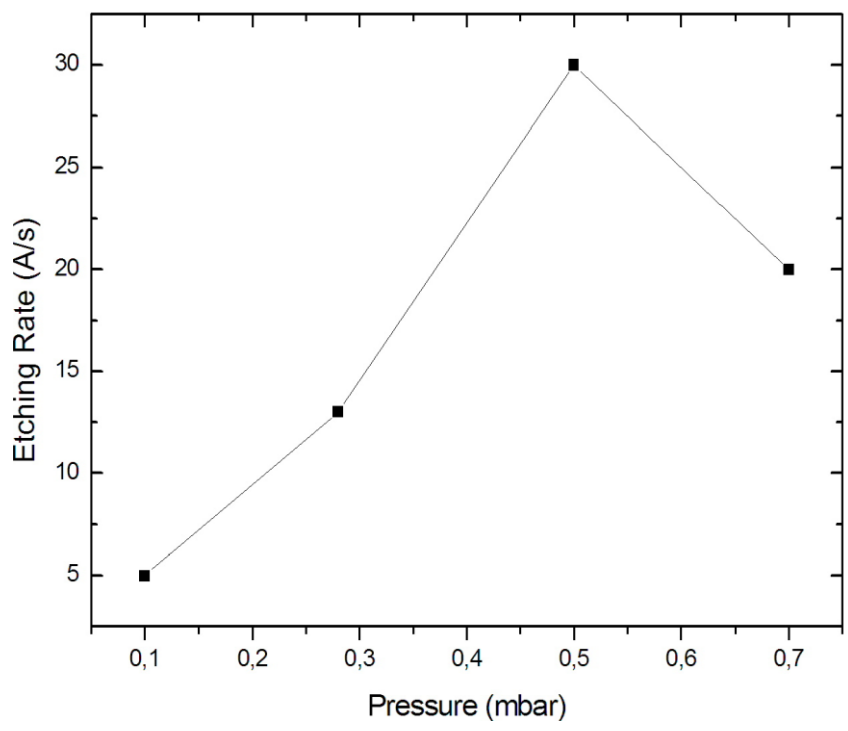
Figure 4.10 a-Si:H etching rate variation with respect to gas pressure.
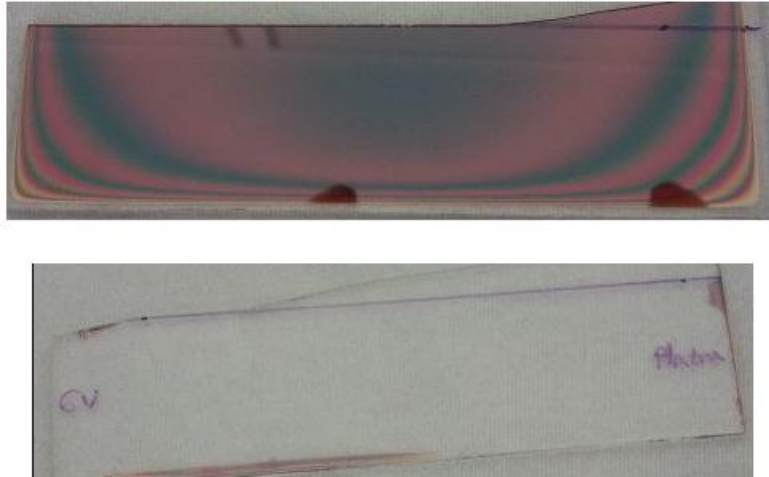
Figure 4.11 Glass substrate before and after NF$_3$ etcing in PECVD.

In order to compare the three cleaning procedures, we have cleaned <100> , p type, 1-20Ωcm^{-1} c-Si wafers with each procedures and we have produce a-Si:H(n)/a-Si:H(i)/c-Si(p) SHJ solar cell structure with deposition parameters determined in section 4.1.

Current-Voltage results of these measurements are given in Figure 4.12 below. In Figure, WE1 denotes the "wet chemical cleaning -I", WE2 denotes the "wet chemical cleaning -II" and DE denotes the "dry etching cleaning". As it can be seen from Figure 4.12 the short circuit current of wet etching cleaning for method II is highly improved whereas there is only small improvement observed for open circuit voltage values.
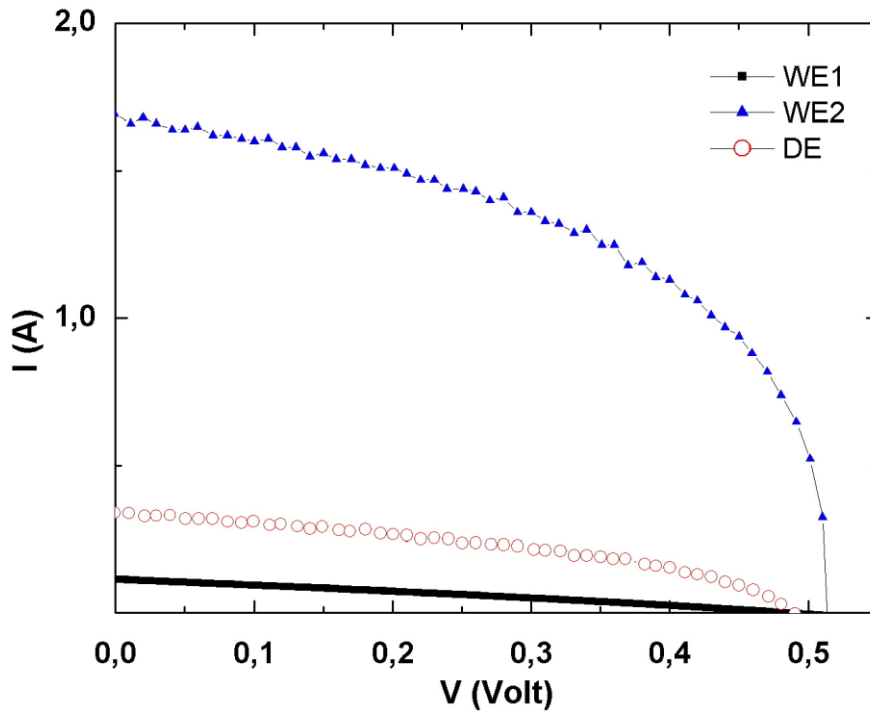
Figure 4.12 Comparision of wafer cleaning procedures

4.3 Determination of Doping Concentration Ratio:

To determine doping concentration ratio, a-Si:H (n)/a-Si:H (i)/c-Si (p) solar cells were deposited on the top of 100mm, <1 Ω.cm, 500 μm thick, p-type commercial Czochralski (100) c-Si wafer substrates with different doping concentration ratios. Prior to the deposition of the a-Si:H layers, wafers were treated by a wet chemical II cleaning explained in Section 4.2.

The deposition parameters used were for i layer are 12 mW/cm^2 RF power density; 225 °C substrate temperature; 0.6 Torr pressure; 40 sccm SiH$_4$ flow and 60s deposition time. For the n-doped layer [PH$_3$]/[SiH$_4$] ratio has been changed in the range of 500 to 500000 ppm for 120 s. The solar cell area was 72 cm^2.

During the characterization, we have used open-circuit voltage data for the determination of the gas phase doping concentration since it is stated that the open-circuit voltage follows the same trend with the efficiency of the solar cell [10,99].

Result of [PH$_3$]/[SiH$_4$] flow ratio versus V$_{oc}$ curve is given in Figure 4.13. In our studies we have obtained a broad plato for the high V$_{oc}$ values with respect to gas phase doping concentrations in between [PH$_3$]/[SiH$_4$]=5000 ppm to [PH$_3$]/[SiH$_4$]=50000 ppm values. Measurements have been checked number of times. This result was interesting for us in that there is just one efficiency peak value for the doping concentration ratio graphs in literature studies [10,99]. In their results, the efficiency decreases for higher and lower gas phase doping concentrations. Actually, considering literature, they have changed doping ratio up to 10000 ppm and they have not continued their studies for the larger doping concentration ratios. Despite, some groups prefers to use n$^+$ doping in SHJ cells to avoid junction to be formed between n-type ZnO:Al and c-Si (p) [103].

During solar cell studies in order to prevent the impurity concentration in the structure, we have decided to use [PH$_3$]/[SiH$_4$]=5000 ppm doping concentration rate for the n layer deposition. In the Figure 4.14 you can see the current-voltage curve of solar cell in a-Si:H(n)/ a-Si:H(i)/c-Si(p) structure for the n layer doping concentration rate 5000 ppm.
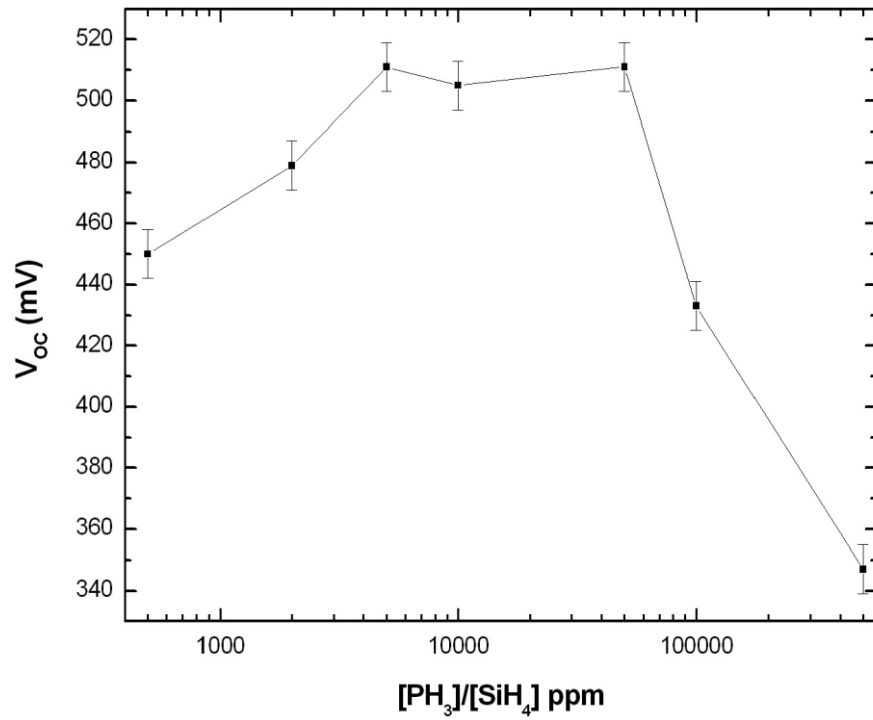
Figure 4.13 Open-circuit voltage variation as a function of the gas phase doping concentration
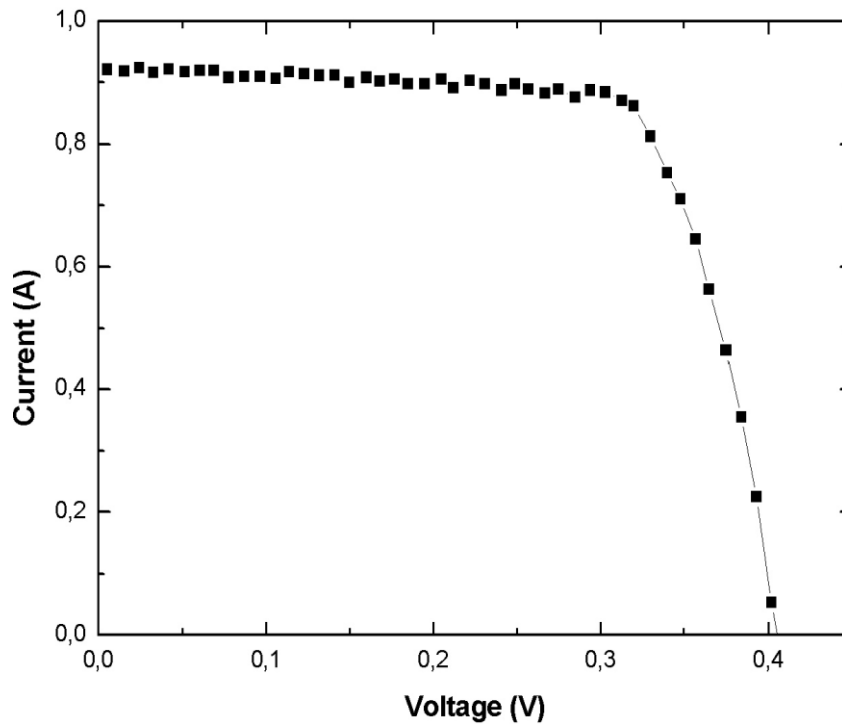
Figure 4.14 I-V curve of the solar cell at the doping concentration ratio of 5000 ppm with 72 cm^2 area and 4.7% efficiency with V_{oc}:0.406 V, I_{sc}:0.922 A , FF:89.46%.

4.4 Investigation of the Growth Mechanisms of (i) a-Si:H Thin Films on c-Si Wafers at Substrate Temperature of 225 ^{o}C

Figure 4.15 shows the general HRTEM result of SHJ structure consist of 5 minutes deposited i-layer, 5 minute deposited n-layer and 15 minute deposited ZnO:Al, where the last one is deposited by RF sputtering. Thickness of the deposited layers indicated in figure.

Figure 4.16 shows the c-Si/intrinsic a-Si:H interface at closer view. We observe that there is an epitaxial growth at the beginning of the intrinsic a-Si:H layer deposition followed by pyramidal shaped crystals and then a-Si:H structure. Existence of epitaxial growth and pyramidal shaped termination before a-Si:H has been observed in a number of publications. In order to understand the growth mechanism of intrinsic a-Si:H on the c-Si (p) wafer we have decided to growth a series of films changing the deposition time from 15 seconds to 1800 seconds at 225 °C. Deposited films were characterized by SE and FTIR measurements.
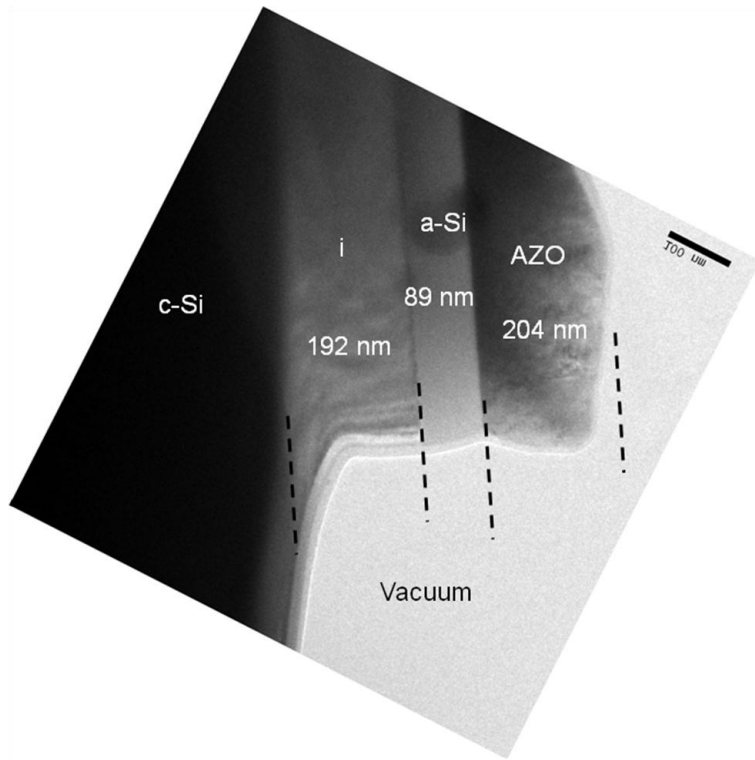
Figure 4.15 HRTEM micrograph of AZO/5 min deposited (n) a-Si:H/5min deposited (i) a-Si:H/c-Si.
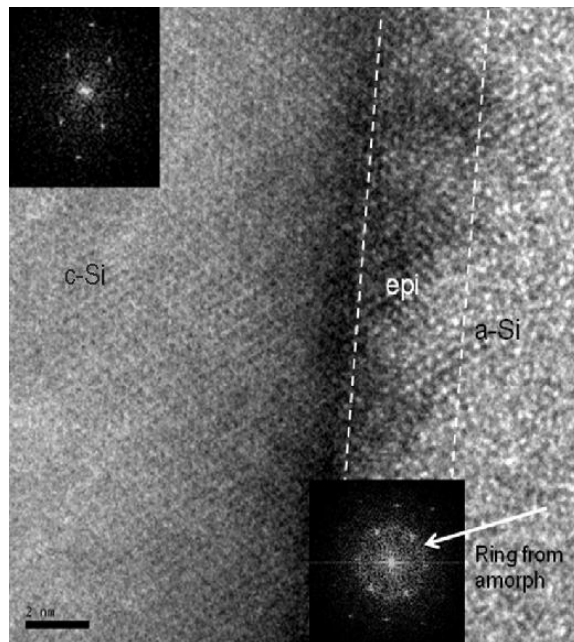
Figure 4.16 HRTEM micrograph of c-Si/(i) a-Si:H interface.

4.4.1 Spectroscopic Ellipsometry Analysis of a-Si:H/c-Si Interface

To search an anology between the SE results and HRTEM results, we have focused on 120s deposited intrinsic a-Si:H thin films on c-Si (p).

Figure 4.17 (left) shows imaginary component of the dielectric function for c-Si wafer and a-Si:H film deposited for 120s on c-Si wafer. Micro-crystalline phase in the films is identified from a bump with a shoulder at low photon energies [100]. Additionally, HRTEM image of 120s film is also presented in Figure 4.17 (right). From HRTEM and SE measurements, we have observed the presence of epi layer and the amorphous layer together in the structure of the deposited film.
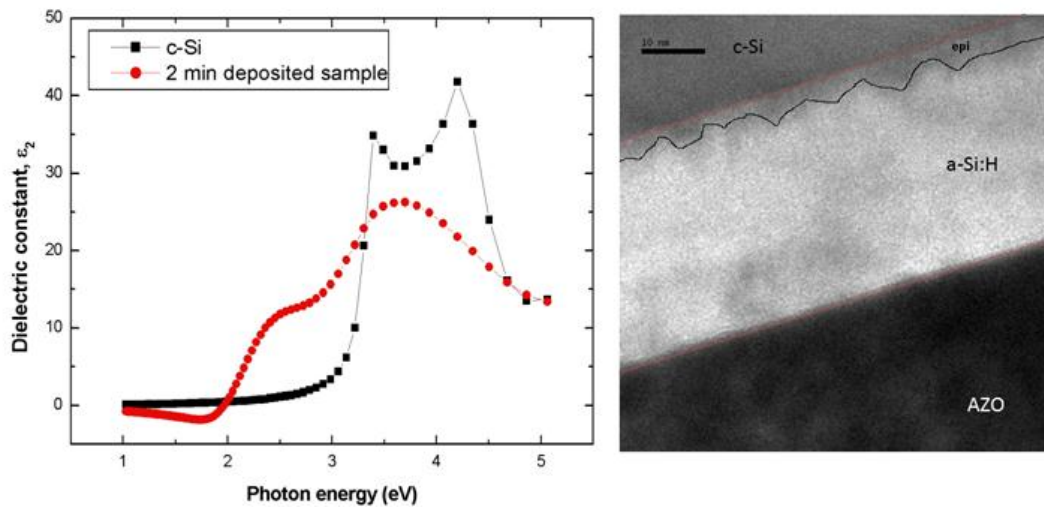
Figure 4.17 Photon Energy versus ε_2 Graph (left) and HRTEM Image (right) for 120s a-Si:H film.

In order to obtain the thickness and the optical parameters of the deposited layer, we have successfully applied a multilayer model. This model consists of : a crystalline silicon wafer as a substrate, linearly graded breakdown layer void on bottom and c-Si on top, another linearly graded breakdown layer that transitions from crystal silicon at the bottom and amorphous silicon at the top, an amorphous layer itself and as an indicator of surface roughness effective medium approximation of amorphous silicon and void, which gives a full history of the deposition, including the epitaxial layer thickness and the evolution of the breakdown into a-Si:H as shown in Figure 4.18.

Model is used to fit the measured SE data (Figure 4.19) and goodness of the fit is checked by the χ^2 which is a direct measure of discrepancies between measured optical data and the final best fit calculated data. Low χ^2, 0.066, indicates a good matching of model with the experimental data as shown by solid lines in Figure 4.19. Consequently, obtained parameters as a result of SE fit and the comparision of thickness values obtained both from SE and HRTEM results are given in Table 4.2 below, in which a very good agreement in film thickness is obtained.
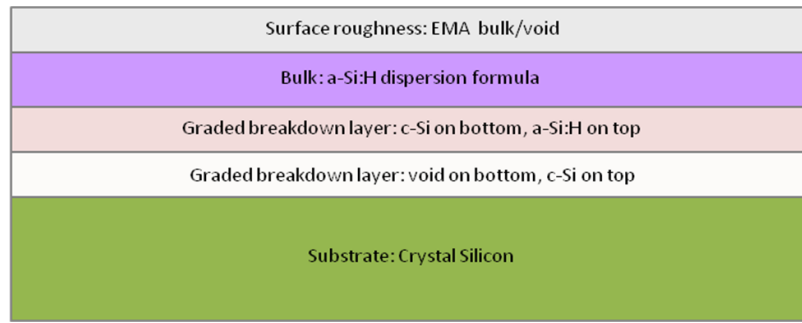
Figure 4.18 Multi layer model for 120 s deposited sample, representing the structure of the material as accurately as possible.

Other models has also been applied to fit the SE measurements presented in Figure 4.19 but, observed χ^2 value and results given in Table 4.3 clearly shows that model in Figure 4.18 successfully explains the evolution of microstructure of a-Si:H deposited at 225 °C on c-Si (p) substrate.
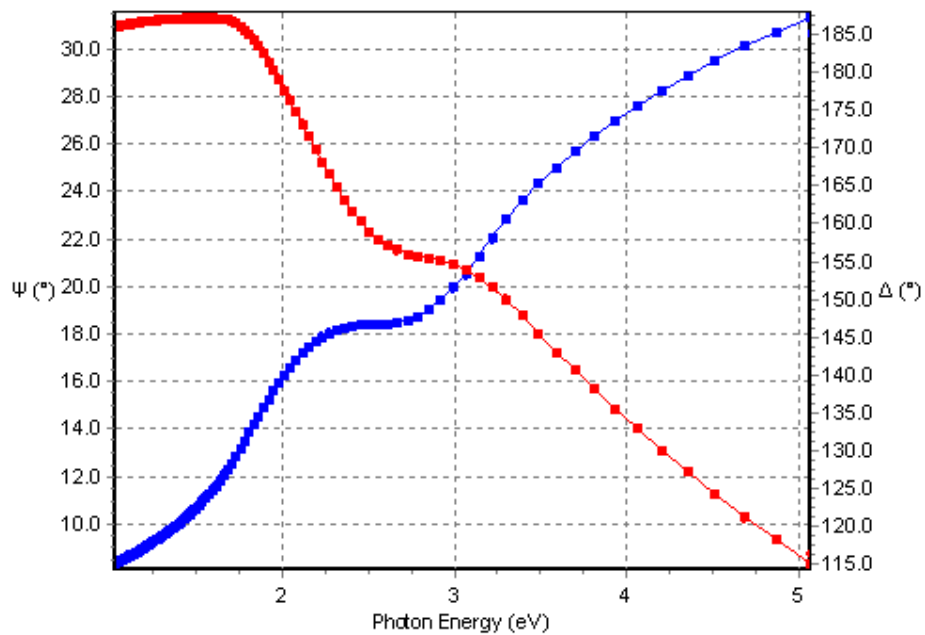
Figure 4.19 Matching of SE measurements (symbols) with model fitting (solid lines), for 120 s deposited sample.

Table 4.2 Comparision of SE and HRTEM results

	SE	HRTEM
L2 Thickness [nm]	7.18 ± 2.25	5
L3 Thickness [nm]	29.37 ±1.07	30
L4 Thickness [nm]	0.55± 0.01	-
a-Si-H_tl E_g [eV]	1.66 ± 0.01	-
a-Si-H_tl ε_∞	0.40 ± 0.04	-
a-Si-H_tl A	216.0 ± 3.3	-
a-Si-H_tl E_o [eV]	3.65 ± 0.01	-
a-Si-H_tl C	2.32 ± 0.02	-
χ^2	0.066	-

In order to understand the growth of microstructural variation of a-Si:H on c-Si substrate we have deposited a series of films from 15 s to 1800 s at 225 °C. Figure 4.20 shows measured dielectric constant of the films, where it is observed that the crystallinity decreases with deposition time. While, a-Si:H layer deposited at t = 15s and 30s exhibit similar optical constants as crystalline silicon, which implies that the films are nearly completely epitaxial; a broad featureless spectra for t=1800s suggests nearly a-Si:H structure. On the other hand, it is worth to note that observed distribution is not perfectly symmetrical and has a bump on the low energy side.
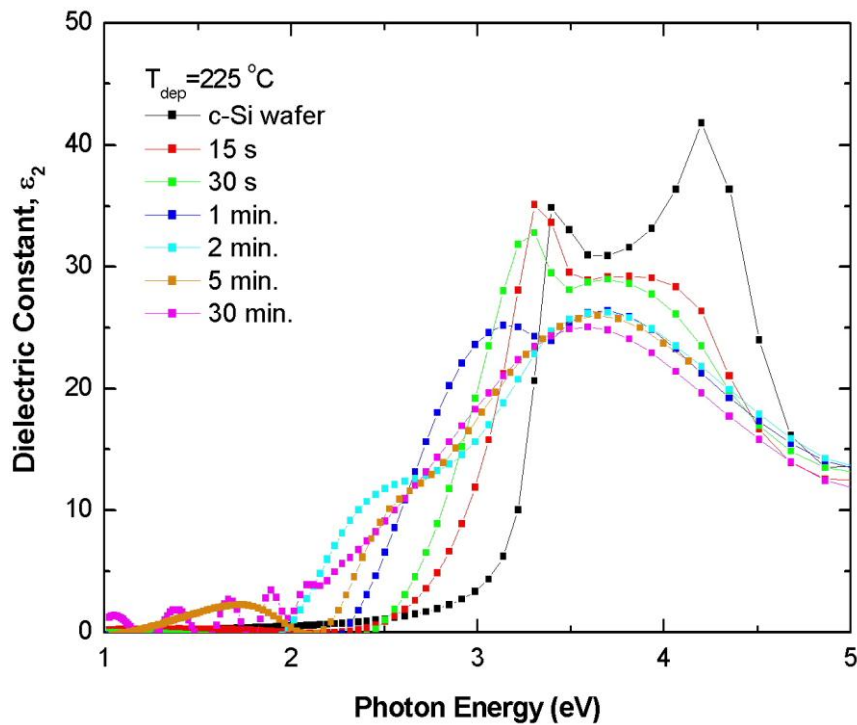
Figure 4.20 Imaginary part of the dielectric constant for the films with different deposition times.

Variation of the surface roughness is also another and clear indication of phase transformation of the growing film besides measured imaginary part of the dielectric constant. Film growth begins in an isolated nucleation sites on the substrate surface, which leads to rapid initial increase in the surface roughness. When continuous film formation starts, surface roughness rapidly decreases [101]. For the a-Si:H films deposited on c-Si wafers, surface roughness is low for a-Si:H films and increases for nano crystalline or micro crystalline films.

Surface roughness can be measured using AFM or calculated from the SE multi layer model given in Figure 4.18, in which the top of the layer is an indication of surface roughness defined by the mixture of void and a-Si:H.

Figure 4.21 shows variation in the surface roughness and bulk layer thickness as a function of deposition time deduced from analysis of SE measurements. Following a maximum, surface roughness decreases and starts saturating after 60s as expected. At very long deposition times surface roughness increases again indicating there could be mixed a-Si:H and μc-Si:H phase in the film growth. The roughness layer explains why the amplitude of the peak at 4.2 eV is smaller than the one from a bare c-Si wafer [41]. Bulk layer thickness increases linearly with deposition time, indicating that deposition rate being independent of growing films which could be epitaxial, nc, μc or a-Si:H.
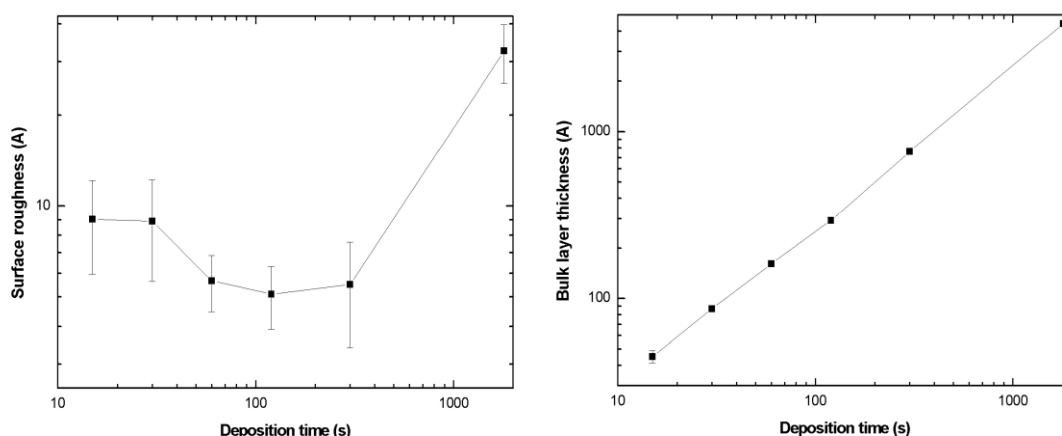
Figure 4.21 Variation of the surface roughness (left) and bulk layer thickness (right) of the a-Si:H films.

4.4.2 FTIR Analysis

Hydrogen bonding configuration of the deposited films was analysed by ATR Fourier transform infrared (FTIR) vibrational spectroscopy. During analyses, we have focused on the most informative Si–H stretch region between 1900–2250 cm^{-1}. As an example, deconvolution of IR spectrum for the 15s film is shown in Figure 4.22 where observed stretching modes are indicated. These are extreme LSMs (ELSM, 1895, 1929 and 1950 cm^{-1}), the low SM (LSM, 1980-2010 cm^{-1}) and two high SM (HSM, 2070–2100 cm^{-1}, 2120 cm^{-1}) [102]. Evolution of the FTIR spectrum with deposition time is presented in Figure 4.23. ESLM dominates the spectrum at early times suggesting that hydride-dense a-Si:H tissue, which either passivates the crystalline grain boundaries or fills the small pores is present in the films [102]. At 120s, where surface roughness is at a minimum value (Figure 4.21) a small

ELSM is observed while, HSM for both a-Si:H and μc-Si:H remarkably increases. As deposition time further increases, HSM modes slightly decrease while LSM increases suggesting mixed growth of a-Si:H and μc-Si:H. This suggest that growing film is mainly a-Si:H with μc-Si:H film grown at the interface.
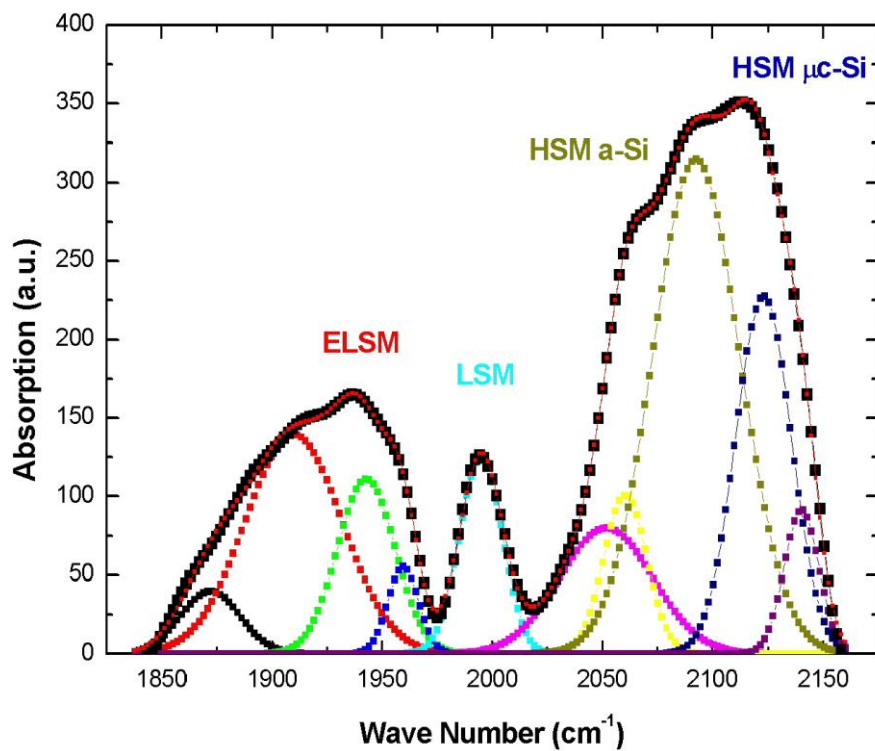
Figure 4.22 Hydride stretching modes in the FTIR spectra for 15 s film.
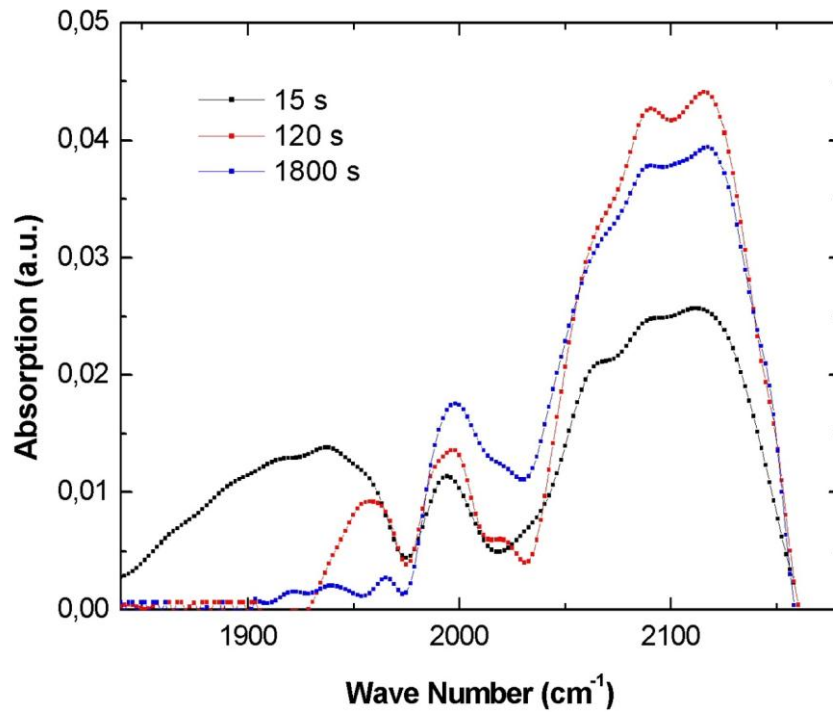
Figure 4.23 Variation of FTIR spectrum of the films at different deposition times.

4.5 Solar Cell Fabrication at 225 °C Substrate Temperature

As explained in Section 3.5.2, with the help of detected EL signal, it is possible to seperate the solar cell regions working with different performances. In Figure 4.24, Electroluminescence image (left) and deposited solar cell (right) for the films deposited at 225 °C substrate temperature; 0.6 Torr pressure; 12 mW/cm^2 and 5000 ppm doping ratio is given.
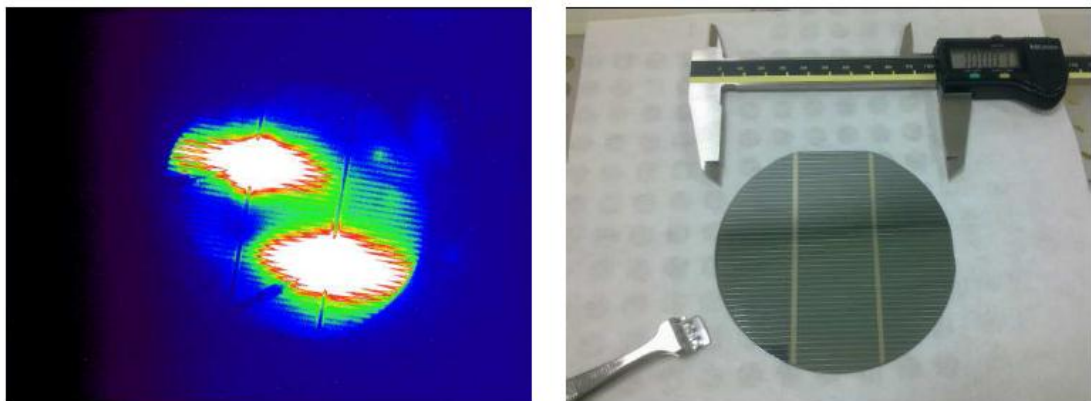
Figure 4.24 Electroluminescence image (left) and picture (right) of the solar cell deposited at at 225 °C substrate temperature; 0.6 Torr pressure; 12 mW/cm^2 and 5000 ppm doping ratio.

As it can be seen from the EL image, the elliptical areas in the close neighborhood of the contact points of the solar cell have high efficient, whereas the contribution of the other regions to the measured current is quite low. This shows that the top electrode surface conductivity requires improvement. Measured efficiency of this cell is 4.6 % .

A series of studies on thickness optimizations for both the doped and the intrinsic layers have been conducted in order to improve the solar cell with 5000 ppm doping concentration rate. Additionally; before back contact deposition wafer were immersed into 2% HF solution till hydrophobic surface is observed, to increase carrier collection thickness of front contacts has been increased and Al/Ag alloys is used instead of aluminium.

The final I/V curve of solar cell with Al/Ag front contact/a-Si:H(n)/a-Si:H(i)/c-Si(p)/Al back contact structure, measured under AM1.5G illumination is given in Figure 4.25. With the new modifications, the efficiency of the solar cell is increased to 9.2%.

As a result of better back surface cleaning of the c-Si wafer and improvement of top electrodes, solar cell efficiency has been increased from 4.7% to 9.2%. Short circuit current is clearly increased due to improvement of the front contacts whereas, only a small improvement, 22 mV, in the V_{oc} is observed. Low V_{oc} value resulted from the presence of the epitaxial layer within the c-Si/a-Si:H interface. With its $72 cm^2$ active area this is the largest studied active area SHJ solar cell presented in the literature on p-type, <100> oriented on c-Si is wafer.

EL image measured in dark, applying open circuit voltage to the solar cell, is given in Figure 4.26. It is obvious from the figure that a much larger region of the solar cell contributes to the current. The dark regions are believed to result from the lack of pasivation due to the less homogenized intrinsic layer with 10-20A thickness.
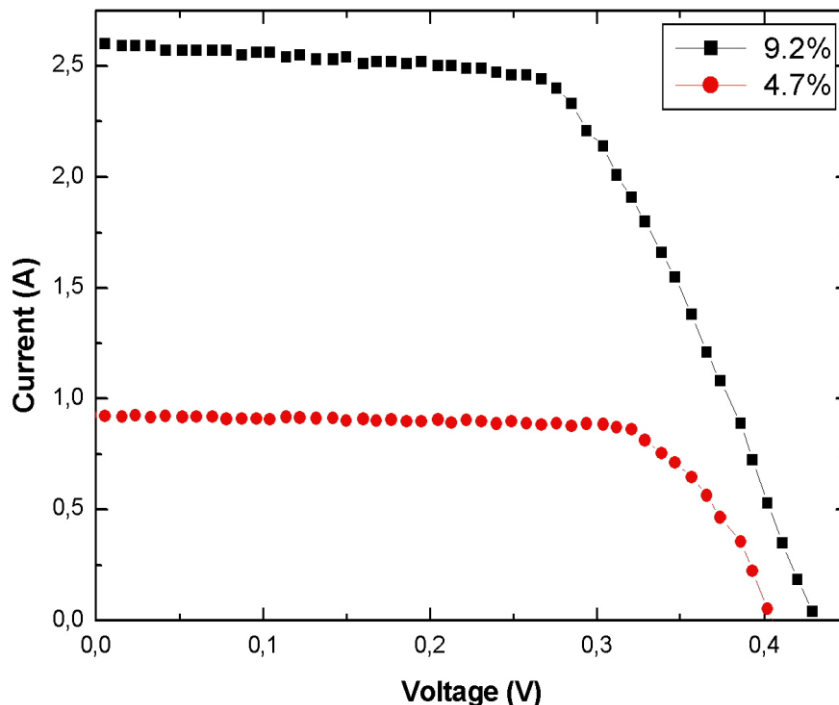
Figure 4.25 I-V curve of the solar cell after the optimization studies under AM 1.5G solar simulator light.
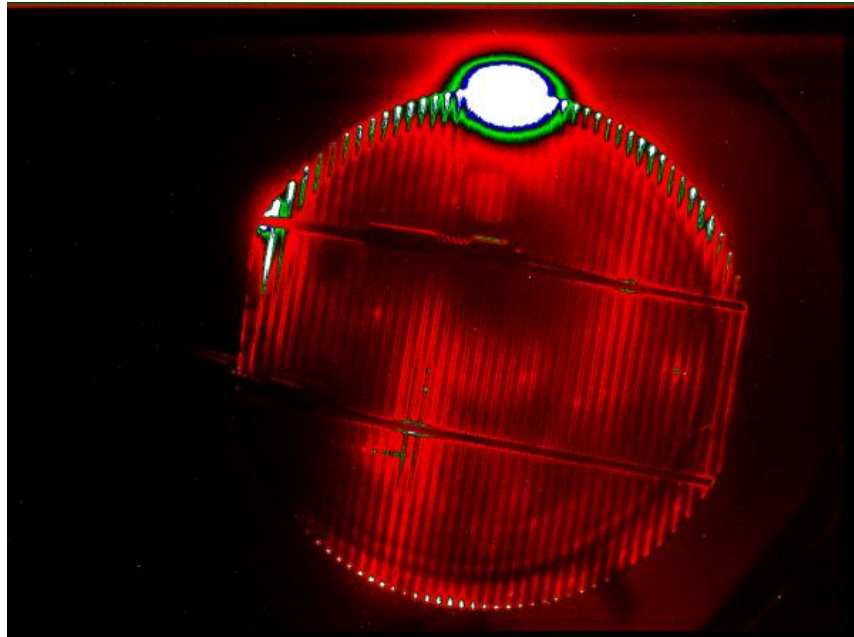
Figure 4.26 Electroluminescence image of the solar cell after optimization studies.

4.6 Deposition of SHJ Solar Cells Below 225 °C

The optimum passivation quality of a-Si:H films are generally obtained in temperature range of 200 and 250 °C [45] within a quite small process window. Appropriately, in our deposition temperature studies we have obtained the 225 °C as an optimum deposition temperature.

Besides, from the HRTEM and SE results of intrinsic a-Si:H layers deposited at 225 °C, we have observed that there is a partial epitaxial growth at the beginning of the film deposition, which cause to decrease in the c-Si surface passivation.

In order to get rid of the epitaxial growth and increase the throughput, in this part of the thesis we have deposited the a-Si:H layers at a low temperature well below the optimum temperature and recovered the layer in an additional post annealing step [39,45-48].

At the beginning of the studies, we have decided to work in low substrate temperature at 130 $^{\circ}$C at different rf powers in order to find the optimum rf power value for the a-Si:H intrinsic layer deposition. From 130 $^{\circ}$C substrate temperature spectral ellipsometry results (Figure 4.27) we have obtained that the intrinsic layer still contains some microcrystallinity in its structure up to rf power of 14 Watt. Shoulder at low photon energies lost at 20 Watt rf power, indicating the structure of the deposited film is amorphous. On the other hand, when we apply these substrate temperature and rf power values as the solar cell intrinsic layer deposition parameters, solar cell device is failed and we could not get good result with this parameters.
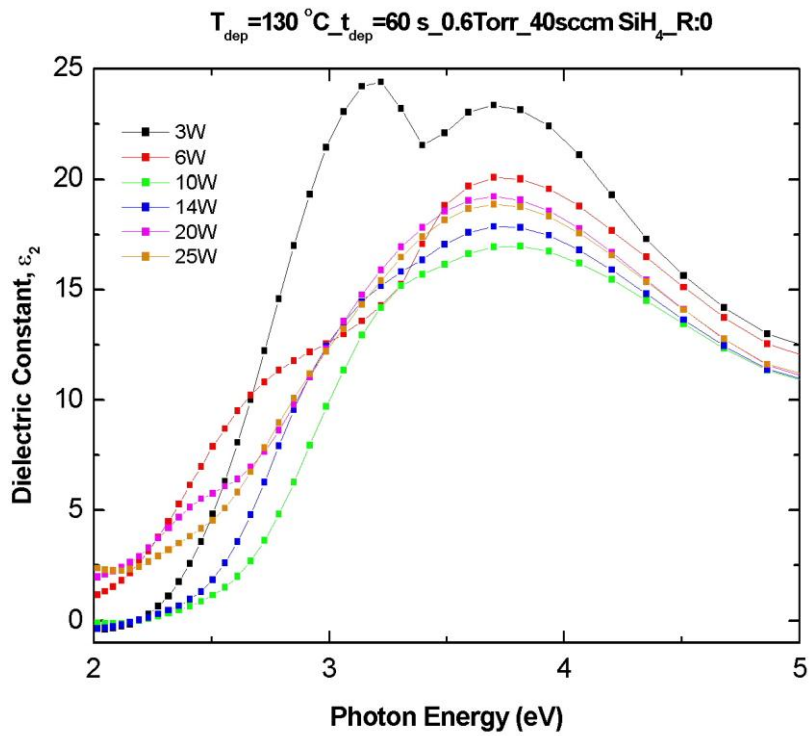
Figure 4.27 Dielectric constant variation of the films with respect to RF power.

Accordingly, in order to obtain a high quality intrinsic a-Si:H layers with the improved passivation property and suppression of epitaxial deposition we have decided to apply some innovations to our deposition procedure: It is known that by diluting the silane deposition precursor with hydrogen, the quality of the resulting a-Si:H layers can be increased in terms of microscopic parameters such as the bulk defect density or hydrogen microstructure [7]. Therefore, a typical dilution ratio of $R_H=[H_2]/[SiH_4]=10$ is decided to take part into the intrinsic layer deposition process and in order to ignite this plasma we started to use slightly higher pressure (0.8 Torr) as a new deposition parameter. Additionally, for the suppression of the epitaxial growth, deposition temperature of the film is decreased. Different sets of films were deposited details of which were given in Table 4.4. Deposition time for the intrinsic and doped layers were kept constant for all cases as 60 s and 120 s respectivly.

Table 4.3 Deposition parameters for the SHJ solar cells at low temperatures.

Set	i layer ^oC $T_{substrate}$ (^oC)	n layer $T_{substrate}$ (^oC)	R_H $[H_2]/[SiH_4]$	Pressure (Torr)	Power (mW/cm^2)
I	100 … 225	100 … 225 ($T_i=T_n$)	0		
II	100 … 225	100 … 225 ($T_i=T_n$)	10	0.8	12
III	100 … 225	190 and 225			

Figure 4.28 shows the efficiency and fill factor variation of the as deposited solar cells for Al-Ag/(n) a-Si:H/(i) a-Si:H/(p) c-Si/Al structure in which the i layer substrate temperature varied for the fixed 225 °C n layer substrate temperature. Figure 4.29 shows the I_{sc} and V_{oc} variations for the same conditions. These values are as deposited values of the samples. We observed existence of a process window between about 140 °C and 190 °C for the i layer,when n layer substrate temperature is kept at 225 °C . According to these curves it can be observed that we can obtain the highest efficiency (6.17 %) and highest V_{oc} (0.475 V) values for the i-layer substrate temperature at 170 ^oC for the as deposited case. Nevertheless, it has very low fill factor value, which is 38 %. For that reason we have decided to continue our studies with the 150 °C i-layer substrate temperature for which the efficiency, FF, V_{oc} and I_{sc} values are 5.29 %, 51 %, 0,486 V and 1.5 A respectively.
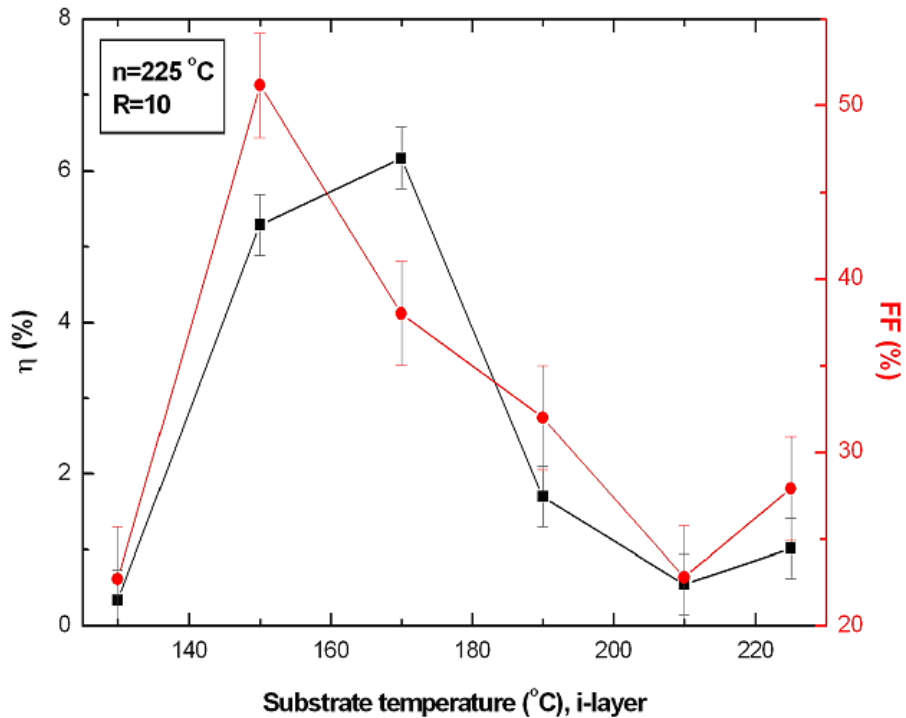
Figure 4.28 Efficiency and FF variation of the deposited structures according to intrinsic layer deposition temperature.

71
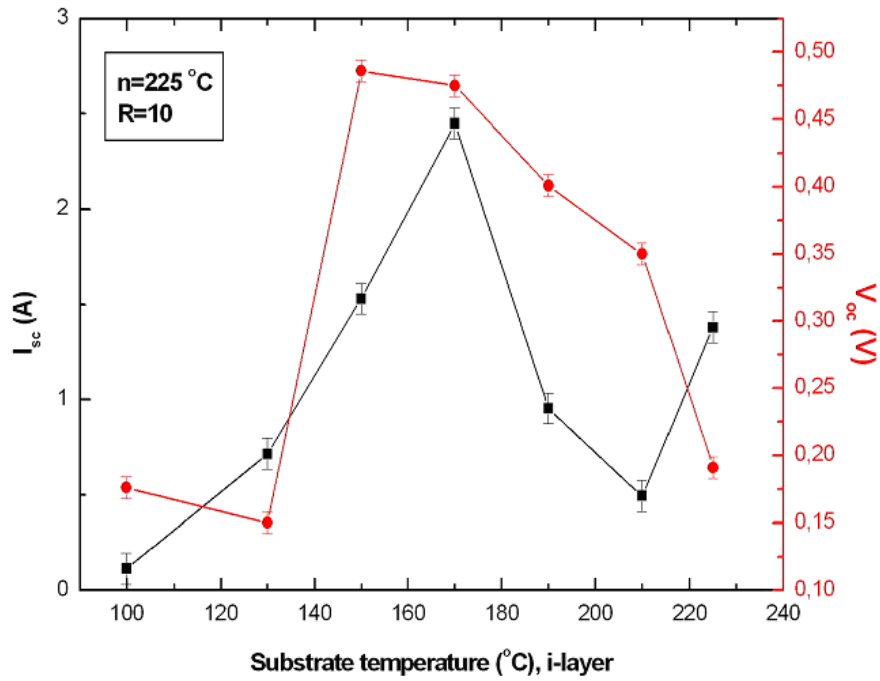
Figure 4.29 I_{sc} and V_{oc} variation of the deposited structures according to intrinsic layer deposition temperature.

When n layer substrate temperature was fixed at 190 °C, we again observed the existance of process window between about 190 °C and 210 °C as shown in Figures 4.30 and 4.31. It can be concluded that even though the highest efficiency (4.79 %) is obtained at 210 °C , since it has a low FF value, we have decided to continue our studies with the 190 °C i-layer substrate temperature for which the efficiency, FF, V_{oc} and I_{sc} values are 4.29 %, 46 %, 0,458 V and 1.46 A respectively.
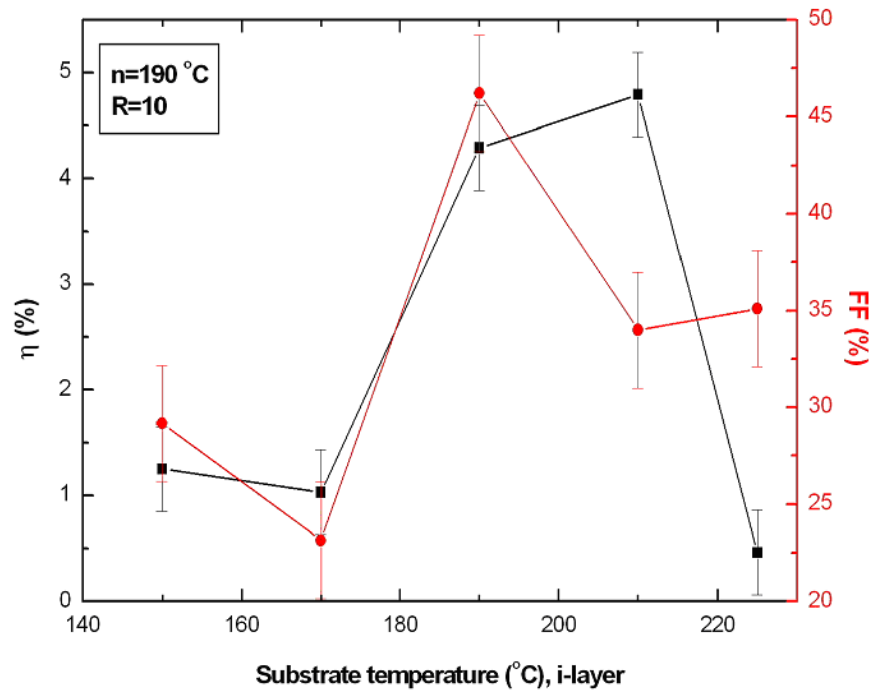
Figure 4.30 Efficiency and FF variation of the deposited structures according to intrinsic layer deposition temperature.
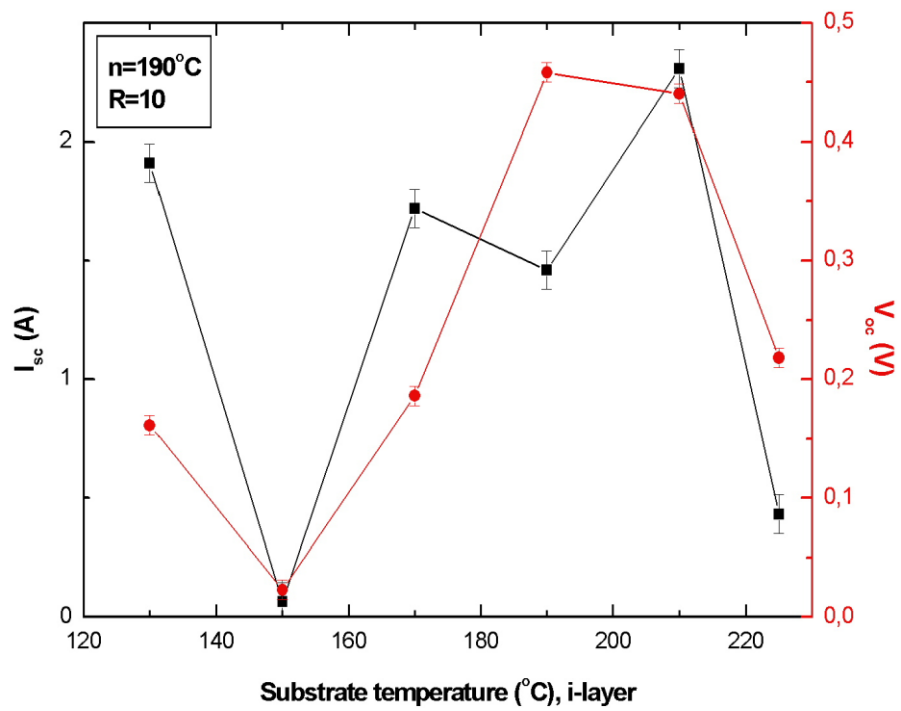
Figure 4.31 I_{sc} and V_{oc} variation of the deposited structures according to intrinsic layer deposition temperature.
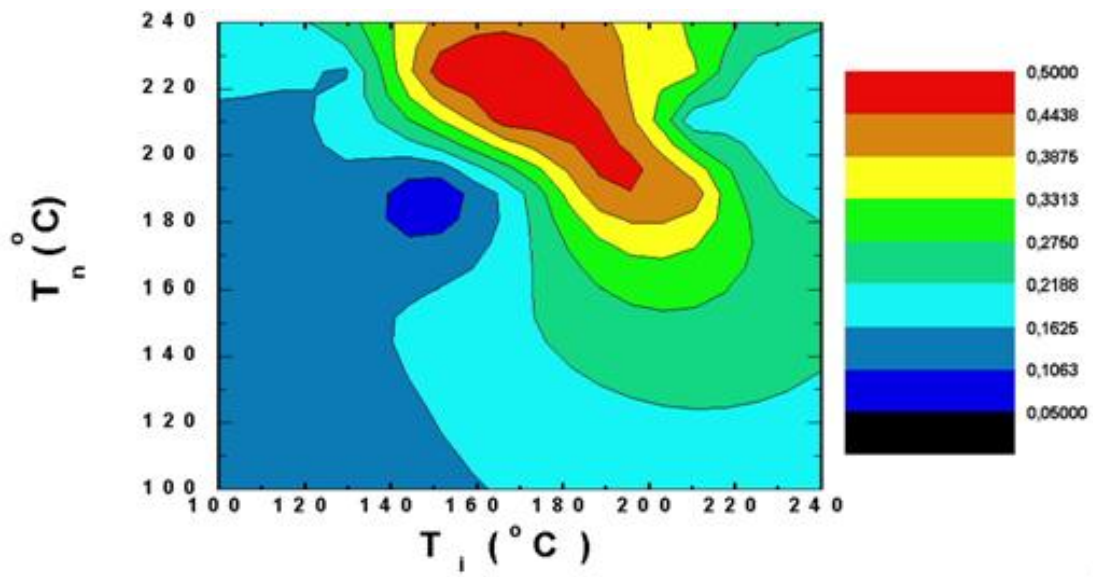
Figure 4.32 3D contour V_{oc} of solar cells as a function of i- and n- layer deposition temperatures.
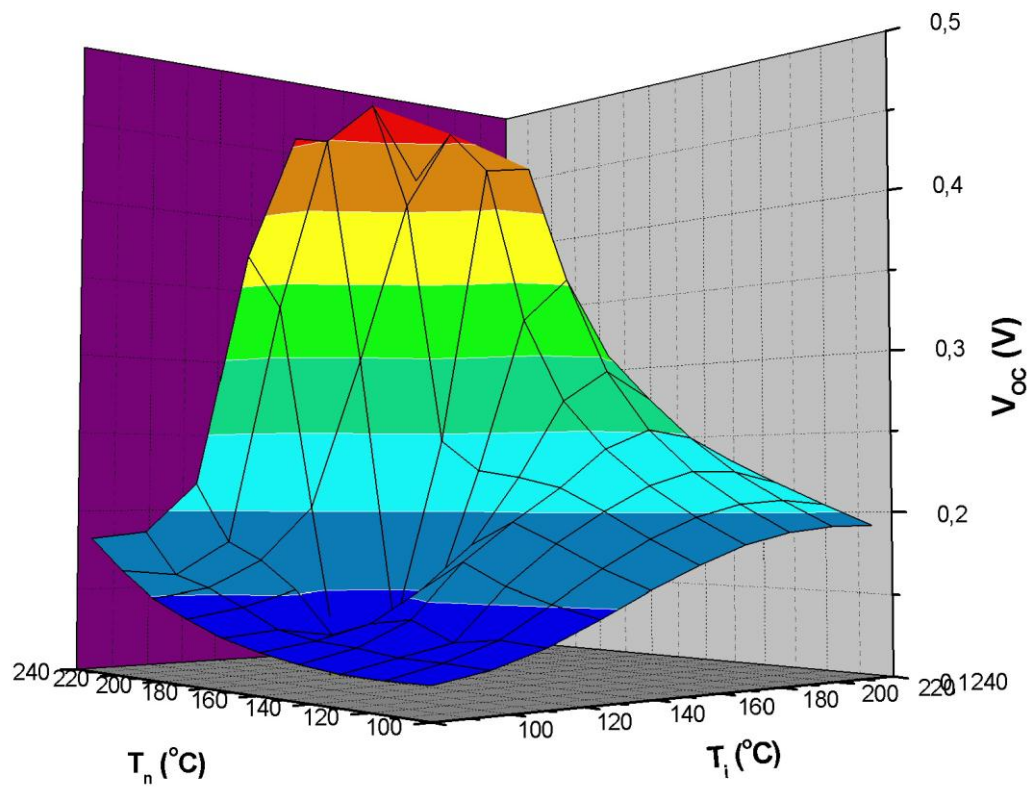
Figure 4.33 3D plot V_{oc} of solar cells as a function of i- and n- layer deposition temperatures.

As pointed before, V_{oc} is a measure of a surface passivation in SHJ solar cell. To understand better the process window we have plotted V_{oc} values of the cells in Table 4.3 as a function of i- and n- layer deposition in Figure 4.32 and 3D plot in Figure 4.33. According to the graph all the cells in Set I and Set II are failed. In the ≤ 200 ^{o}C temperature region, we realized an existence of process window for the deposition temperature of intrinsic and n-doped layers in our PECVD system. Consequently, we have continued our annealing studies for the devices produced in Set III.

4.7 Annealing of SHJ Solar Cells Deposited at Low Temperatures

Post annealing of samples those solar cell parameters are summarized from Figure 4.34 throug Figure 4.39 has been performed at 150°C and at 250°C with varied annealing durations on a hot plate in laboratory environment.
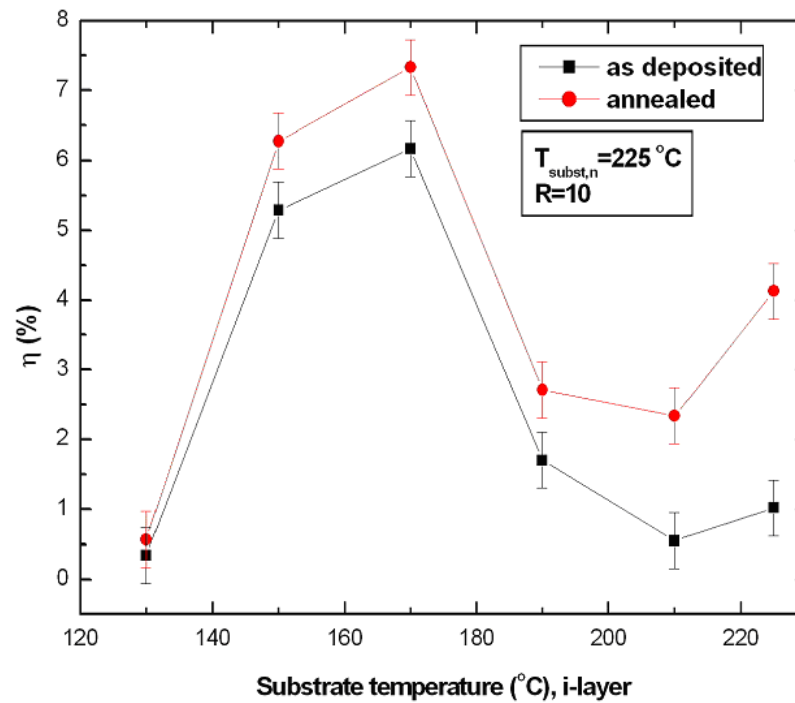
Figure 4.34 Effect of annealing on the efficiency of the deposited structures according to intrinsic layer deposition temperature, at 225 °C n layer deposition temperature.
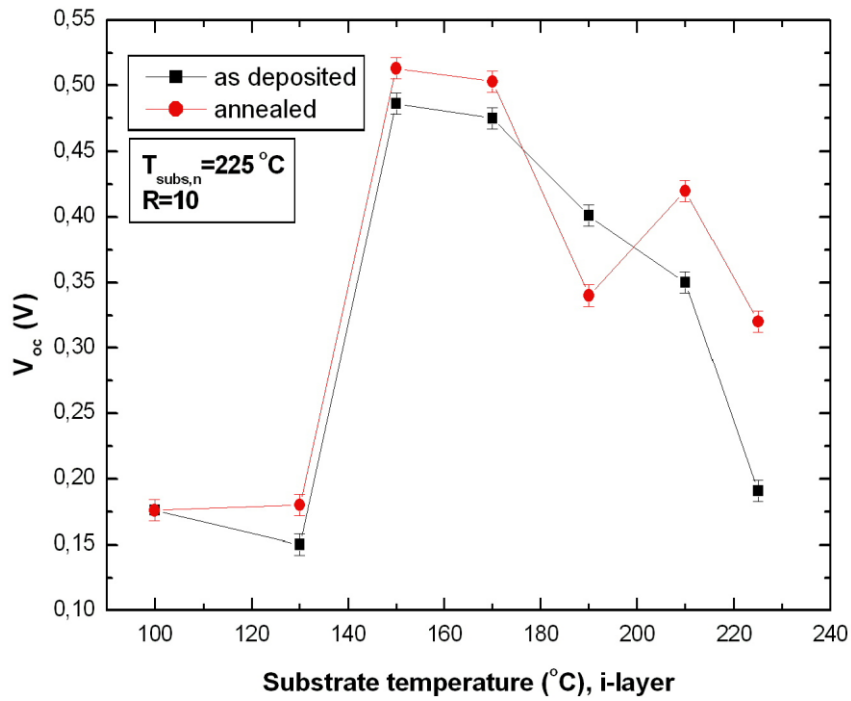
Figure 4.35 Effect of annealing on the V_{oc} of the deposited structures according to intrinsic layer deposition temperature, at 225 °C n layer deposition temperature.
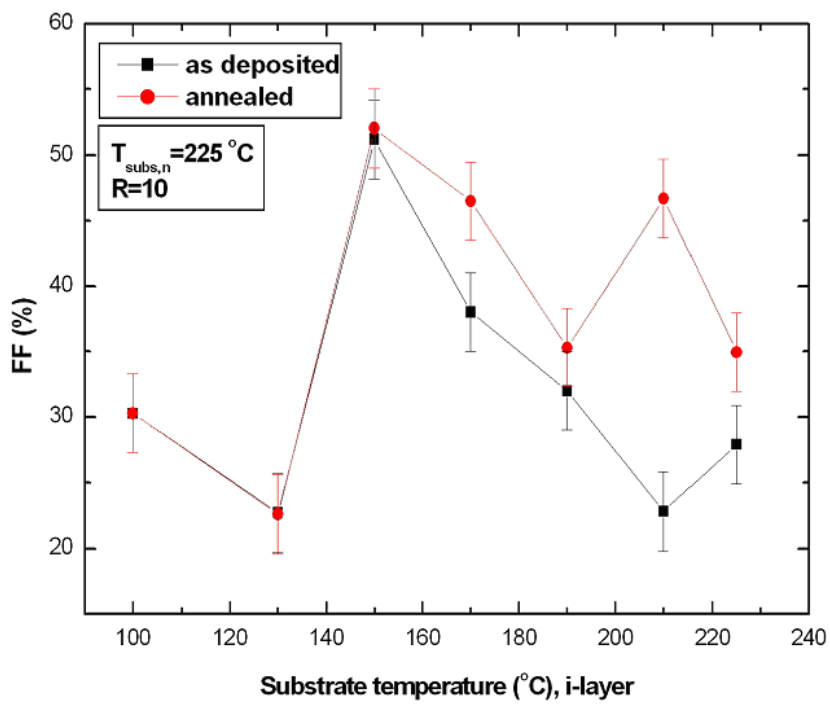
Figure 4.36 Effect of annealing on the FF of the deposited structures according to intrinsic layer deposition temperature, at 225 °C n layer deposition temperature.
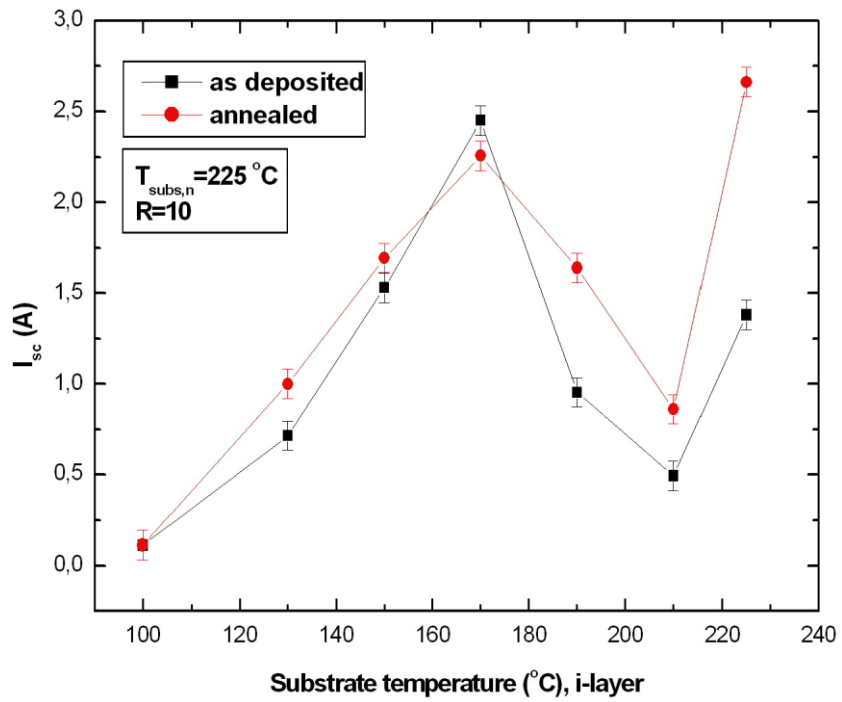
Figure 4.37 Effect of annealing on the I_{sc} of the deposited structures according to intrinsic layer deposition temperature, at 225 °C n layer deposition temperature.
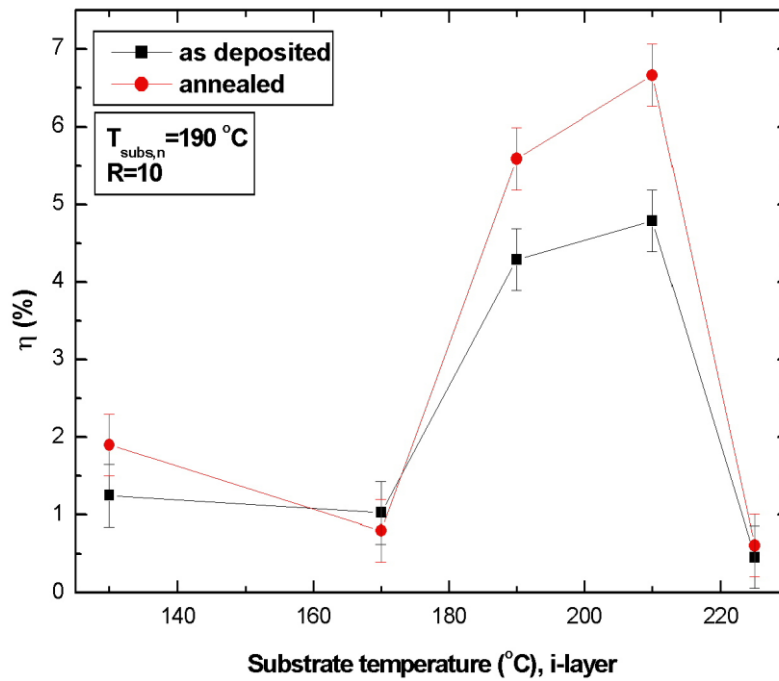
Figure 4.38 Effect of annealing on the efficiency of the deposited structures according to intrinsic layer deposition temperature, at 190 °C n layer deposition temperature.
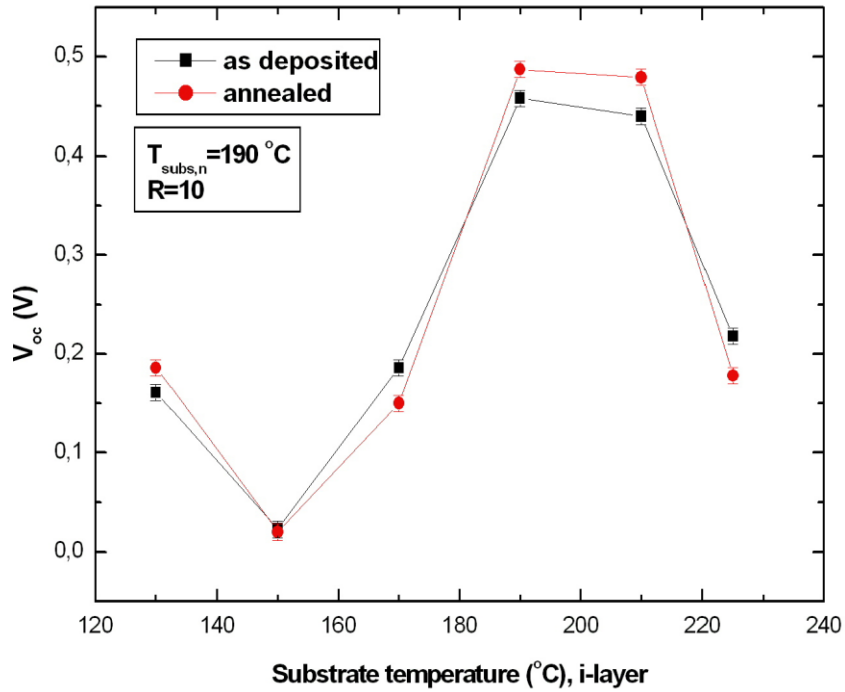
Figure 4.39 Effect of annealing on the V_{oc} of the deposited structures according to intrinsic layer deposition temperature, at 190 °C n layer deposition temperature.
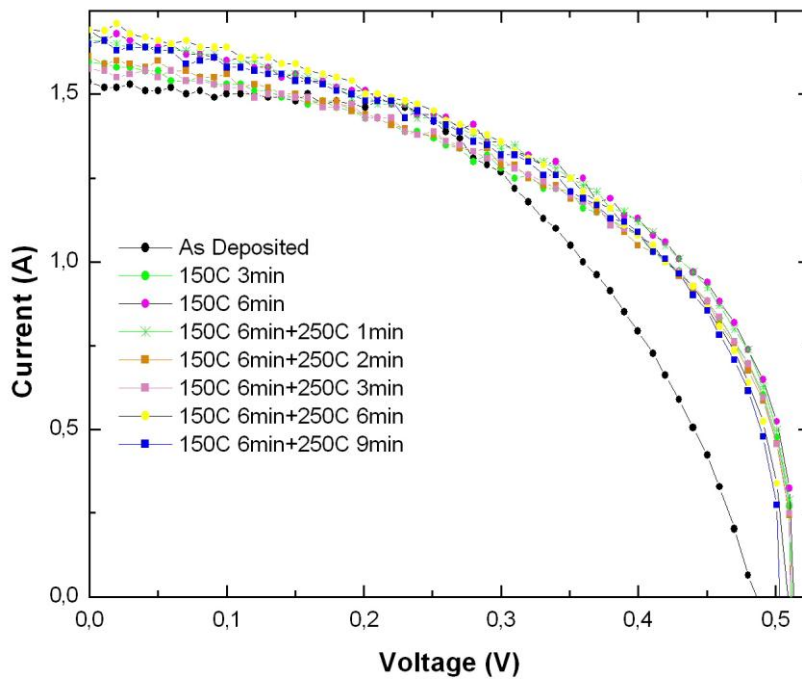
Figure 4.40 Current-Voltage improvement graph with annealing of the film deposited at n=225 °C, i:150 °C, R:10.

The general improvement in the current voltage curve of the choosen sample is given in Figure 4.40. When we checked our results after annealing, from Figures 4.34, 4.35, 4.38 and 4.39 graphs; we have observed a small improvement in V_{oc} (30 mV) within the cells rather than expected, which may indicate that there is still epi layer in heterostructure, which is also proved by the SE measurements. Additionally, it is assumed that the reason for the limitation of the V_{oc} to a range around 513 mV is due to the recombination at the local metal contacts at the backside and the used Si-substrate with a resistivity of 1-20 ohm cm [45] as well as the nc behaviour of intrinsic layer.

Similar results were also obtained from Jeon and Komisako [49]. For the films, deposited with low SiH_4 flow rate (5 sccm), they did not observe an improvement in the effective lifetime measurements. They assumed that the reason of this low improvement is the high surface recombination velocity at the interface, which has $(Si-H_2)_n$ bonds and in micro-crystalline structure. $Si-H_2$ bonds in the structure of the film means defects in the film and it indicates low quality film. Increase in the Si-H bond in the structure of the film indicates that good quality a-Si:H thin films are formed.

De Wolf and Kondo [53] have observed that no lifetime improvement upon annealing was observed when the growth was not purely amorphous. Similar results have also observed by Labrune [34] as well.

In Figure 4.41 you can see the solar cell parameters variation as a function of annealing time. The cell is annealed at 150 °C for 6 minutes and at 250 °C for 9 minutes on a hot plate in ambient air.

In the first 3 minutes of the annealing process, we have observed an increse in all the cell parameters. Increase in the I_{sc} can be explained by the improvement the ohmic behaviour of front metal contact [33]. Increase in the V_{oc} can be attributed to the improvement of the a-Si:H layer with the hydrogen diffusion within the structure for improving surface passivation and overall solar cell performance [33, 52].

3 to 6 minute interval we have observed that I_{sc} continues to increase, while V_{oc} reaching saturation. This means that the front metal contacts continue to improve but there is no more hydrogen diffusion within the structure. The highest efficiency for this cell was obtained 6 minutes of annealing at 150 °C.

After 8th minutes, within the 250 °C annealing temperature, we have observed a small decrease in V_{oc} values, indicating a start in hydrogen effusion.

A longer annealing time at 250 °C ends up with a depletion of hydrogen from the interface, which leads to a lower passivation quality. The annealing step seems to activate a diffusion of very weakly bonded hydrogen in the layer. This diffusing hydrogen is assumed to create a more stable interatomic binding in a favorable position [45].
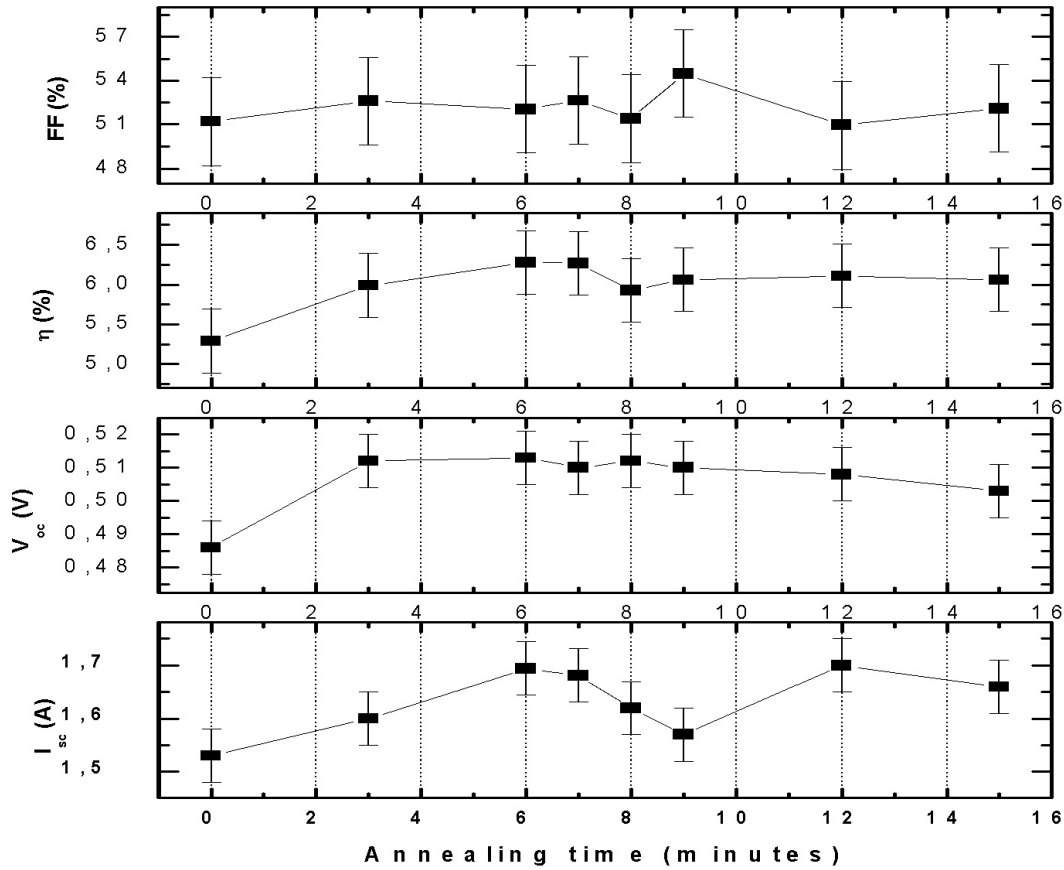
Figure 4.41 Measured I_{sc}, V_{oc}, FF and efficiency variation of i:150 °C, n:225 °C substrate
temperatures c-Si/a-Si:H HJ solar cell as a function of annealing time.

Partial thermal equilibrium between the different bonding configurations of point defetcs or impurities
in the a-Si:H films after the annealing process can be calculated from the barrier energies of the
various states and the kinetics of the reaction. Temperature dependence of Barrier energy is given in
equation 4.2 and the solar cell parameters parameters variation as a function of barrier energy is given
in Figure 4.42.

$$E_B = kT\ln(\tau_R\omega_o)$$ (4.2)

where, ω_o : attempt to escape frequency (10^{12}-10^{13} s^{-1})

E_B: Barrier energy (eV)
k: Bolzmann constant (8.617×10^{-5} eV/K)
T: Applied temperature (K)
τ_R: Annealing time (s).
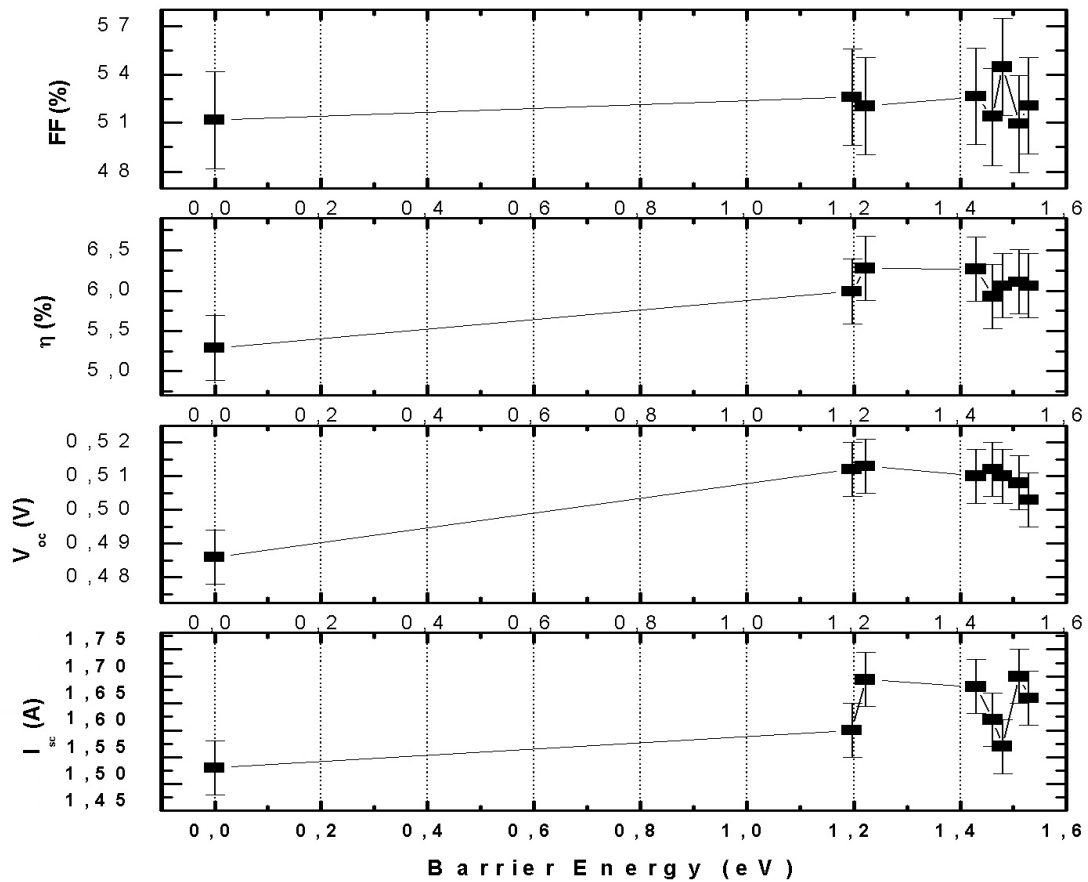
Figure 4.42 Measured I_{sc}, V_{oc}, FF and efficiency variation of i:150 °C, n:225 °C substrate temperatures c-Si/a-Si:H HJ solar cell as a function of barrier energy.

The diffusion of hydrogen from the a-Si:H layer to the c-Si surface is important for improving surface passivation and overall solar cell performance. In the early studies, as an explanation of the surface passivation it has been assumed that the hydrogen is diffused from the thin film bulk layer to the c-Si surface [104]. Nevertheless; since the minimum 2.49 eV energy is necessary to release the bonded hydrogen, it must either already be in a free or quasi-free state [52]. Since there are high density of dangling bonds, it is not possible to be free of hydrogen in the structure. Additionally low temperature thermal annealing and a relatively high defect density 10^{15}–10^{17} cm^{-3} would significantly inhibit a bulk diffusion of hydrogen toward the interface for surface passivation [52].

Mitchell et al. [52] have calculated activation energy for the surface passivation as 0.7±0.1 eV, independent from the bulk layer thickness and they have concluded that the lower activation energy value indicates that surface passivation is controlled by surfaces states, rather than bulk diffusion processes. Annealing process leads the rearrangement of hydrogen already present at the interface prior to deposition (HF-dip step) or else from hydrogen deposited during the initial stages of deposition.

From the barrier energy graph we have observed a small improvement within the energy of 1.2-1.3 eV. In order to explain the mechanism behind this improvement we have two suggestion: We believe that on the cleaned wafer surface, after HF dipping c-si wafer surface is passivated by many H atoms. In the PECVD system, when the film grows, many of these H bonds replace with SiH$_3$ molecule

leading to either epi- or a-Si:H growth. On the other hand, some of the Si-H bonds may preserve their original position or additional H would come from the plasma species.

During annealing process, broken of a weak Si-Si bonds close to the surface and bond switching with the surface hydrogens would improve the surface passivation and improve the solar cell parameters.

Alternatively, again weak Si-Si bonds next to the interface are broken by the applied temperature. One of the created Si-DB configuration is passivated by the hydrogen, already exist at the interface, and the other Si-DB configuration is recombined with the unterminated bond on the wafer surface, resulted with an improvement of the wafer surface passivation.

Our suggestions, which is based on the passivating hydrogen already present in the near-surface reagen can be supported by the depth profile of hydrogen graph [105], measured before and after annealing at 350 ^{o}C, given in Figure 4.43 below. Figure shows that there is an evident decrease in the hydrogen intensity at the c-Si/a-Si:H interface during the annealing.
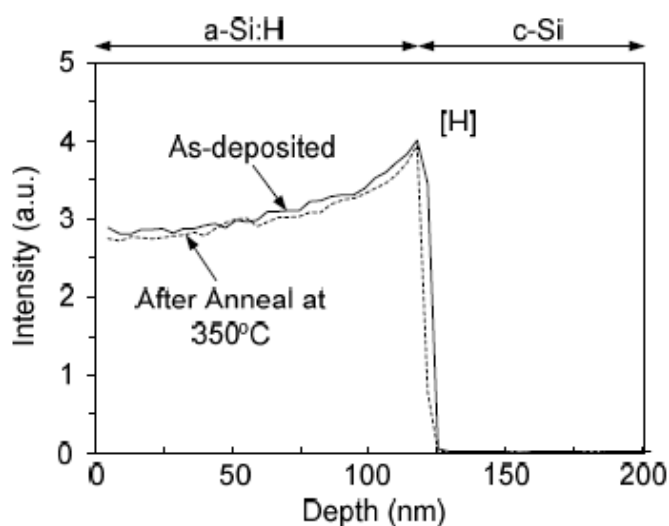
Figure 4.43 Hydrogen SIMS profile on n-type c-Si wafers passivated with a-Si:H before and after annealing at 350 ^{o}C [105].

Schulze [7] has concluded that intrinsic layers lead to an increase in V_{oc} only if intrinsic buffer layers are incorporated on both sides. Buffering just the (n) a-Si:H on the emitter side leads to no change in V_{oc}.

Based on these results we have decided to recontrol the intrinsic layer deposition conditions in order to prevent the epitaxial formation within the first nanometers of the layers and we have decided to perform annealing studies on the double side solar cell structure.

Additionally, in order to deposit epitaxially free layers for the intrinsic layer deposited at 150 °C substrate temperature with 40 sccm SiH_4 gas flow and 60 Watt RF power, we have studied the effect of hydrogen dilution ratio to the structure with SE measurements from the dielecric constant graph, given in Figure 4.44. From the Figure we have observed that even we have increased the hydrogen dilution ratio up to 2.75, which is the maximum available value that can be applied by the system

mass flow controllers for 40 sccm SiH$_4$ gas flow, there is still nc shoulders at low energies. Based on this result, with the present system we have decided to work with different RF power values by fixing the hydrogen dilution ratio to 1 (Figure 4.45).
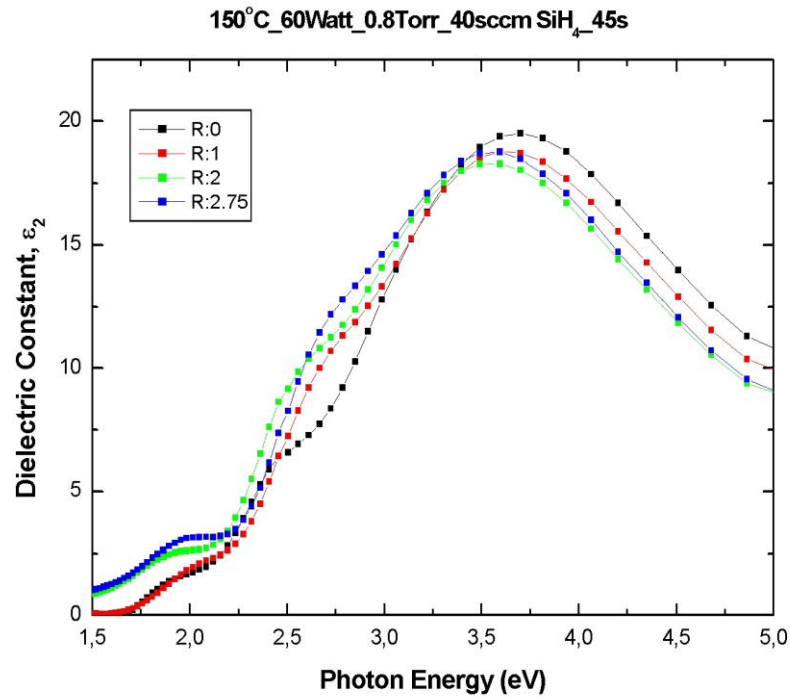
Figure 4.44 Dielectric constant variation of the films with respect to [H$_2$]/[SiH$_4$] ratio, deposited at 150 °C, 60 Watt.
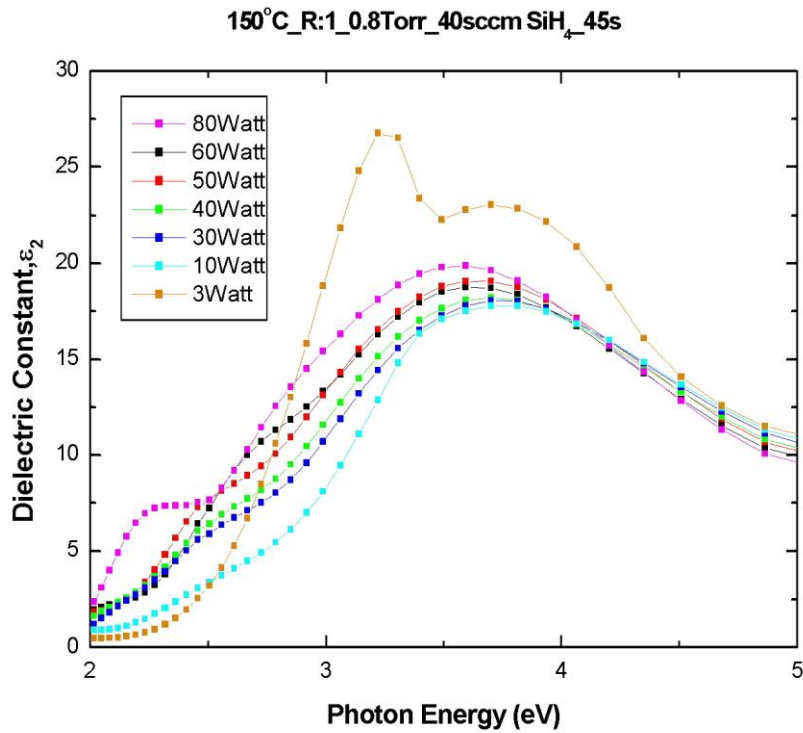
Figure 4.45 Dielectric constant variation of the films with respect to RF power, deposited at 150 °C, [H$_2$]/[SiH$_4$]=1.

From the SE dielectric constant results of the deposited layers with RF power value varies from 3 Watt to 80 Watt we have observed that at hydrogen dilution ratio [SiH$_4$/H$_2$]=1 and at 80 Watt RF power the deposited intrinsic layers shows an amorphous behaviour with a broad peak around 3.6 eV. When we apply a SE multilayer model to this sample, given in Figure 4.46, we have observed the deposited layer is complately amorphous with 2 nm/sec deposition rate.

Figure 4.46 SE multilayer model for the intrinsic a-Si:H thin film deposited at 150 °C substrate temperature, R:1, 80 Watt, 0.8 Torr, 45 seconds on (p) c-Si wafer.
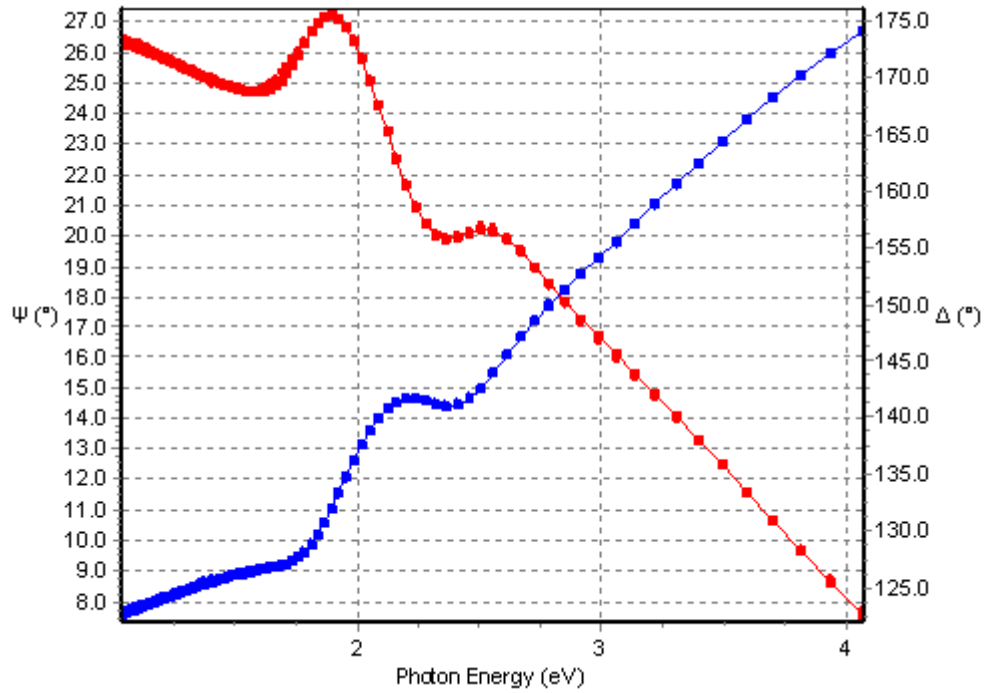
Figure 4.47 SE fit with χ^2 0.063, for the intrinsic a-Si:H thin film deposited at 150 ^{o}C substrate temperature, R:1, 80 Watt, 0.8 Torr, 45 seconds on (p) c-Si wafer.

From the Tauc-Lorentz dispersion formula, the obtained parameters from the multilayer model for the deposited film are given in Table 4.5.

Table 4.4 Deposited layer parameters obtained from SE fit

L1 Thickness [nm]	0.14 $\pm$ 0.06
L2 Thickness [nm]	92.51 $\pm$ 0.80
L3 Thickness [nm]	10.76 $\pm$ 0.48
L1 % void	40.76 $\pm$ 16.12
L3 % a-Si:H	86.95 $\pm$ 0.61
a-Si-H_tl E_g [eV]	1.67 $\pm$ 0.01
a-Si-H_tl ε_∞	1.18 $\pm$ 0.07
a-Si-H_tl A	193.7 $\pm$ 3.9
a-Si-H_tl E_o [eV]	3.45 $\pm$ 0.01
a-Si-H_tl C	2.17 $\pm$ 0.02
χ^2	0.062

4.8 Doped and Intrinsic a-Si:H Layers Thickness Optimization

In the next step, the thickness of the a-Si:H(n) layer was optimized. For this purpose, the n layer deposition times have been varied as 15s, 20s, 30s, 40s, 60s and 120s while keeping i-layer deposition time constant at 60s. These cells are deposited on the (100) p-type, 1-20 ohm-cm, 375μm wafers. n-layer thickness parameters are also studied in the solar cell structure of Al/Ag front contact/a-Si:H (n)/a-Si:H(i)/c-Si(p)/Al.

Obtained parameters with varing a-Si:H(n) layer thickness is given in Figures 4.48 and 4.49 below. At the end of n-layer deposition time studies, since it gives maximum efficiency and V_{oc} values, we have decided to work on 20s.

Thickness value of 20 s deposited n-layer is obtained from the HRTEM result. According to the HRTEM results deposition rate of n-layer is 3 A/s, which indicates that the optimum n-layer thickness is selected as 6 nm for our solar cell applications.
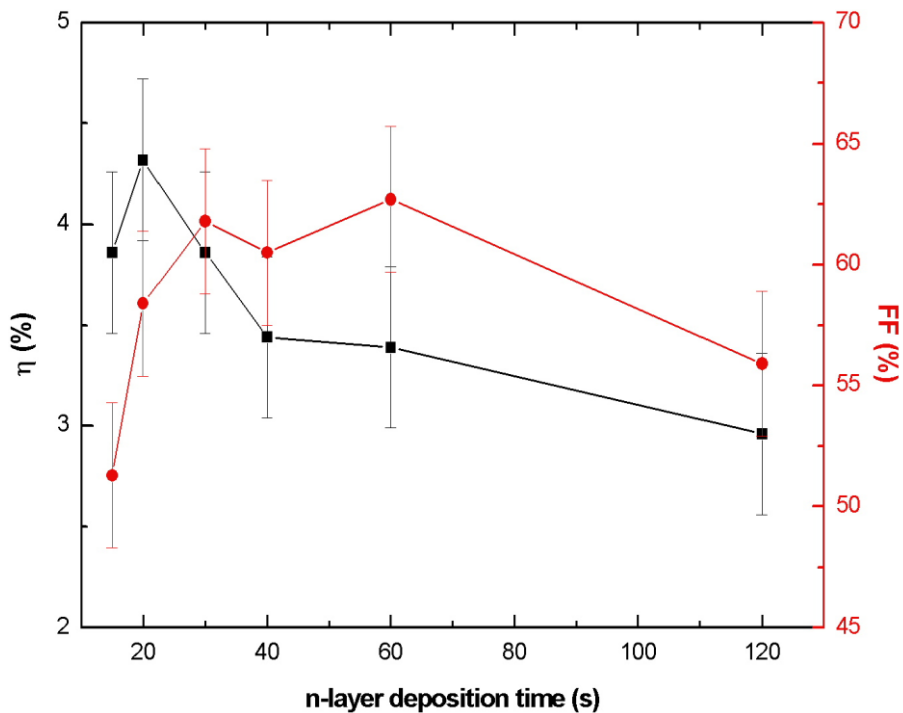
Figure 4.48 Efficiency and FF variation of the device, deposited at 225 °C, with respect to n layer deposition time.
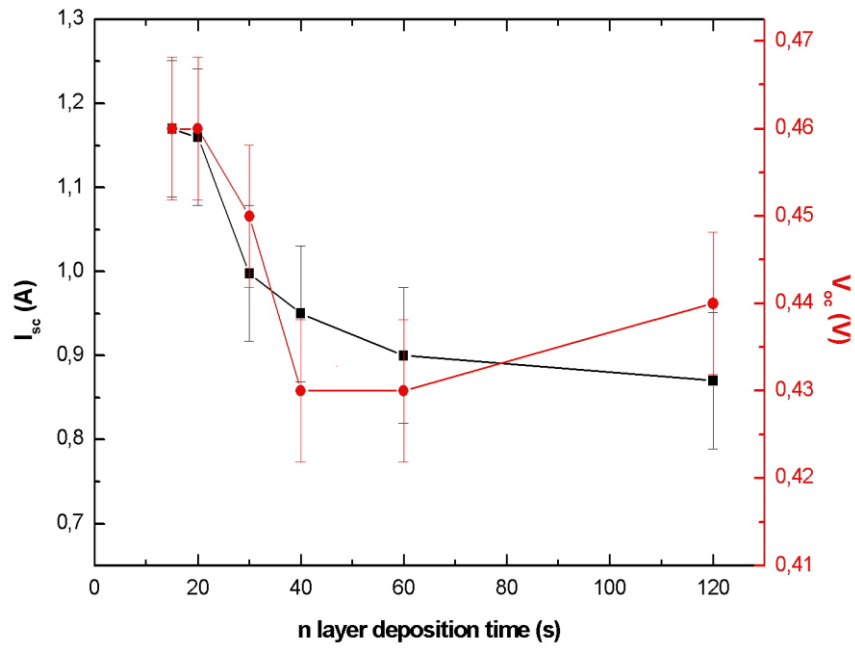
Figure 4.49 I_{sc} and V_{oc} variation of the device, deposited at 225 °C, with respect to n layer deposition time.

After determining the optimum thickness value for n-layer, we have started to intrinsic layer thickness optimization studies. For this purpose the i layer deposition times have been varied as 5s, 7s, 10s, 20s, 30s, 45s, 60s, 80s and 100s while keeping n-layer deposition time constant at 20s.

Obtained parameters with varing a-Si:H(i) layer thickness is given in Figures 4.50 and 4.51. At the end of i-layer deposition time studies, since it gives maximum efficiency and V_{oc} values, we have decided to work on 45s.
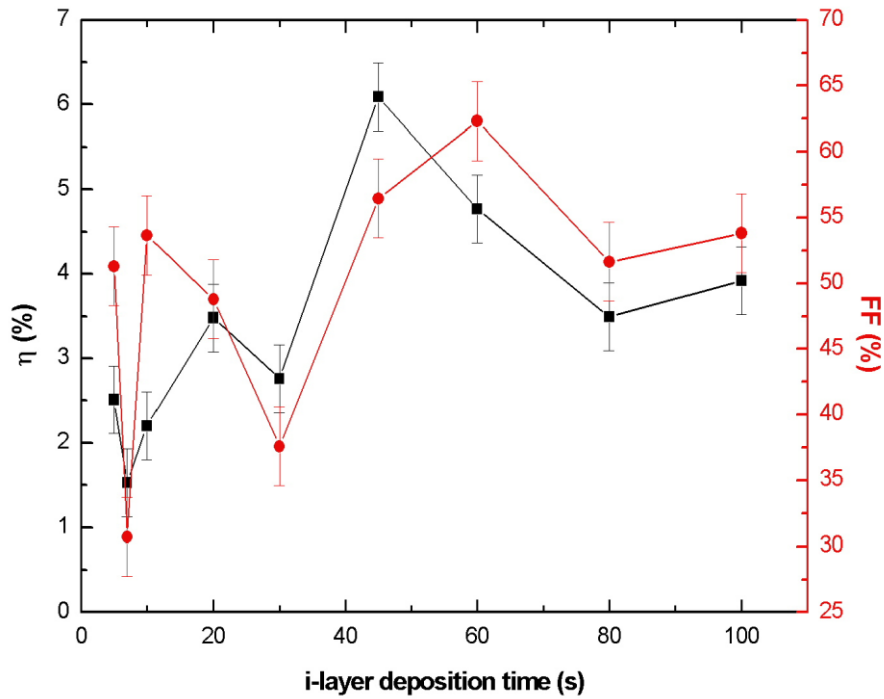
Figure 4.50 Efficieny and FF variation of the device, deposited at 225 °C, with respect to i layer deposition time.
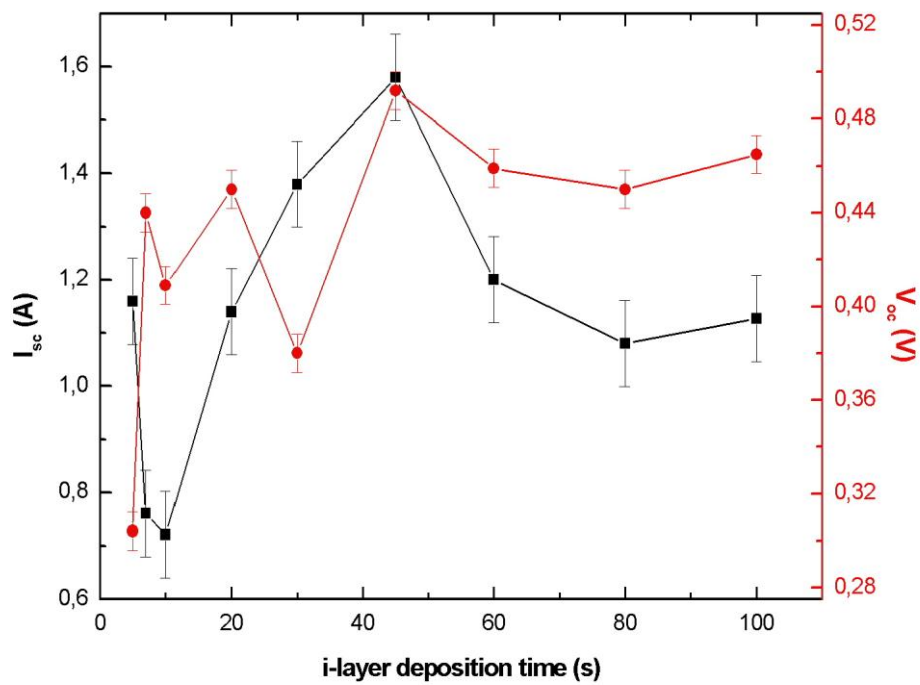
Figure 4.51 I_{sc} and V_{oc} variation of the device, deposited at 225 °C, with respect to i layer deposition time.

Since these sets of intrinsic layer samples were deposited in the PECVD chamber-II instead of chamber-I and since the electrode distances for two chambers are different, we cannot used the HRTEM result for the thickness calculation of 45 s deposited i-layer. Instead, we have used the SE model given in Figure 4.52.

Figure 4.52 SE model for 45s deposited intrinsic layer in Chamber-II

As a result, of this SE modelling we have obtained the following parameters given in Table 4.6 below. According to SE results, deposition rate for intrinsic layer in chamber II is calculated as 0.1A/sec which indicates that the optimum i-layer thickness is selected as 4.5 nm for our solar cell applications.

Table 4.5 Thin film parameters obtained from SE

L1 Thickness [nm]	1.978 ± 0.069
L2 Thickness [nm]	2.332 ± 0.216
L3 Thickness [nm]	0.059 ± 0.061
L4 Thickness [nm]	0.041 ± 0.016
a-Si-H_tl E_g [eV]	1.722 ± 0.000
a-Si-H_tl ε_∞	-1.243 ± 0.000
a-Si-H_tl A	230.812 ± 0.001
a-Si-H_tl E_o [eV]	3.831 ± 0.000
a-Si-H_tl C	1.763 ± 0.000
χ^2	0.117

CHAPTER 5

CONCLUSIONS and FUTURE STUDIES

This study has focused on the growth and composition of intrinsic hydrogenated amorphous silicon (a-Si:H) layer on the performance of a-Si:H/c-Si heterojunction solar cells on (100) oriented, one side polished, CZ, (p) c-Si wafers. All solar cells in this thesis were deposited on 100mm diameter wafers with 72 cm^2 total active area.

Cleaning c-Si wafers during the deposition of a-Si:H films in the PECVD system is a little bit tricky for this development. Both dry and wet chemical processes have been used for the cleaning of the wafer surface in order to decrease interface defect-state density, passivate and provide a smooth surface for a-Si:H deposition. A chemical cleaning procedure starting with RCA cleaning followed by oxide growth and removal is found to be most effective one.

For thin film a-Si:H based devices, it is well known that the PECVD conditions required to produce high quality a-Si:H are very close to the region where microcrystalline is deposited. However, for the growth of an intrinsic layer on c-Si wafers, especially on p-type, these deposition conditions often result in an epitaxial growth at the interface. This thin undoped epitaxial underlayer does not provide a good passivation of the wafer surface and reduce the V_{oc} of the device.

Imaginary part of the dielectric constant deduced from spectroscopic ellipsometry measurements were used for the structural variation analysis. For the samples with crystalline structure, imaginary part of the dielectric constant gives two sharp peaks at 3.5 eV and 4.2 eV. A broad peak around 3.6 eV indicates amorphous structure. Narrower peak with a shoulder at smaller photon energies indicates that the sample contains mixture of crystallinity and amorphous phase like nanocrystalline or microcrystalline structure.

For the case of the FTIR analyses, it is known that the wavenumber at 2000 cm^{-1} is due to the stretching mode of the Si-H bond and the wavenumber at 2090 cm^{-1} peak is the stretching mode of the Si-H$_2$ bond, respectively. The Si-H$_2$ stretching mode is the indication of defects in the film and appearance of it can be concluded as the increase of a dangling bond in the film due to the microcrystallization of the film. The intensity of the Si-H stretching mode on the other hand, indicates that good quality a-Si:H thin films.

From the HRTEM and SE results of intrinsic a-Si:H layers deposited at 225 °C, we have observed that there is a partial epitaxial growth at the beginning of the film deposition, which causes to decrease in the c-Si surface passivation.

Additionally, in order to study the growth mechanism of deposited intrinsic layer on the c-Si wafer we have deposited a series of films changing the deposition time from 15 seconds to 1800 seconds. From the SE and FTIR analyses, we have observed the microcryrstalline to amorphous phase transition during the film deposition like that: there is an epitaxial growth at the beginning of the deposition, followed by pyramidal shaped crystallines and then amorphous phase.

In order to overcome the epitaxial growth and to reach better surface passivation of c-Si wafers, such as a hydrogen rich and atomically abrupt a-Si:H/c-Si interface; it is suggested to deposit the a-Si layer at a temperature well below the optimum temperature and to recover the layer with an additional annealing step.

It is known that, in order to observe an improvement with an annealing process a minimum film thickness with a minimum amount of hydrogen is necessary in order to passivate the interface and prevent out diffusion of hydrogen from the film.

The diffusion of hydrogen from the a-Si:H layer to the c-Si surface is important for improving surface passivation and overall solar cell performance. In the early studies, as an explanation of the surface passivation it has been assumed that the hydrogen is diffused from the thin film bulk layer to the c-Si surface. Neverthless; since the minimum 2.49 eV energy is necessary to release the bonded hydrogen, it must either already be in a free or quasi-free state. Since density of dangling bonds is high, it is not possible to be free of hydrogen in the structure. Additionally low temperature thermal annealing and a relatively high defect density 10^{15}–10^{17} cm^{-3} would significantly inhibit a bulk diffusion of hydrogen toward the interface for surface passivation.

Number of different laboratories have calculated 0.7 ± 0.1 eV activation energy for the surface passivation, independent from the bulk layer thicknesses and they have concluded that lower activation energy values indicates that surface passivation is controlled by surfaces states, rather than bulk diffusion processes. Annealing process leads the rearrangement of hydrogen already present at the interface prior to deposition (HF-dip step) or else from hydrogen deposited during the initial stages of deposition.

From the barrier energy graph we have observed a small improvemet within the energy of 1.2-1.3 eV. In order to explain the mechanism behind this improvemet; we believe that on the cleaned wafer surface, after HF dipping c-si wafer surface is passivated by many H atoms. In the PECVD system, when the film grows, many of these H bonds replace with SiH_3 molecule leading to either epi- or a-Si:H growth. On the other hand, some of the Si-H bonds may preserve their original position or additional H would come from the plasma species. During annealing process, break of a weak Si-Si bond close to the surface and bond switching with the surface hydrogens would improve the surface passivation and improve the solar cell parameters.

Under these considerations we have deposited different sets of films at different substrate temperature values in between 100 to 225 ^{o}C, with an $[H_2]/[SiH_4]=10$. Then All the deposited samples were thermally annealed at 150°C and 250°C, varied annealing duration on a hot plate, in an air ambient.

Only a small improvement (30 mV) of V_{oc} has been observed within the cells after the annealing rather than expected, which indicates that there is still epi layer in heterostructure, and is also proved by the SE measurements.

Additionally, we have observed that V_{oc} value is limited to a range around 513 mV, which is due to the recombination at the local metal contacts at the backside and the microcrystalline behaviour of the intrinsic layer. Thin undoped epitaxial underlayer does not passivate the surface properly and no imrovement upon annealing was observed when the deposition was not purely amorphous.

From the device application studies, the highest efficiency of 9.2% has been obtained with Al/Ag front contact/a-Si:H(n)/a-Si:H(i)/c-Si(p)/Al back contact structure, measured under AM1.5G illumination for the films deposited at 225 ^{o}C substrate temperature, on 72 cm^2, 100 oriented, one side polished, CZ, (p) c-Si wafers.

It is believed that the back contact is still limiting the performance of our devices. Additionally optimization of front contact, especially TCO films deposited by RF sputtering at room temperature, is still a subject for further research. The resistance losses can be prevented by decreasing the series resistance of the device both with highly conductive TCO and good ohmic contacts.

In order to reduce the optical losses, one of the possible solution could be the texturizing the surface of the wafers to provide efficient light trapping.

Additionally, it has been observed that while there is an epitaxial growth on (100) substrate at around 200°C, on a (111) substrate at the same temperature, the film is essentially a-Si:H as soon as the deposition starts. During studies we have used one side polished (100) oriented p-type wafer and it is known that it is better to use (111) oriented n type, double side polished wafer for the better surface passivation.

REFERENCES

[1] Goatzberger A., Hoffmann V.U., 2005, Photovoltaic Solar Energy Generation (Springer)

[2] Rostan P. J., 2010, a-Si:H/c-Si Heterojunction Front- and Back Contacts for Silicon Solar Cells With p-type Base, PhD Thesis, Institut für Physikalische Elektronik der Universiẗat Stuttgart

[3] Mishima T., Taguchi M., Sakata H., Maruyama E., 2011, Development Status of High-Efficiency HIT Solar Cells, Solar Energy Materials & Solar Cells, 95, 18-21

[4] Flamn D. L., 1990, Mechanisms of Silicon Etching in Fluorine- and Chlorine-Containing Plasmas, Pure &Applied Chem., 62, 9, 1709-1720

[5] Poortmans J., Arkhipov V., 2005, Thin Film Solar Cells Fabrication Characterisation And Applications (John Wiley & Sons)

[6] Street, R. A., 2005, Hydrogenated amorphous Silicon (Cambridge University Press)

[7] Schulze, T. F., 2011, Structural, Electronic and Transport Properties of Amorphous/Crystalline Silicon Heterojunctions, PhD Thesis, Institut für Silizium-Photovoltaik E-I1, Helmholtz Centre Berlin

[8] Zeman M., Thin Film Silicon Solar Cells, Report

[9] Chai L., 1997, Improved Understanding and Control of the Properties of PECVD Silicon Nitride and its Applications in Multicrystalline Silicon Solar Cells, PhD Thesis, Georgia Institute of Thecnology

[10] Tucci, M.; Noce, M.d.; Bobeico, E.; Roca, F.; Cesare, G.d.; Palma, F., 2004, Comparison of Amorphous/Crystalline Heterojunction Solar Cells Based on n- and p-type Crystalline Silicon , Thin Solid Films, 451-452, 355-360

[11] Shen, J. M., 1995, Characterization Of Fluorinated Hydrogenated Amorphous Silicon Nitride Alloys, PhD Thesis, Texas Tech University

[12] Anderson P. W., 1975, Model for the Electronic Structure of Amorphous Semiconductors, Physc. Rev. Lett., 34, 953-955

[13] Liu S., 1997, Deposition, Characterization, And Device Application of Amorphous Carbon and Amorphous Silicon Films, PhD Thesis, Texas Tech University

[14] Kasap S., Capper P., 2006, Springer Handbook of Electronic and Photonic Materials (Springer)

[15] Gaspari F., 2011, Optoelectronic Properties of Amorphous Silicon the Role of Hydrogen: from Experiment to Modelling, Optoelectronics-Materials and Techniques (Padmanabhan Predeep)

[16] Grundmann M., 2010, The Physics of Semiconductors (Springer)

[17] Hassan El Gohary, 2010, Development of Low-Temperature Epitaxial Silicon Films and Application to Solar Cells, PhD Thesis, University of Waterloo, Ontarino, Canada

[18] Leu G. F., Grünenfelder P., Modrzynski P., 2011, Dissociation Efficiency of NF_3 in a Capacitively Coupled Plasma: a Phenomenological Parameterization, 30th ICPIG, Belfast, Northern Ireland, UK

[19] Smith B. C., Young A., 2001, Optimazing Chamber Cleans for Better Film Deposition Performance, Journal of the Electrochemical Society, 148 (11), C721-C725

[20] Hrunski D., Rech B., Schmitz R., Mück A., Pinçon O., Breuer U., Beyer W., 2008, Influence of Contaminations on the Performance of Thin-Film Silicon Solar Cells Prepared After in situ Reactor Plasma Cleaning, Thin Solid Films, 516, 4639-4644

[21] Abelson J. R., 1993, Plasma Deposition of Hydrogenated Amorphous Silicon: Studies of the Growth Surface, Appl. Phys., A56, 493-512

[22] Tanaka, K., 1989, Hydrogenated Amorphous Si and Its Alloy Materials: New Approach to Structural Control, Optoelect. Dev and Tech., 4:2, 143-153.

[23] Bruno, G., Capezzuto P., Madan A., 1995, Plasma Deposition of Amorphous Silicon- Based Materials. Academic Press, ISBN: 9780121379407, Burlington, MA.

[24] Ferlauto, A. S., Koval, R. J., Wronski, C. R., Collins, R. W ., 2001, Phase Diagrams for the Optimization of rf Plasma Enhanced Deposition of a-Si:H: Variations in Plasma Power and Substrate Temperature, Materials Research Society Symposium Proceedings, 664, A5.4

[25] van Sark W. G. J. H. M., 2002, Methods of Deposition of Hydrogenated Amorphous Silicon for Device Applications, PhD Thesis, Utrecht University

[26] Takai, M., Nishimoto, T., Takagi, T., Kondo, M. and Matsuda, A., 2000, Guiding principles for obtaining stabilized amorphous silicon at larger growth rates, J. Non-Cryst. Solids., 266-269, 90-94

[27] Bruno G., Capezzuto P., Madan A., 1995, Plasma Deposition of Amorphous Silicon-Based Materials, (Academic Press, Boston, MA, U.S.A.)

[28] Rahman K. M. A., 2010, Nanocrystalline Silicon Solar Cells Deposited via Pulsed PECVD at 150°C Substrate Temperature, MS Thesis, University of Waterloo

[29] Guha S., Multijunction Solar Cells and Modules, in Technology and Applications Amorphous Silicon, Street R. A., 2000, 252 – 305, (Springer)

[30] Donker M. N. van den, Rech B., Schmitz R., Klomfass J., Dingemans G., Finger F., Houben L., Kessels W. M. M., and Sanden M. C. M. V.,2007, Hidden parameters in the plasma deposition of microcrystalline silicon solar cells, Journal of Materials Research, 22, 7, 1767 – 1774

[31] Estrada M., Cerdeira A., Soto S., 1999, High Deposition Rate a-Si:H Layers from Pure SiH_4 and from a 10% Dilution of SiH_4 in H_2, Superficies y Vacio, 9, 306-309

[32] Halindintwali S., 2005, A Study of Hydrogenated Nanocrystalline Silicon Thin Films Deposited by Hot-Wire Chemical Vapour Deposition, PhD Thesis, University of the Western Cape

[33] van Sark W.G.J.H.M., Korte L., Roca F., 2012, Physics and Technology of Amorphous-Crystalline Heterostructure Silicon Solar Cells, (Springer)

[34] Labrune M., 2011, Silicon Surface Passivation and Epitaxial Growth on c-Si by Low Temperature Plasma Processes for High Efficiency Solar Cells, PhD Thesis, Docteur de Ecole Polytechnique

[35] Matsuda A., 2004, Microcrystalline Silicon. Growth and Device Application, Journal of Non-Crystalline Solids, 338-340, 1-12

[36] Cervantes, D. M., 2008, Silicon Heterojunction Solar Cells Obtained by Hot Wire CVD, PhD Thesis, Universitat Politecnika de Catalunya

[37] Lacoste, J. D.; Cabarrocas, P. R., 2009, Toward a Better Physical Understanding of a-Si:H/c-Si Heterojunction Solar Cells, Journal of Applied Physics, 105, 063712

[38] De Wolf, S.; Ballif, C.; Kondo, M., 2012, Kinetics of a-Si:H Bulk Defect and a-Si:H/c-Si Interface-State Reduction, Physical Review B, 85, 113302

[39] Wang, T.H.; Iwaniczko, E.; Page, M.R.; Levi, D.H.; Yan, Y.; Branz, H.M.; Wang Q., 2005, Effective Interfaces in Silicon Heterojunction Solar Cells, 31st IEEE Photovoltaics Specialists Conference and Exhibition, NREL/CP-520-37457

[40] Wang, T.H.; Iwaniczko, E.; Page, M.R.; Wang Q.; Xu, Y.; Yan, Y.; Levi, D.; Roybal, L.; Bauer, R.; Branz, H.M., 2006, High Efficiency Silicon Heterojunction Solar Cells by HWCVD, 4th IEEE World Conference, 1439-1442

[41] I Cabarrocas, P. R.; Cariou, R.; Labrune, M., 2012, Low Temperature Plasma Deposition of Silicon Thin Films: From Amorphous to Crystalline, Journal of Non-Crystalline Solids, 358, 2000-2003

[42] Fujiwara H., Kaneko t., Kondo M., 2007, Application of Hydrogenated Amorphous Silicon Oxide Layers to c-Si Heterojunction Solar Cells, Applied Physics Letters, 91, 133508

[43] De Wolf, S.; Kondo, M., 2007, Abruptness of a-Si:H/c-Si Interface Revealed by Carrier Lifetime Measurements, Applied Physics Letters, 90, 042111

[44] Fujiwara, H.; Kondo, M., 2007, Impact of Epitaxial Growth at the Heterointerface of a-Si:H/c-Si Solar Cells, Applied Physics Letters, 90, 013503

[45] Pysch D., Ziegler J., Becker P., Suwito D., Janz S., Glunz S. W., Hermle M., 2009, Potentials and Development of Amorphous Silicon Carbide Heterojunction Solar Cells, IEEE, 34th IEEE Photovoltaic Specialists Conference, Vol.1, 000794

[46] Schulze, T.F.; Beushaesen, H.N.; Hansmann, T.; Korte, L.; Rech, B., 2009, Accelerated Interface Defect Removal in Amorphous/Crystalline Silicon Heterostructures using Pulsed Annealing and Microwave Heating, Applied Physics Letters, 95, 182108

[47] De Wolf S., Andrault Y., Barraud L., Bartlome R., Batzner D., Bole P., Choong G., Demaurex B., Descoeudres A., Guerin C., Holm N., Kobas M., Lachenal D., Mendes B., Strahm B., Tesfai M., Wahli G., Wuensch F., Zicarelli F., Buechel A., Ballif C., 2010, High Efficiency Silicon Heterojunction Solar Cells: from Physics to Production Lines, 10th IEEE International Conference, 1986-1989

[48] Illiberi A., Creatore M., Kessels W.M.M., van de Sanden M.C.M, 2010, Hydrogenated Amorphous Silicon Based Surface Passivation of c-Si at High Deposition Temperature and Rate, Phys. Status solidi RRL 4, 8-9, 206-208

[49] Jeon M., Kamisako K., 2009, Hydrogenated Amorphous Silicon Thin Films as Passivation Layers Deposited by Microwave Remote-PECVD for Heterojunction Solar Cells, Transactions on Electrical and Electronic Materials, 10(3), 75

[50] Zhang X., Fronheiser J.A., Korevaar B.A., Tolliver T.R., 2008, a-Si/c-Si Interfaces: the Effect of Annealing and Film Thickness, 33rd IEEE Photovoltaic Specialists Conference, 1-5

[51] Burrows M. Z., Das U. K., Opila R.L., De Wolf S., Birkmire R.W., 2008, Role of Hydrogen Bonding Environment in a-Si:H Films for c-Si Surface Passivation, Journal of Vacuum Science and Technology A, 26, 683

[52] Mitchell J., Macdonald D., Cuevas A., 2009, Thermal Activation Energy for the Passivation of the n-type Crystalline Silicon Surface by Hydrogenated Amorphous Silicon, Applied Physics Letters, 94, 162102

[53] De Wolf S., Kondo M., 2009, Nature of Doped a-Si:H/c-Si Interface Recombination, Journal of Applied Physics, 105, 103707

[54] Jeon M., Yoshiba S., Kamisako K., 2010, Hydrogenated Amorphous Silicon Film as Intrinsic Passivation Layer Deposited at Various Temperatures using RF Remote-PECVD Technique, Current Applied Physics, 10, 237-240

[55] Taguchi M., Terakawa A., Maruyama E., Tanaka M., 2005, Obtaining a Higher V_{oc} in HIT Cells, Progress in Photovoltaics: Research and Applications, 13, 481-488

[56] Wang Q., Page M.R., Iwaniczko E., Xu Y., Roybal L., Bauzer R., To B., Yuan H.C., Duda A., Hasoon F., Yan F.Y., Levi D., Meier D., Branz H.M., Wang T.H., 2010, Efficient Heterojunction Solar Cells on p-type Crystal Silicon Wafers, Applied Physics Letters, 96, 013507

[57] Meijun Lu, 2008, Silicon Heterojunction Solar Cell and Crystallization of Amorphous Silicon, PhD Thesis, University of Delaware

[58] van Cleef M.W.M., Rubinelli F.A., Rath J.K., Schropp R.E.I., van der Weg W.F., Rizzoli R., Summonte C., Pinghini R., Centurioni E., Galloni R., 1998, Photocarrier Collection in a-SiC:H/c-Si Heterojunction Solar Cells, Journal of Non-Crystalline Solids, 227-230, 1291-1294

[59] Centurioni E., Iencinella d., Rizzoli R., Zignani F., 2004, Silicon Heterojunction Solar Cell: A New Buffer Layer Concept With Low-Temperature Epitaxial Silicon, IEEE Transantions on Electron Devices, 51(11), 1818

[60] Centurioni E., Iencinella d., Rizzoli R., Zignani F., 2004, Silicon Heterojunction Solar Cell: A New Buffer Layer Concept With Low-Temperature Epitaxial Silicon, IEEE Transantions on Electron Devices, 51(11), 1818

[61] Angermann H., 2008, Passivation of Structured p-type Silicon Interfaces: Effect of Morphology and Wet-Chemical Pre-Treatment , Applied Surface Science, 254, 8067-8074

[62] Munoz D., Carreras P., Escarre J., Ibarz D., Martin de Nicola S., Voz C., Asensi J.M., Bertomeu J., 2009, Optimization of KOH Etching Process to Obtain Textured Substrates Suitable for Heterojunction Solar Cells Fabricated by HWCVD , Thin Solid Films, 517, 3578-3580

[63] Taguchi M., Sakata H., Yoshimine Y., Maruyama E., Terakawa A., Tanaka M., An Approach for the Higher Efficiency in the HIT Cells , web.mit.edu

[64] Park J.B., Oh J.S., Gil E., Kyoung S.J., Kim J.S., Yeom G.Y., 2009, Plasma Texturing of Multicrystalline Silicon for Solar Cell using Remote-Type Pin-to-Plate Dielectric Barrier Discharge , Journal of Physics D: Applied Physics, 42, 215201

[65] Henrion W., Rebien M., Angermann H., Röseler A., 2002, Spectroscopic Investigations of Hydrogen Termination, Oxide Coverage, Roughness and Surface State Density of Silicon During Native Oxidation in Air , Applied Surface Science, 202, 199-205

[66] Tucci M., De Rosa R., Roca F., 2001, CF_4/O_2 Dry Etching of Textured Crystalline Silicon Surface in a-Si:H/c-Si Heterojunction for Photovoltaic Applications , Solar Energy Materials&Solar Cells, 69, 175-185

[67] Tucci M., Salurso E., Roca F., Palma F., 2002, Dry Cleaning Process of Crystalline Silicon Surface in a-Si:H/c-Si Heterojunction for Photovoltaic Applications , Thin Solid Films, 403-404, 307-311

[68] Anandan C., Mukherjee C., Seth T., Dixit P.N., Bhattacharyya R., 1995, Effect of Pulse Parameters on the Deposition Rate of Hydrogenated Amorphous Silicon in a Modified Pulsed Plasma Discharge, Applied Physics Letters, 66, 85

[69] Spectroscopic Ellipsometry User Guide, Horiba, Jobin Yvon.

[70] Petrus Jacobus van den Oever, 2007, In Situ Studies of Silicon-Based Thin Film Growth for Crystalline Silicon Solar Cells, Eindhoven: Technische Universiteit

[71] Kageyama S., Akagawa M., Fujiwara H., 2011, Dielectric Function of a-Si:H based on Local Network Structures, Physical Review B, 83, 195205

[72] Yuguchi T., Kanie Y., Matsuki N., Fujiwara H., 2012, Complete Parametrization of the Dielectric Function of Microcrystalline Silicon Fabricated by Plasma-Enhanced Chemical Vapor Deposition, Journal of Applied Physics, 111, 083509

[73] Jason A. Stoke, 2008, Spectroscopic Ellipsometry Analysis of the Component Layers of Hydrogenated Amorphous Silicon Triple Junction Solar Cells, Master of Science, University of Toledo

[74] Aspnes D.E., 1982, Optical Properties of Thin Films, Thin Solid Films, 89, 249-262

[75] Fujiwara, H.; Koh, J.; Rovira, P.I.; Collins, R.W., 2000, Assesment of Effective-Medium Theories in the Aanalysis of Nucleation and Microscopic Surface Roughness Evolution for Semiconductor Thin Films, Physical Review B, 61(16), 10832(13)

[76] Ferlauto, A. S. ; Ferreira, G.M.; Pearce, J.M. ; Wronski, C.R.; Collins, R. W ., 2002, Analytical Model for the Optical Functions of Amorphous Semiconductors from the Near-Infrared to Ultraviolet: Applications in Thin Film Photovoltaics, Journal of Applied Physics, 92(5), 2424

[77] Teplin, C.W. ; Levi, D.H.; Iwaniczko, E. ; Jones, K.M.; Perkins, J. D ., 2005, Monitoring and Modeling Silicon Homoepitaxy Breakdown with Real-Time Spectroscopic Ellipsometry, Journal of Applied Physics, 97, 103536

[78] Morral, A.F. ; Cabarrocas, P.R.; 2004, Structure and Hydrogen Content of Polymorphous Silicon Thin Films Studied by Spectroscopic Ellipsometry and Nuclear Measurements, Physical Review B, 69, 125307

[79] Pereira, L.; Aguas, H.; Fortunato, E.; Martins, R., 2006, Nanostructure Characterization of High k Materials by Spectroscopic Ellipsometry, Applied Surface Science, 253, 339-343

[80] Feng, G.F.; Zallen, R., 1989, Optical Properties of Ion-Implanted GaAs: The Observation of Finite-Size Effects in GaAs Microcrystals, Physical Review B, 40, 1064

[81] Hasbullah Bin Anthony Hasbi, 2005, Structural Properties of Hydrogenated Amorphous Silicon (a-Si:H) Thin Film Grown via Radio Frequency Plasma Enhanced Chemical Vapor Deposition (RP PECVD), Master of Science, Universiti Teknologi Malaysia

[82] Arno Hendrikus Marie Smets, 2002, Growth Related Material Properties of Hydrogenated Amorphous silicon, Eindhoven: Eindhoven University of Technology

[83] Peng, W.; Zeng, X.; Liu, S.; Xiao, H.; Kong, G.; Yu, Y.; Liao, X., 2009, Study of Microstructure and Defects in Hydrogenated Microcrystalline Silicon Films, Photovoltaic Specialists Conference, 34th IEEE, 001029-001033

[84] Laurent Kroely, 2010, Process and Material Challenges in the High Rate Deposition of Microcrystalline Silicon Thin Films and Solar Cells by Matrix Distributed Electron Cyclotron Resonance Plasma, PhD Thesis, Ecole Polytechnique, Paris

[85] Vavrunkova V.; Mullerova, J.; Sutta, P., 2007, Microstructure Related Characterization of a-Si:H Thin Films PECVD Deposited Under Varied Hydrogen Dilution, Advances in Electrical and Electronic Engineering

[86] Wang Y.H. , Lina J., Huana C.H.A., 2003, Structural and Optical Properties of a-Si:H/nc-Si:H Thin Films Grown from Ar–H$_2$–SiH$_4$ Mixture by Plasma-Enhanced Chemical Vapor Deposition, Materials Science and Engineering, B104, 80–87

[87] Smets, A.H. ; Matsui, T.; Kondo, M., 2008, Infrared Analysis of the Bulk Silicon-Hydrogen Bonds as an Optimization Tool for High-Rate Deposition of Microcrystalline Silicon Solar Cells, Applied Physics Letters, 92, 033506

[88] Aad Gordijin, 2005, Microcrystalline Silicon for Thin-Film Solar Cells, PhD Thesis, Universiteit Utrecht

[89] Agnes Marie Henriette Petit, 2006, Expanding Thermal Plasma Deposition of Hydrogenated Amorphous Silicon for Solar Cells, PhD Thesis, Delft University of Technology

[90] Ovain D. Clark, 2009, Thin Film Amorphous silicon Cells by Inductive PECVD, with a View Towards Flexible Substrates, PhD Thesis, University of Southampton

[91] Lu M., 2008, Silicon Heterojunction Solar Cell and Crystallization of Amorphous Silicon, PhD Thesis, University of Delaware

[92] Fuyuki, T. ; Kondo, H.; Kaji, Y.; Ogane A.; Takahashi Y., 2007, Analytic Findings in the Electroluminescence Characterization of Crystalline Silicon Solar Cells, Journal of Applied Physics, 101, 023711

[93] Köntges, M. ; Siebert, M.; Hinken, D.; Eitner U.; Bothe, K.; Potthof, T., 2009, Quantitative Analysis of PV-Modules by Electroluminescence Images for Quality Control, 24th European Photovoltaic Solar Energy Conference, Hamburg, Germany, 4CO.2.3

[94] Croizer, J.L.; Vorster, F.J.; van Dyk, E.E., 2011, Centre for Renewable and Sustainable Energy Studies

[95] Jacqueline Louise Crozier, 2012, Characterization of Cell Mismatch in Photovoltaic Modules using Electroluminescence and Associated Electro-Optic Techniques, Master of Science, Nelson Mandela Metropolitan University

[96] Köntges M., Siebert M., Hinken D., Eitner U., Bothe K., Potthof T., 2009, Quantitative Analysis of PV-modules by Electroluminescence Images for Quality Control, 24st European Photovoltaic Solar Energy Conference, Hamburg, Germany

[97] Kilani D., 2008, Electroluminescence for Characterisation of Solar Cells, Lot Oriel, Application note

[98] Lee S. Y., Shim J. H., You D. J., Ahn S., MinLee H., 2011, The Novel Usage of Spectroscopic Ellipsometry for the Development of Amorphous Si Solar Cells, Solar Energy Materials & Solar Cells, 95, 142–145

[99] Maydell, K.v.; Conrad, E.; Schmid, M., 2006, Efficient Silicon Heterojunction Solar Cells Based on p- and n-type Substrates Processed at Temperatures < 220 °C, Progress in Photovoltaics: Research and Applications, 14, 289-295

[100] Soppe, W.J.; Devilee, C.; Biebericher, A.C.W.; Simit, C.; et al., 2004, Micro Crystalline Silicon in the Netherlands, ECN publications

[101] Levi, D. H.; Nelson, B. P.; Perkins, J. D.; Moutinho, H. R., 2003, In situ Studies of the Amorphous to Microcrystalline Transition of Hot-wire Chemical Vapor Deposition Si:H Films Using Real-Time Spectroscopic Ellipsometry, Journal of Vacuum Science & Technology, A 21 (4), 1545

[102] Burrows, V. A.; Chabal, Y. J.; Higashi, G. S.; et al., 1988, Infrared Spectroscopy of Si (111) Surfaces After HF Treatment: Hydrogen Termination and Surface Morphology, Applied Physics Letters, 53, 998-1000

[103] Schmidt, M.; Angermann, H.; Conrad, E.; et al., 2006, Physical and Technological Aspects of a-Si:H/c-Si Heterojunction Solar Cells, IEEE 4th World Conference, 1433-1438

[104] Morral, A.F. ; Cabarrocas, P.R.; 2002, Etching and Hydrohen Diffusion Mechanisms During a Hydrogen Plasma Treatment of Silicon Thin Films, Journal of Non-Crystalline Solids, 299-302, 196-200

[105] Hekmatshoar, B.; Shahrjerdi, D.; Hopstaken, M.; Sadana, D., 2011, Metastability of Hydrogenated Amorphous Silicon Passivation on Crystalline Silicon and Implication to Photovoltaic Devices, Reliability Physics Symposium, IEEE International, 5E.5.1-5E.5.4

CURRICULUM VITAE

PERSONAL INFORMATION

Surname, Name: Pehlivan, Özlem
Nationality: Turkish (TC)
Date and Place of Birth: 16 Nowember 1976, Eskişehir
Marital Status: Single
Phone: +90 262 679 50 00
Fax: +90 262 679 50 01
email: ozlem.guven@tubitak.gov.tr

EDUCATION

Degree	Institution	Year of Graduation
MS	METU Physics, Ankara	2001
BS	METU Physics, Ankara	1998

WORK EXPERIENCE

Year	Place	Enrollment
2002- Present	Tubitak UME, KOCAELI	Researcher
1998-2002	Atılım University, ANKARA	Research Assistant

PUBLICATIONS & PRESENTATIONS

1. ***Ö.Pehlivan***, O.Yılmaz, A.O.Kodolbaş, Ö. Duygulu, M. Tomak, "Structural Characterization of Intrinsic a-Si:H Thin Films for Silicon Heterojunction Solar Cells, accepted for publication in Journal of Optoelectronics and Advanced Materials, 2013.

2. ***Ö.Pehlivan***, O.Yılmaz, A.O.Kodolbaş, Ö. Duygulu, M. Tomak, "Structural Characterization of Intrinsic a-Si:H Thin Films for Silicon Heterojunction Solar Cells, Solar TR-2, Solar Electricity Conference and Exhibition, 7-9 November 2012, Antalya, Turkey.

3. D. Menda, O. Özdemir, A.O. Kodolbaş, O. Yılmaz, ***Ö. Pehlivan***, K. Kutlu, "Effects of Substrate Temperature and Annealing on PECVD Grown HIT Solar Cells", Solar TR-2, Solar Electricity Conference and Exhibition, 7-9 November 2012, Antalya, Turkey.

4. D. Menda, ***Ö. Pehlivan Güven***, O. Yılmaz, A. O. Kodolbaş, O. Özdemir, K. Kutlu "Structural and Interface Properties of Doping Inversed HIT Solar Cells through TEM Analysis", "SuNEC 2012 (Sun New Energy Conference)", Palermo- İtalya, 4-6 Eylül 2012.

5. A Diril and ***O P Guven***, "Characterization of UME-made Co-C eutectic fixed-point blackbody cells", International Journal of Thermophysics, Volume 32, Issue 11-12, Pages 2671-2679, 2011.

6. I Pusnik, S Clausen, J O Favreau, B Gutschwager, A K Dogan, A Diril, ***O P Guven***, H McEvoy, SS Hoem, A Steiner, E van der Ham, "Comparison of Blackbodies for Calibration of Infrared Ear Thermometers", International Journal of Thermophysics, Volume 32, Issue 1-2, Pages 127-138, 2011.

7. A Diril and ***O P Güven***, "Characterization of UME-made Co-C eutectic fixed-point blackbody cells and thermodynamic temperature measurements", Proceedings of Tempmeko 2010, Slovenia.

8. M Sadli, *O Pehlivan*, F Bourson, A Diril, K Ozcan, "Collaboration Between UME and LNE-INM on Co–C Eutectic Fixed-Point Construction and Characterization" International Journal of Thermophysics, Volume 30, Issue1, Pages 36-46, 2009.

9. H. Nasibov, A. Diril, *O.Pehlivan*, "Calibration and characterization of the infrared pyrometer for the float glass temperature measurements" The African Committee of Metrology, 2008, Tunisia.

10. H.Nasibov, S.O.Aytekin, *O.Pehlivan*, A.Diril, "Automation of experimental data handling in calibration procedures using VBA." The African Committee of Metrology, 2008, Tunisia.

11. M Sadli, *O Pehlivan*, F Bourson, A Diril, K Ozcan, "Collaboration on Co-C Eutectic Fixed-Point Construction and Characterization Between UME and LNE INM/CNAM." Tempmeko 2007 Proceedings.

12. S.Uğur, *O.Pehlivan*, "UME Radiation Temperature Laboratory" VI.National Metrology Conference , 2005.

13. S. Uğur, A. Diril, *O.Pehlivan*, "Referans Radyasyon Thermometre ile EUROMET-Temel Parametreler Ölçüm Sonuçları", Electro-Optic Meeting, 2004, Istanbul.

14. H. Nasibov, *O.Pehlivan*, S. Uğur, "Interpolation Equation for the Optical Radiation Thermometer". 2003 Electro-Optic Meeting, Ankara.